

Spatio-temporal Correlations in the Manna Model in one, three and five dimensions

Gary Willis and Gunnar Pruessner*

*Department of Mathematics, Imperial College London,
180 Queen's Gate, London SW7 2AZ, United Kingdom*

Although the paradigm of criticality is centred around spatial correlations and their anomalous scaling, not many studies of Self-Organised Criticality (SOC) focus on spatial correlations. Often, integrated observables, such as avalanche size and duration, are used, not least as to avoid complications due to the unavoidable lack of translational invariance. The present work is a survey of spatio-temporal correlation functions in the Manna Model of SOC, measured numerically in detail in $d = 1, 3$ and 5 dimensions and compared to theoretical results, in particular relating them to “integrated” observables such as avalanche size and duration scaling, that measure them indirectly. Contrary to the notion held by some of SOC models organising into a critical state by re-arranging their spatial structure avalanche by avalanche, which may be expected to result in large, non-trivial, system-spanning spatial correlations in the quiescent state (between avalanches), correlations of inactive particles in the quiescent state have a small amplitude that does not increase with the system size, although they display (noisy) power law scaling over a range linear in the system size. Self-organisation, however, does take place as the (one-point) density of inactive particles organises into a particular profile that is asymptotically independent of the driving location, also demonstrated analytically in one dimension. Activity and its correlations, on the other hand, display non-trivial long-ranged spatio-temporal scaling with exponents that can be related to established results, in particular avalanche size and duration exponents. The correlation length and amplitude are set by the system size (confirmed analytically for some observables), as expected in systems displaying finite size scaling. In one dimension, we find some surprising inconsistencies of the dynamical exponent. A (spatially extended) mean field theory is recovered, with some corrections, in five dimensions.

PACS numbers: 05.65.+b, 05.70.Jk

I. INTRODUCTION

Correlations functions are at the heart of critical phenomena [1]. They capture spatio-temporal scaling in microscopic variables (position and time) and, via integrals, also on the large scale (system size and duration). In the form of propagators or response functions, they govern most of our theoretical understanding of critical phenomena, certainly all of field theory [2]. In fact, originally, temporal correlation functions were the key-motivation of Self-Organised Criticality (SOC) [3, 4], namely to develop a theory of $1/f$ noise [5]. However, for a range of reasons interest in correlation functions in SOC systems ceased very quickly [6]: Firstly, $1/f$ noise in the Bak-Tang-Wiesenfeld Model was quickly repudiated [7], secondly spatial analogues were difficult to come by numerically (because necessary boundary and initial conditions spoil translational invariance thereby making it impossible to improve estimates by taking spatial averages) and thirdly, spatio-temporal integrals were very easily determined and linked very nicely with established theories and systems, in particular via correlation functions [1, 8, 9]. Given modern computing resources, most of the technical difficulties are fairly easily overcome, except maybe for the effort needed to carefully implement the observables, so that they can be measured efficiently.

To make further theoretical progress, indeed a more complete understanding of correlations in SOC systems is needed. Does the “substrate”, *i.e.* the lattice occupied by immobile particles these models “live on”, self-organise in any form? Does it develop (long-ranged, clearly visible) correlations? Those questions are part of the narrative of an SOC model developing into its critical state [10, 11]. In the active state, what does the response function look like, *i.e.* where, when and how much activity is seen in a system after it is being perturbed (activated) somewhere? What is left of the old claim of $1/f$ noise? Which correlations display non-trivial scaling and how is that related to the known scaling of avalanches [4], or, in fact, to growth models [12, 13]? How does the behaviour above the upper critical dimension relate to mean field theory?

The scaling that we are primarily concerned with is finite size scaling, and more specifically scaling of amplitudes and characteristic (correlation) lengths with the system size. This has two key reasons: Firstly, in SOC systems the finite extent should be the only finite (large length) scale. Secondly, we expect that it is difficult to identify the scaling of an observable (in particular in natural systems), if its amplitude is fixed and cannot be increased by studying bigger systems. If the (effective) lattice spacing is very small compared to the range of observations, such a feature might be indiscernible in measurements. Conversely, it is easier to measure scaling of an observable, when its amplitude scales with the system size.

The aim of this work is twofold: On the one hand, we

*Electronic address: g.pruessner@imperial.ac.uk; URL: <http://www.ma.ic.ac.uk/~pruess>

want to confirm that many of the features to be expected in a self-organised critical system are actually present, *i.e.* correlation functions really display what is expected according to the paradigm [3, 4, 6, 14–17], such as the spatial correlation length scaling linearly in the system size and the self-organisation being independent of details such as the driving. A key-objective is to provide an overview of correlation functions that is broad in scope as far as different correlations are concerned. To keep the size of this work within reason we therefore focus on a single model, namely on the Abelian Manna Model which to us seems particularly well behaved [18, 19]. To our knowledge, the present work is nevertheless one of the most comprehensive surveys of correlation functions in an SOC model to date. However, we are by far not the first to study correlation functions in SOC, which have received prominent attention in the past [20], most notably in the form of important exact results [21–32] for the Abelian Sandpile Model [3, 20] and its directed variant [33], but also as a key-feature in SOC models generally [17, 34–36]. Moreover, correlation functions have recently been studied at the interface between absorbing state phase transitions and SOC [37–40].

On the other hand, we want to make contact with theoretical and in particular field-theoretical work, where response and correlation functions play a central rôle. Some theories have been or still are being developed, which we can compare our numerical findings to [41, 42]. We can also verify standard scaling forms [2] and relate the scaling of correlation functions to those of observables normally investigated in SOC, such as avalanche sizes and duration [4, 9]. Many of our findings can also be compared to mean-field theories, which serve as a first reference point and which (normally) become exact above the upper critical dimension $d_c = 4$ [9, 43, 44]. Mean-field theories are unable to capture non-trivial scaling and (most of) the non-trivial physics and in the past they have often been equated with a lack of spatial structure [10, 45–54]. However, there is no need for a mean field theory to do away with dissipation at boundaries, which has been suggested to be so crucial to SOC [55, 56] and implement their average effect by way of a global dissipation rate [52, 57–59]. Although we will briefly introduce the relevant features of the mean-field theory in Sec. II B, we will not dwell on the details and intricacies of mean-field theories in general and instead leave that for separate, future work [60].

In the following, we will first introduce the Manna Model and our observables in some detail. We will then present our findings for the various one, two and three-point correlation functions, with a focus on qualitative results, such as where scaling is found and whether it is quantitatively consistent with the exponents reported in the literature. We will not, however, attempt to extract very high accuracy estimates of exponents, but rather explore different observables and probe for consistency mostly using data collapses. The core of this work has been performed in $d = 1$ dimensions, but we have also

carried out extensive simulations in $d = 3$ and $d = 5$ dimensions, the latter in order to make contact with mean-field theory. In one dimension, the system sizes considered (linear extent up to $L = 4095$ depending on the observable) are small in comparison to past studies [18], but limited by the CPU-time needed to calculate some correlation functions. Given that transients in some versions of the Manna Model can be extremely long [37] and show significant scaling in L , large system sizes become computationally prohibitively expensive. This is a trade-off between small finite size corrections on the one hand and short transients and large statistics on the other. In dimensions $d = 3$ and $d = 5$, where memory requirements become a limiting factor too, system sizes were commensurate with the literature [19]. In the last section, we will summarise and discuss the numerical finding in particular in the light of recent theoretical progress.

II. MODEL, OBSERVABLES AND METHODS

The Abelian variant [61] of the Manna Model [62], used throughout the present work, is defined as follows: Sites \mathbf{x} of a lattice are occupied by $z_{\mathbf{x}}$ particles. A site \mathbf{x} occupied by not more than one particle, $z_{\mathbf{x}} \leq 1$, is said to be stable. If all sites are stable, $\forall_{\mathbf{x}} z_{\mathbf{x}} \leq 1$, the configuration is said to quiescent, otherwise active. The system is “driven” at times when it is quiescent by adding a particle to a site, say \mathbf{x}_0 , which may be fixed or selected at random, say, with uniform probability, which is then called “uniform driving”. The present study, however, focuses almost exclusively at centre driving, where \mathbf{x}_0 is fixed and chosen to be in the middle of the system. The fact that driving never takes place while the system is active is known as a separation of time scales. The succession of such particle additions, “drivings”, is said to occur on the *macroscopic* time scale.

If the particle number at a site exceeds the threshold of unity, *i.e.* $z_{\mathbf{x}} > 1$, then *two* particles are removed from the site and each placed randomly, independently and with uniform probability among its nearest neighbours. Such a redistribution is called a “toppling” and the arrival of a particle at a nearest neighbour a “charge”. The toppling of a driven site and the subsequent charge of a nearest neighbour may give rise to the latter exceeding the threshold. In each *microscopic* time step, every site \mathbf{x} that exceeds the threshold at the beginning of the microscopic time step redistributes each of two particles randomly, independently and uniformly among its nearest neighbours, until $z_{\mathbf{x}} \leq 1$, *i.e.* it topples $\lfloor z_{\mathbf{x}}/2 \rfloor$ times in that time step. This may include some sites toppling more than once in that time step. For example, $z_{\mathbf{x}} = 2$ topples to $z_{\mathbf{x}} = 0$ via one toppling and $z_{\mathbf{x}} = 5$ to $z_{\mathbf{x}} = 1$ via two topplings. The microscopic time step lasts until all sites initially exceeding the threshold have completed their toppling. Only then sites that subsequently exceed the threshold are considered at the beginning of the next microscopic time step. This *parallel* updating scheme in

“sweeps” provides an integer-valued microscopic time t which furnishes a convenient, well-defined and well justified way to estimate time-resolved observables. This original scheme is sometimes replaced by random sequential or proper Poissonian updating with random, exponentially distributed waiting times, which lends itself more naturally to a theoretical description.

For our purposes it proves most convenient for the microscopic time to be reset to $t = 0$ at each driving. In that sense we will regard microscopic time as the time passed since the last driving.

In the literature it is not always stated explicitly whether particles are redistributed all at once (non-Abelian, original definition [62]) or in pairs (Abelian definition [61]). The latter is more commonly implemented and has a number of theoretical advantages [4]. In particular, for a fixed (random) sequence of directions of particle redistributions, the final configuration of the Abelian Manna Model is independent of the order in which sites exceeding the threshold topple. This is not the case in the non-Abelian definition, as the number of particles leaving a site equals the number of charges it has received since the last toppling and up to the time of its toppling.

On a lattice that naturally divides into sublattices of sites that are mutual nearest neighbours, in particular on hypercubic lattices with suitable boundary conditions (see below), the scheme above has the additional advantage that all sites that are active at the beginning of a time step reside on the same sublattice. The number of active sites can therefore never exceed the size of the largest sublattice (which are equally or almost equally large) and given that no two sites within the same sublattice are nearest neighbours, they cannot charge each other while toppling. More importantly, if a site toppling during a particular time step were able to become active again during the same time step, a trail of computational implementation problems arises, namely of keeping track of the number of particles to topple in the present and in the future time steps. Without such safeguards, the number of topplings occurring at a site *during a particular microscopic time step* would be a function of the order of updates of sites, as the Abelian property states only that the distribution of *final states* is invariant under changes of updating order (strictly, changes of the order of initial charges), but says nothing about observables on the microscopic time scale (or, strictly, any other observables). To avoid any form of bias against certain sequences of events, one would probably resort to random sequential updating. Rather than doing that, we use hypercubic lattices that naturally divide into sublattices as described above.

In the description above, there is no loss of particles anywhere, in fact, only gain of particles added by the external driving. However, particle loss occurs at the boundaries of the lattice. For the following discussion it is easiest to think of such boundary sites as being situated adjacent to *sink sites*, where particles may accumulate without that site ever exceeding the threshold. The

particles are effectively lost at those sites and such sink sites are not subject to the lattice dynamics. The only lattices we have studied are those where each and every regular (*i.e.* non-sink) site has the same number of nearest neighbours, *i.e.* every boundary site is surrounded by suitable number of sink sites. In one dimension, a system consisting of L sites has sites $x \in \{1, 2, \dots, L\}$ with boundary sites $x = 1$ and $x = L$ adjacent to sink sites at $x = 0$ and $x = L + 1$. In two dimensions, a “frame” of sink sites may be thought of surrounding the lattice. However, in dimensions $d > 1$ we have applied periodic boundary conditions in all but one direction (which we refer to as x -direction), *i.e.* a site at $y = 1$ is adjacent to a site at $y = L'$, with L' the length of the lattice in the periodic direction. In the following, this is referred to as hyper-cylindrical boundary conditions. Coordinates in the periodic directions will be denoted by y_2, y_3, \dots, y_d (or just y where unambiguous), so that the full lattice vector $\mathbf{x} = (x, y_2, y_3, \dots, y_d)$, has components $x \in \{1, 2, \dots, L\}$ with open boundary conditions and $y_2, \dots, y_d \in \{1, 2, \dots, L'\}$ with periodic boundary conditions.

In order to implement centre driving, we have chosen L odd and the driving position $x_0 = (L+1)/2$. However, to maintain the segregation of toppling exclusively on either the even or the odd sublattice in dimensions $d > 1$, we had to choose an even length for the “perimeter” L' of the $d-1$ periodic directions, which we took as $L' = L+1$. The total number of sites in these systems is thus $N = L(L+1)^{d-1}$. Below, we will discuss the Manna Model in one dimension at length, presenting results for a large variety of observables. Only for a selected set of these observables we will present results from simulations in higher dimensions, namely $d = 3$ (just below the upper critical dimension $d_c = 4$, [9, 19, 43]) and $d = 5$ (above the upper critical dimension, where mean field theory should apply).

According to the updating rules above, particle trajectories are those of random walkers. The difference between the particles in the Manna Model and a random walker is the fact that the former may get stuck occasionally, when they arrive at an empty site. If each particle had attached to it a local clock that ticks only whenever the particle moves, then the particle’s trajectory with time labels of the local clock would be indistinguishable from that of a random walk. In the following, we will call moving particles “active”, the local (per-site) number of *topplings* “activity density” and their totality “activity”. Strictly, for any given time t activity density is the *number* of topplings $n(\mathbf{x}, t; \mathbf{x}_0, L) = \lfloor z_{\mathbf{x}}(t)/2 \rfloor$ that take place during parallel update t to $t+1$ at site \mathbf{x} after driving at site \mathbf{x}_0 . Because time is reset to $t = 0$ at driving, $n(\mathbf{x}, t = 0; \mathbf{x}_0, L)$ vanishes everywhere except possibly but not necessarily (as the driving is not bound to result in activation) at $\mathbf{x} = \mathbf{x}_0$, *i.e.* $n(\mathbf{x}, t = 0; \mathbf{x}_0, L) \propto \delta_{\mathbf{x}, \mathbf{x}_0}$. It is rare that a large fraction of sites is active in parallel, so $n(\mathbf{x}, t; \mathbf{x}_0, L)$ is generally sparse in \mathbf{x} . To distinguish different histo-

ries $n(\mathbf{x}, t; \mathbf{x}_0, L)$ after driving the system for the i th time, we use the notation $n_i(\mathbf{x}, t; \mathbf{x}_0, L)$. The average of $n_i(\mathbf{x}, t; \mathbf{x}_0, L)$ over many realisations $i = 1, 2, \dots, M$ is referred to as the (time-dependent) activity density (the count per site) or response propagator $G(\mathbf{x}, t; \mathbf{x}_0, L)$ for a system of size L , see Eq. (9) below.

Particles that are not moving are part of the “substrate”, *i.e.* the “backdrop” in front of which activity unfolds. These inactive, immobile particles may be referred to as “substrate particles” and their density, *i.e.* fraction of singly occupied sites, as the substrate density either spatially resolved as $D_s(\mathbf{x}; \mathbf{x}_0, L)$ or averaged as ζ_L , Eq. (4), with $\lim_{L \rightarrow \infty} \zeta_L = \zeta_\infty$.

In each toppling, *two* particle moves occur. Each particle contributes (with weight 1/2) to the activity density (only while moving away). A time integral over the activity density hides the complicated relationship between local time and actual microscopic time and the resulting space-dependent density is that of a collection of random walkers with a diffusion constant D corresponding to one lattice spacing squared per local time step (as moves occur only when local time ticks away), $D = 1/(2d)$ [63]. Strictly, the activity density is *half* the density of random walker trajectories emanating from the driving site.

The totality of all topplings triggered by driving a quiescent system is called an avalanche. If the driving occurs at an empty site, $z_\mathbf{x} = 0$, so that it remains stable and no toppling takes place at all, an avalanche size of 0 is recorded. Otherwise, the avalanche size s is the total number of topplings that are triggered by adding a particle as the system is driven. To indicate the instantaneous avalanche size in an individual realisation, indexed by i , we may use the notation s_i . Following from the discussion above, the expected avalanche size is given by half the escape time¹ of a random walker from a lattice, which can (depending on boundary conditions) be calculated in closed form [63]. With hyper-cylindrical boundary conditions as described above, the expected avalanche size is simply [4]

$$\langle s \rangle = \frac{x_0(L + 1 - x_0)}{4D} \quad (1)$$

in a d -dimensional lattice (periodic in $d-1$ dimensions and open in one of linear extent L) driven at distance x_0 away from the open boundary.

The number of parallel updates needed to make the system quiescent again after driving it defines the avalanche duration T , individually denoted by T_i for the duration of the i th avalanche. If no toppling takes place we define $T_i = 0$. We may thus write

$$s_i = \sum_{t=0}^{T_i-1} n_i(\mathbf{x}, t; \mathbf{x}_0, L) . \quad (2)$$

¹ The escape time of a random walker gives the number of its moves, which is half the number of topplings, as each toppling causes two moves.

As opposed to the Oslo Model [64], where particles move deterministically as in the (BTW) Sandpile Model [3] but with the difference that the threshold is reset randomly, the Manna Model has no strict upper bound for the avalanche size and the avalanche duration, as particles may keep toppling back and forth indefinitely. As we know from the mapping to random walker trajectories mentioned above, this has no serious implications as far as the numerics are concerned (avalanches eventually terminate just as walkers eventually dissipate), but algebraically, *e.g.* in terms of expressing the dynamics using Markov matrices [4], a number of difficulties arise (see also Appendix A).

Avalanche size and avalanche duration are typical observables in the study of SOC models. Beyond a lower cutoff, the probability density function of both observables displays scaling. Specifically, the probability $P_s(s; L)$ of observing an avalanche of size s large compared to some lower cutoff in a system of linear size L displays *simple (finite size) scaling* [14], that is, it scales like $a_s s^{-\tau} \mathcal{G}_s(s/(b_s L^D))$ with metric factors a_s and b_s , scaling function \mathcal{G}_s and two universal exponents τ and D . The former, τ is known as the avalanche size exponent, the latter as the avalanche dimension D . Correspondingly, the avalanche duration has probability distribution $P_T(T; L) = a_T T^{-\alpha} \mathcal{G}_T(T/(b_T L^z))$ with avalanche duration exponent α and dynamical exponent z .

All measurements reported below are taken in the stationary (or steady) state, which the Manna Model develops into over long times. Because of the two timescales (microscopic and macroscopic) and an obvious dependence of observables on the microscopic time passed since driving, stationarity may appear somewhat awkward to define properly. To do this, we introduce $P_i(\{z\})$, which denotes the probability of finding the system in a certain quiescent configuration $\{z\}$ (the set $\{z\}$ denoting all particle numbers on all sites) after driving it i times and allowing all avalanching to cease. The system is stationary if $P_{i+1}(\{z\}) = P_i(\{z\})$, *i.e.* in case of invariance of $P_i(\{z\})$ under further drives. We will use “stationary state”, “steady state” and the invariant joint probability $P_i(\{z\})$ synonymously in the following. In the stationary state (or, equivalently, sampling initial states from $P_i(\{z\})$), the expectation of any observable taken after t microscopic time steps after the i th drive, will be identical to that after t time steps after the $i+1$ th drive. This state is what we have attempted to characterise numerically below.

However, we do not aim to estimate or determine $P_i(\{z\})$ explicitly. Rather, as in most Markov Chain Monte-Carlo procedures, we initialise our system once (or a small number of times, letting multiple instances run embarrassingly parallel) and trigger a large number of avalanches, hoping that after passing (and dismissing as transient) many avalanches the resulting configuration is far more representative (*i.e.* likely) than the initial configuration, so that all further evolution of the system may be considered as an exploration of the stationary state,

with each new configuration being the initial configuration for the next avalanche. Rare configurations may still occur, but with suitably low frequencies. The present argument is inherently quantitative, as *every* configuration (modulo a certain conserved parity in certain settings, see Appendix B2) is recurrent, *i.e.* configurations transcended at (supposed) stationarity are rare ones, not strictly transient ones.

It may appear natural to start the Manna Model from an empty lattice [62], but because the substrate density is close to unity at least in $d = 1$ dimensions, it pays off to start from full occupation. A similar approach has been proposed for the Oslo Model [65, 66] (and a more sophisticated one recently [40]); in that case, the distribution of configurations after a single further charge is exactly the stationary $P_i(\{z\})$. We are not aware of a similar proof for the Manna Model. In some cases, we have initialised the lattice with bulk density (as estimated in preliminary runs or as published [18, 19]) throughout. After initialisation, we generally dismissed a generous number of typically about 10^6 avalanches as transient.

Measurements of most relevant observables were taken as averages over 100 or so “chunks” of about 10^5 avalanches each. By monitoring in particular (but not exclusively) moments of the avalanche size we were able to determine whether the transient was over, *i.e.* satisfy ourselves that “equilibration” had been achieved. Although analytically known, the first moment is a somewhat misleading indicator for that. We focused instead on higher moments, taking as the end of the transient a small multiple of the number avalanches from when on the estimate of the moment is no longer monotonic in the number of avalanches since initialisation. Increasing the length of the transient beyond that has no noticeable effect on the estimates (within the estimated error) and we are therefore confident that the SOC Manna Model is not suffering from the same dependence on the transient as recently reported for the fixed energy sandpile version in one dimension [37]. We further verified that our numerical findings are consistent with published data [18, 19, 44, 67–69].

After the transient, the chunks can always be merged to create estimates based on bigger chunks, so that each chunk exceeds the correlation time on the macroscopic time scale (see Sec. III C 7), which is orders of magnitude shorter than the transient. Chunks of that size may be treated as statistically independent. On the basis of about 100 such chunks statistical errors are easily calculated. As a random number generator we used the Mersenne Twister [70].

All numerical results stated in the following are based on such chunk-averages [4]. To ease notation (and discussion) we will not distinguish numerical estimators and exact population averages, which we may denote by $\langle \cdot \rangle$ (usually for avalanche sizes and duration averaged across many avalanches). Although we spend much time on only one dimension, we will use vectors such as \mathbf{x} and \mathbf{x}_0 to denote positions, and use scalars such as x and x_0

only if the result is either restricted to one dimension, or if the only relevant component of the vectors in our hyper-cylindrical lattice is the distance from the open boundary.

Many of the results below derive from observables that are defined for the entire lattice, which suggests that expectation values are calculated on the basis of scanning the entire lattice. Because this is computationally very costly, we made extensive use of stacks (that store the list of sites active at a given time t) and “integration by parts”, as the time series a_t for $t = 0, \dots, T - 1$ obeys [4]

$$\sum_{t=0}^{T-1} a_t = T a_T - \sum_{t=1}^T t(a_t - a_{t-1}), \quad (3)$$

with arbitrary a_T , in particular $a_T = 0$. The right hand side is computationally much less costly to calculate in cases where changes $a_t - a_{t-1}$ of a_t are rare and naturally tracked (for example if a_t represents the occupation of a site in the quiescent state). The computational gain may depend on the dimensionality of the lattice; if, for example, $a_t - a_{t-1}$ are changes in the local occupation of the lattice, then on average $\propto L^2$ changes have to be tracked between avalanches, compared to scanning a lattice of size L^d .

A. Observables

The main objective of the present work is to characterise spatio-temporal correlation functions. In field theoretic terms, we are considering both response functions and correlation functions, but also, effectively, three-point functions.

As far local degrees of freedom are concerned, the particle numbers (or densities) observed at a site naturally divide into two “categories”. Firstly, there is the number of immobile particles (or “substrate particles”) residing at any site, unambiguously measured in the quiescent state, secondly the number of particles moving, which is always a multiple of 2, to be precise $2 \lfloor z_{\mathbf{x}}(t)/2 \rfloor$ for a site carrying $z_{\mathbf{x}}(t)$ particles. This latter observable is more elegantly expressed as the number of topplings or the “activity” occurring at any site at time t over the course of an avalanche, $n(\mathbf{x}, t; \mathbf{x}_0, L) = \lfloor z_{\mathbf{x}}(t)/2 \rfloor$ as introduced above. As each toppling involves two particles leaving the site, the activity $n(\mathbf{x}, t; \mathbf{x}_0, L)$ is thus half the count of active particles. These counts of immobile (substrate) particles and of the instantaneous topplings (activity) can be correlated in time and space. We will not mix them in the following, although that would give rise to very interesting observables, such as the activity as a function of local particle density. We will use the notion of “count” (per site) and “density” synonymously.

All of these observables (the “counts”) must be considered as a function of the driving position, \mathbf{x}_0 . We will consider (almost) exclusively centre driving (for the

definition see above). The driving position makes, effectively, any local count a two-point correlation function, namely the count somewhere as a function of the driving somewhere else. In case of the immobile particle count, it turns out that observables are (under certain conditions) independent of the position of driving. As far as activity is concerned, the opposite is the case, *i.e.* location and time of activity is quite obviously correlated to the position and time of driving. Driving at a site results in activity at that site with a probability equal to the probability of that site being occupied, which displays a very shallow spatial profile, *i.e.* in the bulk, the probability of a site being occupied has very little dependence on its position. Up to this pre-factor, the activity resulting from driving the system may therefore be seen as the response (that is the activity resulting from creating activity somewhere else).

We will also consider higher correlation functions, such as the immobile particle count at two different points in space given the driving at the centre. We will usually choose one of the two points to be the driving site. Similarly, we will consider correlations in the activity, given driving somewhere else and again, we will choose one site (probed for activity possibly at a later time) to coincide with the driving site.

The decomposition of the system into an even and an odd sublattice, as discussed above, results in certain correlation functions vanishing — if site x topples at time t , site y may topple at time t' only if $y + t'$ has the same parity as $x + t$.

Many of the results derived below will be based on collapses, which are often not very sensitive as far as estimates of exponents are concerned. Rather, they give qualitative results, indicating that scaling takes place and whether exponents found are compatible with those in the literature.

In the following we first present a mean field theory before discussing the results in detail, defining the various observables as we proceed, first through the results in one dimension (Sec. III) and then in three and five dimensions (Sec. IV). We will conclude with a discussion of the results in Sec. V.

Briefly summarising the key results, we will demonstrate that correlations in the substrate (*i.e.* in the distribution of immobile particles) are quite faint and that the density profile of immobile particles that the system adopts is (essentially) independent of the driving and very shallow. In one dimension, we can qualify this statement further by providing an analytical proof. In our interpretation, this result suggests that the notion of “self-organising to the critical state” — namely the one and only critical state, given by the invariant ensemble $P(\{z\})$ and resulting in a particular particle density profile — is indeed justified. Further, we will show that the activity profile (the response function) is essentially Gaussian in space and that its spreading is governed by the exponents as captured by the avalanches normally analysed in SOC. Remarkably, this link seems somewhat

flawed in one dimension with inconsistencies occurring within results presented in the following and in relation to the literature. We believe that validating the relation between the scaling of avalanches and the scaling of spatio-temporal correlation functions is crucial for the understanding of SOC and the significance of avalanches as historically studied. Notably, the correlation length of the activity as well as of the weak correlations in the substrate are linear in the system size, as expected in a critical, finite system.

B. Mean Field Theory

There is surprisingly little effort in the literature to devise any spatially extended mean field theory (MFT). This is probably because mean field theories are designed to ignore certain interactions and thus correlations and fluctuations. If spatial correlations are neglected, one may be tempted to disregard space as a whole. However, it has been known for a long time that boundaries are fundamental to SOC, as particles in bulk-conservative models can only leave via the boundary [55, 56]. Some authors have attempted to mimic their effect by introducing a bulk dissipation rate [52, 57–59].

As far as the spreading of activity is concerned, one may think of it as a spatially extended branching process, whereby activity (similar to active particles) moves on a lattice, ceases upon arrival at a site with probability 1/2 or doubles otherwise, with both “offspring” being redistributed randomly and independently at nearest neighbours. This MFT model, a branching random walk which arises as the tree level in a recent field-theoretic study [42], differs from the Manna Model crucially in the mechanism by which activity doubles — in the Manna Model this is dependent on the occupation number at the site, and that is in turn dependent on whether or not activity has ceased at the site previously. The particle number is conserved in the Manna Model, but noticeably activity only in the sense that its time-integral is identical to that of the density of (bulk-conserved) random walkers with the diffusion constant as stated above. This last point is also captured by the MFT model. We are planning to publish a detailed analytical study of the MFT model soon [60]. For comparison with the numerics obtained in the present study, we will occasionally draw on this MFT model, deriving some of its features in passing.

III. RESULTS IN ONE DIMENSION

A. Quiescent state

Because of the separation of time scales, avalanches are instantaneous on the time scale of driving (the macroscopic time scale). Observing therefore the lattice at any

given macroscopic time, it is quiescent.² In fact, the connection between macroscopic and microscopic time scale is sometimes made by devising an infinitely slow Poissonian rate [71], so that the system is almost surely quiescent at any randomly chosen microscopic time. It is thus natural to attempt to identify the signature of SOC in the quiescent state. In the following, we will study the one-point and two-point correlations of immobile (inactive) particles that make up those quiescent configurations.

The one-point correlation $D_s(\mathbf{x}; \mathbf{x}_0, L)$ is the expected count (at site \mathbf{x}) or density of inactive particles as a function of position \mathbf{x} and the position \mathbf{x}_0 where the driving takes place, in a system of linear extent L . This function is below referred to as the “density profile”. The measurements are taken at quiescence (when no avalanche is running) and in the stationary state. Strictly $D_s(\mathbf{x}; \mathbf{x}_0, L)$ is a response function of the density of inactive particles at \mathbf{x} in response to a driving taking place at \mathbf{x}_0 in the presence of an initial distribution of inactive particles and in the long time limit (when the avalanche has ceased). Because we are measuring in the stationary state, the density of inactive particles is invariant under further external driving, *i.e.* there is no time-dependence (which does not mean that the arrangement of inactive particles remains unchanged under driving, but only that its *joint probability distribution* is not changing). Since sites can be occupied by at most one particle, the expected particle count at a site is the probability of finding a particle there at all.

The sum

$$\zeta_L = N^{-1} \sum_{\mathbf{x}} D_s(\mathbf{x}; \mathbf{x}_0, L) \quad (4)$$

over all N sites is the spatially averaged (expected) density of particles in the system at stationarity (as $D_s(\mathbf{x}; \mathbf{x}_0, L)$ is taken at stationarity). As can be seen in Fig. 1(a), in large enough systems $D_s(\mathbf{x}, \mathbf{x}_0, L)$ shows little variation in the bulk, as boundary effects decay, according to Fig. 1(b), independent of the system size, so that $D_s(\mathbf{x}, \mathbf{x}_0, L)$ converges as $L \rightarrow \infty$ for fixed \mathbf{x} and \mathbf{x}_0 , *i.e.* the shoulder of $D_s(\mathbf{x}, \mathbf{x}_0, L)$, visible for small x , is reproduced with increasing system size.

The inset of Fig. 1(b) suggests that the deviation of the density from the bulk value follows a power law as a function of the distance away from the boundary, $D_s(\mathbf{x}; \mathbf{x}_0, L) - \zeta_\infty \propto |\mathbf{x}|^{-0.72}$, over a characteristic scale that is linear in the system size (probably related to the scaling of the correlations seen below in the inset of Fig. 2(b)). Because the amplitude of the deviation quickly converges with increasing L , this is diffi-

cult to confirm in the bulk of large systems, as any deviations eventually drown in noise. This is a common theme in substrate features: Amplitudes do not display finite size scaling. The inverse of the observed exponent, $1/0.72 = 1.388\dots$ should be ν_\perp [9], estimated below to be 1.395(3). Bonachela and Munoz have studied a range of observables in the Manna Model as a function of the distance from the boundary [72] (also [73]) and Grassberger, Dhar and Mohanty [40] recently found the same scaling in the Oslo Model [64], which is thought to be in the same universality class [74]. They found an exponent of approximately 0.75, which is still compatible with the present data.

The density is bounded from above and from below, but nevertheless displays a small decrease with system size at the boundary sites ($x = 1$ and $x = L$). Because of the lack of scaling of the amplitude of the deviation, the drop in the rescaled plot Fig. 1(a) from the bulk density towards the lower density at the boundaries gets increasingly sharp with system size. For very large system sizes, the density in the bulk may therefore be approximated nearly everywhere by ζ_L , Eq. (4). Numerically, the best known estimate for its value in the limit of $L \rightarrow \infty$ is $\zeta_\infty = 0.9488(5)$ [18], which our value of 0.94882(1) is compatible with. We have extracted that from our data by fitting results for $L = 31, 63, \dots, 4095$ against

$$\zeta_\infty + a_1 L^\alpha + a_2 L^{\alpha-1/2} + a_3 L^{\alpha-1} \quad (5)$$

which also produces a very good goodness of fit (about 0.64) and generates, in passing, an estimate of $\nu_\perp = -1/\alpha$ of 1.395(3) which compares well with previous estimates of 1.35(9) [9].

That the density profile shows so little structure suggests that it does not even reveal the position \mathbf{x}_0 where the driving takes place, *i.e.* that $D_s(\mathbf{x}, \mathbf{x}_0, L)$ is independent of the driving position. Numerically, this is indeed confirmed. The inset of Fig. 1(a) shows the difference $D_s(\mathbf{x}/L; (L+1)/2, L) - D_s(\mathbf{x}/L; (L+1)/4, L)$ between the density profile of $L = 511$ driven at $x_0 = (L+1)/2$ and at $x_0 = (L+1)/4$. This data is fully compatible with the hypothesis that the profile does not depend on the driving position.

The stationary state, *i.e.* the invariant probability of finding a certain profile of immobile particles, could in principle be dependent on the way (where and how) the system is driven and also on the initialisation. For the system sizes considered here ($L \geq 63$), we do not find any such dependence. The resulting profile is independent of \mathbf{x}_0 and other details of the driving.

In Appendix A and more particularly Appendix B, we discuss an analytical approach to the stationary state. There, we show that in one dimension *the stationary state reached by driving the Manna Model at the first site, $x_0 = 1$, at the last site, $x_0 = L$, or globally with positive probability at every site (such as uniform driving), is identical and unique.* This stationary state is the *unique invariant distribution of configurations that is common to all driving sites.* This is a remarkable feature that is in

² In the following we distinguish the “quiescent state”, which refers to the system being quiescent, “quiescent configurations” which is any of the 2^N configurations that are quiescent and the “stationary state” or “steady state” which means that the probability of any such configuration is invariant under driving (at a certain site).

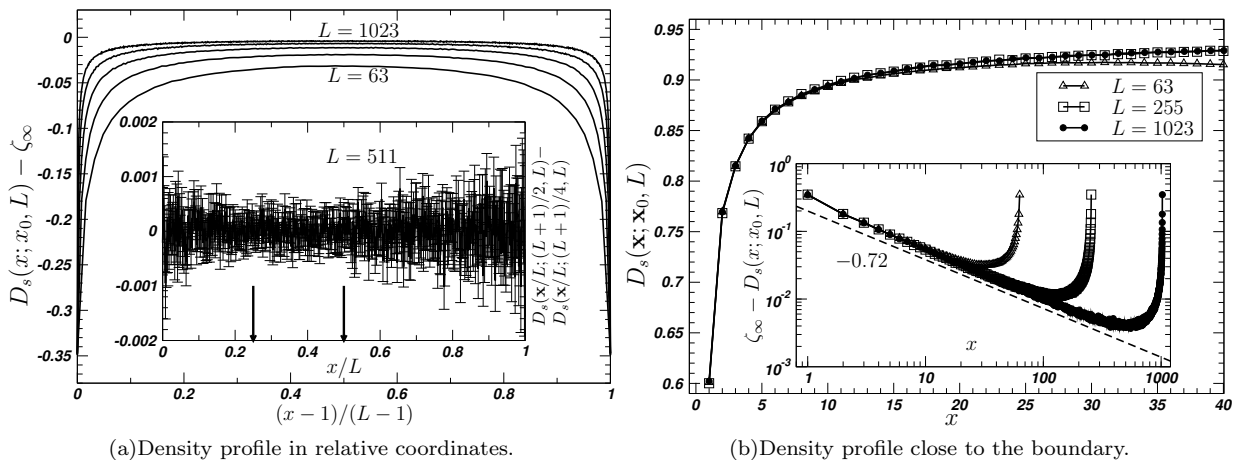


FIG. 1: The density of inactive (immobile, substrate) particles during quiescence in the stationary state, $D_s(\mathbf{x}; \mathbf{x}_0, L)$, for different system sizes L and as a function of position x (full lines to guide the eye, error bars negligible unless shown). (a) Plotting $D_s(\mathbf{x}; \mathbf{x}_0, L) - \zeta_\infty$ versus the relative position $(x-1)/(L-1)$ with $x \in \{1, \dots, L\}$ reveals that deviations of the density away from the asymptotic value ζ_∞ are confined to the regions close to the boundary. With increasing system size, an increasing fraction of sites is occupied with a probability that is arbitrarily close to ζ_∞ . The data in the main panel is for $x_0 = (L+1)/2$ (centre driving). The inset shows for $L = 511$ the difference between the density profile for different driving positions (marked by arrows), $D_s(\mathbf{x}/L; (L+1)/2, L) - D_s(\mathbf{x}/L; (L+1)/4, L)$, *i.e.* driving at $x_0 = (L+1)/2$ and at $x_0 = (L+1)/4$. This deviation clearly remains within the numerical error (*i.e.* can be fitted against 0 with almost unity as goodness of fit). Errors are smaller near the driven sites x_0 due to better statistics. (b) The density profile close to the boundary quickly converges with increasing L , as shown here for $L = 63, 255, 1023$. The “shoulder” in the profile does not scale, in the sense that densities differ visibly among different *small* L only further in the bulk (as can be seen for $L = 63$ and $L = 255$, but for $L = 255$ and $L = 1023$ only at bigger x and then much less pronounced). The inset shows the scaling of the difference $D_s(\mathbf{x}; \mathbf{x}_0, L) - \zeta_\infty$ as a function of x , revealing an intermediate powerlaw dependence with exponent of approximately -0.72 (dashed line).

perfect agreement with the notion of self-organisation in the Manna Model, namely that there is one and only one stationary state (a distribution of configurations) that the model evolves towards, irrespective of whether it is driven at a boundary site or at all sites with positive probability.

However, as discussed in Appendix B3, it turns out that the invariant probability is in fact two-fold degenerate (and can in principle be even more degenerate), as there is a conserved quantity if L is odd and x_0 is even (as in the present case of odd L and centre driving). This degeneracy was not picked up in the numerics mentioned above, because it is visible in the density profiles $D_s(\mathbf{x}/L; \mathbf{x}_0, L)$ only in very small systems (see Fig. 28). For systems of size 31 and bigger it seems numerically impossible to differentiate between the stationary states resulting from these different initial conditions and one will therefore arrive always at the (numerically) same density profile $D_s(\mathbf{x}/L; \mathbf{x}_0, L)$.

B. Correlations

In the stationary state, not only the one-point density $D_s(\mathbf{x}; \mathbf{x}_0, L)$ is invariant, but in fact the probability of finding the system in any of its 2^N configurations. Indeed, the analytical results mentioned above (see Appendix B) give access also to n -point correlation func-

tions (in principle even to the response function and the “temporal shape of the avalanche” discussed below) — unfortunately, however, only for very small system sizes. These results are therefore not shown.

Carrying on with numerical results for systems of size $L \geq 63$, in the following we analyse two point correlations in the occupation by inactive particles. If $P_s^{(2)}(\mathbf{x}_2, \mathbf{x}_1; \mathbf{x}_0, L)$ is the joint probability of finding a particle at \mathbf{x}_1 and another one, at the same (macroscopic, quiescent) time, at \mathbf{x}_2 after driving at \mathbf{x}_0 , then

$$C_s(\mathbf{x}_2, \mathbf{x}_1; \mathbf{x}_0, L) = P_s^{(2)}(\mathbf{x}_2, \mathbf{x}_1; \mathbf{x}_0, L) - D_s(\mathbf{x}_2; \mathbf{x}_0, L)D_s(\mathbf{x}_1; \mathbf{x}_0, L) \quad (6)$$

is the connected two-point correlation function. As shown in Fig. 2, small anti-correlations are present in the distribution of inactive particles. However, there is clearly no finite size scaling of the amplitude of these correlations, which cannot possibly increase indefinitely as the density is bounded everywhere. In fact, the anti-correlations die off very quickly in space. Despite being slightly *less* pronounced for large system sizes, they seem to converge to a finite value for increasing L , *i.e.* they are not merely a finite size effect. Because the spatial scale of the anti-correlation does not vary significantly with the size of the system, this correlation function does not collapse under any non-trivial rescaling. However, for distances $|x-y|$ of less than about 50 sites $C_s(x, y; \mathbf{x}_0, L)$

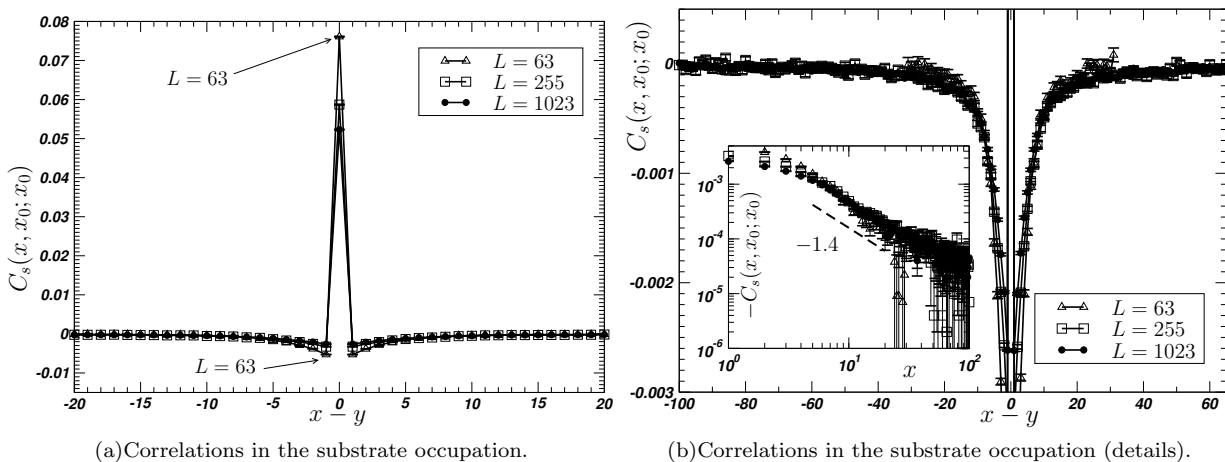


FIG. 2: The correlations in occupation (density) by inactive particles, $C_s(x, y; \mathbf{x}_0, L)$, Eq. (6), versus the distance $x-y$, measured during quiescence and at stationarity. The system is driven at the centre site $x_0 = (L+1)/2$, which is also the location where one of the densities is taken, $y = x_0$. Correlations are in fact anticorrelations (with an amplitude decreasing with increasing system size), because the dynamics depletes sites of particles, depositing them at neighbouring sites. (a) Correlations are slightly more pronounced for the *smaller* systems, decay very quickly and are barely noticeable beyond 5 to 10 sites. (b) On a very fine scale correlations are more discernible, and in fact might decay like a powerlaw, as shown in the inset (the dashed line shows a powerlaw with exponent -1.4). As data for different system sizes L collapse on the same plot without rescaling, there is no non-trivial finite size scaling in these correlations (other than possibly in the cutoff, see main text). The data in (a) and (b) are identical but shown on different scales.

shows some noisy linear behaviour in a double logarithmic plot, as shown in the inset of Fig. 2(b). This may suggest a power law dependence of $C_s(x, y) \propto |x-y|^{-1.4}$, albeit with a very small amplitude of about one third of the (local) variance $C_s(\mathbf{x}_0, \mathbf{x}_0; \mathbf{x}_0, L)$, which is itself a small quantity (as discussed below). The power law-like behaviour persists for $y \neq x_0$ and, as a *second* moment, may be related to the exponent of -0.72 found in the scaling of the deviation of the density from the bulk value, away from the boundary Fig. 1(b) and thus expected to be $-2/\nu_\perp \approx 1.48(10)$ [9].

Given the small amplitude of the anti-correlations, which seems to converge from above with increasing system size, and the large relative statistical error, it is fair to say that the anti-correlations are not very pronounced and difficult to measure. There is clearly no scaling of the amplitude with system size and no rescaling needed to achieve the (noisy) collapse of Fig. 2(b). This lack of scaling is similarly found in the density profile shown in Fig. 1(b), yet the exponent roughly characterising the scaling of the correlations is about twice that characterising the decay of the density difference from the bulk value away from the boundary. Similar power law scaling is observed in in three and five dimensions (Figs. 17(b) and 23(b) respectively), but the data is obviously plagued by statistical noise. Future studies, in particular using more sophisticated observables and numerical techniques, may be more successful in identifying features in the substrate whose amplitude scales up with increasing system size and that (unlike, say, the shoulder in Fig. 1(a) localised close to boundary) remain visible even when the (apparent) lattice spacing is very small compared to the range

of observation.

Within statistical error the variance $C_s(\mathbf{x}_0, \mathbf{x}_0; \mathbf{x}_0, L)$ coincides with the Bernoullian $D_s(\mathbf{x}_0; \mathbf{x}_0, L) - D_s(\mathbf{x}_0; \mathbf{x}_0, L)^2$ (which is a small quantity as $D_s(\mathbf{x}_0; \mathbf{x}_0, L)$ is close to unity, $\zeta_\infty = 0.9488(5)$). To explore the correlations apparent in Fig. 2(b) further, we have also measured the distribution of distances between unoccupied sites, measured as the number d_0 of consecutively occupied sites between any two unoccupied ones. If occupation is governed by a Bernoulli process, the frequency $P_0(d_0)$ of such distances d_0 should follow $(1 - \zeta_L)\zeta_L^{d_0}$. As shown in Fig. 3, a semi-logarithmic plot produces a mixed picture. On small scales (small d_0 or small system size) significant deviations are apparent, but with increasing system size, the large scale behaviour seems to approach the expected exponential, although with a higher density of unoccupied sites (a steeper slope). Very long stretches of continually occupied sites are very rare and their statistics therefore subject to significant noise. That barely any correlations are visible on the large scale is nevertheless consistent with the observation of hyperuniformity discussed in the following.

Through a different observable, there is already clear evidence for anti-correlations in the fixed energy variant of the Manna Model, as Hexner and Levine [75] observed hyperuniformity [76] in the substrate particle density and Basu *et al* identified “natural long-range correlations in the background” [37].

Hyperuniformity refers to the (fast) scaling of the variance of the particle density with the volume over which this density is estimated. In one dimension, the instan-

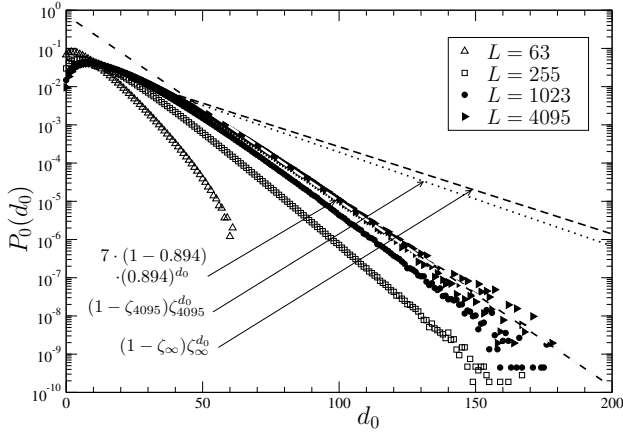


FIG. 3: Semi-logarithmic plot of the distribution $P_0(d_0)$ of distances d_0 between consecutive unoccupied sites (separated by d_0 occupied ones) in one dimension for various system sizes. If sites are occupied independently, the data forms a straight line. The thick (black and white) dashed line through the data for $L = 4095$ is $7 \cdot (1 - 0.894) \cdot (0.894)^{d_0}$, the other (black) dashed line the Bernoullian $(1 - \zeta_\infty)\zeta_\infty^{d_0}$ using the asymptotic density $\zeta_\infty = 0.9488(5)$. The dotted line shows $(1 - \zeta_{4095})\zeta_{4095}^{d_0}$ with $\zeta_{4095} = 0.945028(3)$.

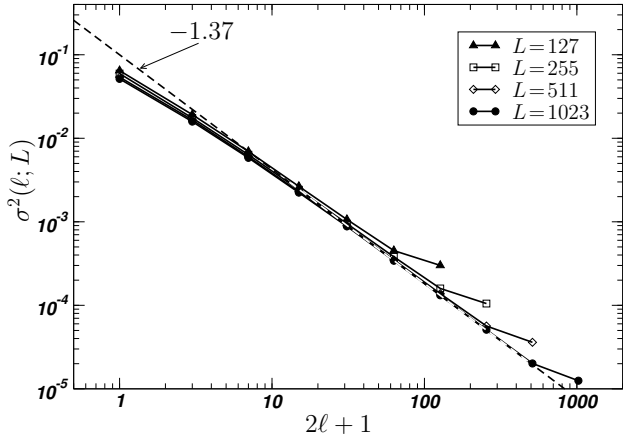


FIG. 4: Double logarithmic plot of the variance $\sigma^2(\ell; L)$ of the window-averaged (size ℓ) substrate particle density in one dimension for a range of system sizes L . The dashed line shows the approximate scaling exponent -1.37 , which is steeper than $\sigma^2 \propto \ell^{-1}$ expected when sites are independently occupied.

taneous density might be measured as a window average $(\frac{1}{2\ell+1} \sum_{x=x_0-\ell}^{x_0+\ell} \dots)$ symmetrically around the driving site at the centre. Its variance is given by

$$\sigma^2(\ell; L) = \frac{1}{(2\ell+1)^2} \sum_{x_1, x_2=x_0-\ell}^{x_0+\ell} C_s(\mathbf{x}_2, \mathbf{x}_1; \mathbf{x}_0, L) \geq 0, \quad (7)$$

and so $\sigma^2(\ell; L) \propto (2\ell+1)^{-1}$ if sites are independently occupied. In general, if $C_s(\mathbf{x}_2, \mathbf{x}_1; \mathbf{x}_0, L)$ was positive everywhere, $\sigma^2(\ell; L)$ could not decay faster than ℓ^{-1} . If it

does, this is referred to as hyperuniformity. The variance $\sigma^2(\ell; L)$ can always be written as

$$\sigma^2(\ell; L) = \frac{\sigma^2(0; L)}{(2\ell+1)} + \sum_{\substack{x_1, x_2=x_0-\ell \\ x_1 \neq x_2}}^{x_0+\ell} C_s(\mathbf{x}_2, \mathbf{x}_1; \mathbf{x}_0, L) \quad (8)$$

with $\sigma^2(0; L) = C_s(\mathbf{x}_1, \mathbf{x}_1; \mathbf{x}_0, L)$, the correlation at $x_2 = x_1$, which is bound to be non-negative. At the heart of hyperuniformity is the behaviour of the sum in Eq. (8). Even if $C_s(\mathbf{x}_2, \mathbf{x}_1; \mathbf{x}_0, L)$ is negative for $x_2 \neq x_1$, it might still be subleading, resulting in $\sigma^2(\ell; L) \propto \ell^{-1}$. However, as illustrated in Fig. 4, we found a scaling of $\sigma^2(\ell; L) \propto \ell^{-1.37}$, for $L = 1023$ in an intermediate range of the width of about $31 < 2\ell+1 \leq 511$. We believe this value of the exponent is compatible with $-1.425(25)$ found by Hexner and Levine for the same quantity in the fixed energy version of the Manna Model.

Ignoring the contributions from $C_s(\mathbf{x}_2, \mathbf{x}_1; \mathbf{x}_0, L)$ for small $|x_2 - x_1|$ or, equivalently, assuming that the positive contributions at $x_2 - x_1 = 0$, which scale like ℓ^{-1} , are cancelled by negative ones from small, positive $|x_2 - x_1|$ (where it does not follow a power law), the scaling of $\sigma^2(\ell; L)$ in large ℓ is due to the (intermediate) asymptote of $C_s(\mathbf{x}_2, \mathbf{x}_1; \mathbf{x}_0, L)$, which means that the exponent of -1.4 in the inset of Fig. 2(b) is to be compared to -1.37 and $-1.425(25)$, found for $\sigma^2(\ell; L)$ here and in [75], respectively. Standard finite size scaling indeed suggests $\sigma^2(\ell; L) \propto \ell^{-2/\nu_\perp}$ [40]. Notably, the scaling of $C_s(\mathbf{x}_2, \mathbf{x}_1; \mathbf{x}_0, L)$, which has to be cut off when $|x_2 - x_1|$ exceeds L and the absence of finite size scaling of the amplitude are compatible with hyperuniformity. Our numerics indicate that the scaling of $\sigma^2(\ell; L)$ persists up to $\ell \approx L/2$, which suggests that the scaling of $C_s(\mathbf{x}_2, \mathbf{x}_1; \mathbf{x}_0, L)$ is long-ranged, possibly of the form $|x_2 - x_1|^{-1.4} \mathcal{C}(|x_2 - x_1|/L)$, with a cutoff length linear in the system size. Algebraic correlations of the substrate have first been observed analytically in the seminal work by Majumdar and Dhar [22] on the paradigmatic Abelian Sandpile Model [3, 20] and thus may be considered the fingerprint of the critical state.

C. Active state

The features in the active state, *i.e.* during the course of an avalanche, are much richer not least due to the additional time-dependence. In the following, we will follow roughly the order of observables above. The one-point correlation function is, as above, really the response function $G(\mathbf{x}, t; \mathbf{x}_0, L)$, as defined below. It is the activity density at \mathbf{x} and (microscopic) time t after the system was driven at \mathbf{x}_0 at time 0. Numerically, $G(\mathbf{x}, t; \mathbf{x}_0, L)$ is the estimated number of topplings of site \mathbf{x} at time t after an initial charge at x_0 .

As explained above, this frequency is measured by recording the number $n(\mathbf{x}, t; \mathbf{x}_0, L)$ of topplings that occur at each lattice site \mathbf{x} during the t th sweep across

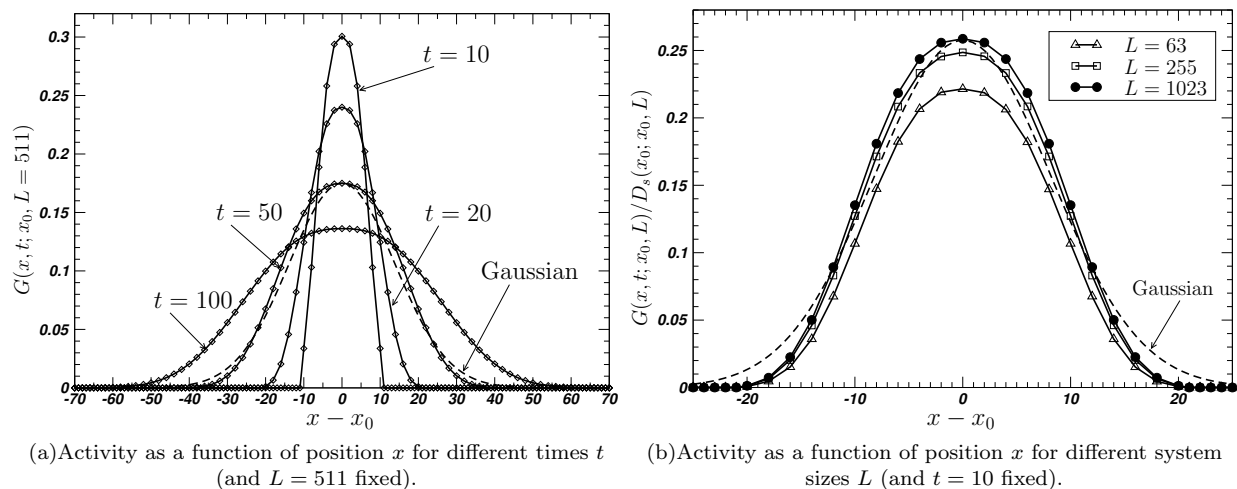


FIG. 5: The activity $G(x, t; x_0, L)$ in one dimension as a function of position x , for centre driving, $x_0 = (L + 1)/2$, at various times and for different system sizes L (for a collapse see Fig. 11). Actual data are shown as symbols, which are connected by a line as guide for the eye. Data points that necessarily vanish because of parity conservation (see text) have been omitted. (a) The activity as a function of the distance from the driving site, $x - x_0$, for fixed system size $L = 511$ at various times t as indicated. The shape resembles a Gaussian (dashed line, for $t = 50$), but deviates clearly from it. (b) The activity rescaled by the particle density at the driving site as a function of the distance $x - x_0$ for different system sizes L and at fixed time $t = 10$. The difference in shape cannot be caused by the activity having reached the boundary (as it cannot possibly given t), nor by the probability $D_s(x_0; x_0, L)$ by which activity is triggered. Again, a Gaussian (dashed) is shown for comparison.

all active sites, which is the t th round of parallel updates. The zeroth sweep is the initial drive, and so at the first sweep $\langle n(\mathbf{x}, 1; \mathbf{x}_0, L) \rangle = D_s(\mathbf{x}_0; \mathbf{x}_0, L) \delta_{\mathbf{x}, \mathbf{x}_0}$, where $D_s(\mathbf{x}_0; \mathbf{x}_0, L)$ is the (expected) density of particles at the driven site. In order to derive time-resolved estimates, for each time t these records have to be summed over and divided by the total number of drivings. If $n_i(\mathbf{x}, t; \mathbf{x}_0, L)$ is the record of the activity after i driving attempts (macroscopic time), we use the estimator

$$G(\mathbf{x}, t; \mathbf{x}_0, L) = \frac{1}{M} \sum_{i=1}^M n_i(\mathbf{x}, t; \mathbf{x}_0, L) \quad (9)$$

from a sample of M (consecutively) attempted avalanches by driving the system at site \mathbf{x}_0 . To make the estimator well-defined for $t > T_i$, we define $n_i(\mathbf{x}, t; \mathbf{x}_0, L) = 0$ whenever t exceeds T_i , the duration of the i th avalanche ($T_i = 0$ if no avalanche has occurred).

The time-dependence makes the numerics more difficult to handle compared to the statistics in the quiescent state discussed above. Indeed, the response function $G(\mathbf{x}, t; \mathbf{x}_0, L)$ contains more information in its space and time-dependence than, say, $D_s(\mathbf{x}; \mathbf{x}_0, L)$ and even at fixed \mathbf{x}_0 the analysis is numerically and analytically more difficult due to the additional time-dependence. To facilitate further analysis, we will focus mostly on various integrals of the response function $G(\mathbf{x}, t; \mathbf{x}_0, L)$.

By the definition of the local dynamics (toppling), the trajectories of active particles are those of random walkers. On the other hand, $G(\mathbf{x}, t; \mathbf{x}_0, L)$ itself does *not* obey

the diffusion equation,³ first of all because active particles may become trapped for a certain microscopic time, only to be re-activated some time later. Were those resting times discounted, each individual active particle would perform a random walk from the time it enters the system by external drive to the time when it leaves the system through an open boundary. However, regardless of how resting-times are discounted, the density $G(\mathbf{x}, t; \mathbf{x}_0, L)$ is never that of pure diffusion, as there are fluctuations and correlations in the number of active particles at different times.

Fig. 5 shows time slices of the activity, which is, according to Fig. 5(a) almost a slowly broadening Gaussian. Below we discuss briefly in what sense a plain diffusion process is recovered, but from Fig. 5(a) it is clear that the spatial structure is not exactly but very close to a Gaussian, as demonstrated by the slight mismatch of the data (full line) and an approximated Gaussian with the same height and roughly the same width (dashed line). One may argue that the slight deviation is due to lattice effects or due to the parity conservation in the activity, as the parity of the coordinate x of sites active at a given time t is identical to that of $x_0 + t$. The slight difference is certainly not due to the avalanche having reached the boundaries, as times are chosen short enough.

The activity also shows a mild dependence on the sys-

³ This does not contradict the time-integrated activity, Eq. (10), to obey the Poisson equation $D \nabla^2 \hat{G}(\mathbf{x}, t; \mathbf{x}_0, L) = -(1/2) \delta(x, x_0)$ [20], Eq. (11).

tem size, as shown in Fig. 5(b), but seems to converge. One may think that this is due to the probability of activity being triggered at all, which is the occupation probability at the driving site, $D_s(x_0; x_0, L)$, because the (average) activity is reduced on the whole across *all* sites if the site driven is not occupied (and thus fails to topple). However, this is not the case, as the data in Fig. 5(b) has been rescaled accordingly. It is also not due to the avalanche having reached the boundary, as times are chosen short enough again. As the time in these figures is chosen to confine activity to the bulk, it seems most likely that the reduction of activity is caused by *all* sites in a smaller system having a smaller occupation probability (Fig. 1(a)), thus hindering spreading of activity somewhat. At the same time, however, stationarity is maintained, *i.e.* the hindrance in the activity spreading does not result in an accumulation of particles. That the time integral over all activity is nevertheless identical to that of a random walk regardless of the system size, does not mean that the activity in smaller systems, which is reduced at earlier times, must exceed that of bigger systems at later times or last longer, because the path density of random walkers increases with system size, as discussed below.

We will discuss the *temporal* features of the response function in further detail below. They show a very clear departure from a diffusion process, rendering the present behaviour superdiffusive.

The random walker nature of individual particles can be captured by summing over all times

$$\widehat{G}(\mathbf{x}; \mathbf{x}_0, L) = \sum_{t=1}^{\infty} G(\mathbf{x}, t; \mathbf{x}_0, L) \quad (10)$$

which is the average number of topplings caused at site \mathbf{x} by driving at site \mathbf{x}_0 . In directed sandpiles, this quantity can be used to solve the system exactly, as higher order responses can be written in terms of products of such two-point functions [33, 77]. In the stationary state, every particle added eventually leaves the system, following a random walker trajectory until it reaches the dissipative boundary. One may thus think of each particle added as producing a random walker trajectory from the source \mathbf{x}_0 to a point at the boundary (even when the activity trace is more akin to a branching process, following individual branches of the trajectories and allowing occasional rests, produces random walker paths).

To ease notation, we adopt mostly a continuum perspective in the following. Because each toppling results in *two* particles being moved, the total number of topplings at site \mathbf{x} (per avalanche) is thus half the density of Brownian paths (per particle), $\widehat{G}(\mathbf{x}; \mathbf{x}_0, L) = (1/2)\widehat{\phi}_0(\mathbf{x}; \mathbf{x}_0, L)$ where $\widehat{\phi}_0(\mathbf{x}; \mathbf{x}_0, L) = \int_0^{\infty} dt \phi_0(\mathbf{x}, t; \mathbf{x}_0, L)$ and $\phi_0(\mathbf{x}, t; \mathbf{x}_0, L)$ is the solution of the diffusion equation, $\partial_t \phi_0 = D\nabla^2 \phi_0$, with diffusion constant $D = 1/(2d)$ and initial condition $\lim_{t \rightarrow 0} \phi_0(\mathbf{x}, t) = \delta(\mathbf{x} - \mathbf{x}_0)$. On a lattice ∇^2 is the lattice Laplacian and $\delta(\mathbf{x} - \mathbf{x}_0)$ is to be replaced by $\delta_{\mathbf{x}, \mathbf{x}_0}$.

Carrying on in the continuum, it follows that $\widehat{G}(\mathbf{x}; \mathbf{x}_0, L)$ solves the Poisson equation

$$D\nabla^2 \widehat{G}(\mathbf{x}; \mathbf{x}_0, L) = -(1/2)\delta(\mathbf{x} - \mathbf{x}_0) \quad (11)$$

with $\mathbf{x}, \mathbf{x}_0 \in (0, L+1)$ and Dirichlet boundary conditions identical to those on the lattice, $\widehat{G}(0; \mathbf{x}_0, L) = \widehat{G}(L+1; \mathbf{x}_0, L) = 0$, which in one dimension produces

$$\widehat{G}(x; x_0, L) = \begin{cases} \frac{x(L+1-x_0)}{2D(L+1)} & \text{for } 0 \leq x < x_0 \\ \frac{x_0(L+1-x)}{2D(L+1)} & \text{for } x_0 \leq x \leq L+1 \end{cases} \quad (12a)$$

a solution that holds identically on the lattice.

We note in passing that at $t \rightarrow 0$ half the density of walker paths is $(1/2)\delta_{\mathbf{x}, \mathbf{x}_0}$ and thus clearly smaller than the response $G(\mathbf{x}, 0; \mathbf{x}_0, L) = D_s(\mathbf{x}_0; \mathbf{x}_0, L)\delta_{\mathbf{x}, \mathbf{x}_0}$ because $1/2 < D_s(\mathbf{x}_0; \mathbf{x}_0, L)$, which means in turn that the return probability of activity is (at some later times) less than half of that of a random walker, as otherwise the time integral of activity $G(\mathbf{x}, t; \mathbf{x}_0, L)$ cannot be exactly equal to half the integral over $\phi_0(\mathbf{x}, t; \mathbf{x}_0, L)$.

The Poisson equation Eq. (11) and, on the lattice, the corresponding difference equation

$$D\nabla^2 \widehat{G}(\mathbf{x}; \mathbf{x}_0, L) = -(1/2)\delta_{\mathbf{x}, \mathbf{x}_0} \quad (13)$$

with a lattice Laplacian on the left and a Kronecker- δ on the right equally apply in higher dimensions. It may be interpreted and derived as a continuity equation of particles being transported from one site to another, two at each toppling. In the continuum it is easily solved in higher dimensions by

$$\widehat{G}(\mathbf{x}; \mathbf{x}_0, L) = \frac{1}{2} \left(\frac{1}{L'} \right)^{d-1} \frac{2}{L+1} \sum_{n=1}^{\infty} \sum_{\mathbf{m}=(\infty, \dots, \infty)}^{(\infty, \dots, \infty)} \frac{\sin(q_n x) \sin(q_n x_0) \exp(i\mathbf{k}_{\mathbf{m}} \cdot (\mathbf{y} - \mathbf{y}_0))}{D(q_n^2 + \mathbf{k}_{\mathbf{m}}^2)} \quad (14)$$

where $\mathbf{y} \in [0, L']^{d-1}$ are the $d-1$ components of \mathbf{x} in the periodic directions and $x \in (0, L')$ is its component in the open direction, correspondingly for \mathbf{x}_0 . The $d-1$ dimensional vector $\mathbf{k}_{\mathbf{m}}$ has components $k_{m_i} = 2\pi m_i/L'$ with $m_i \in \mathbb{Z}$ for $i = 2, 3, \dots, d$, whereas $q_n = \pi n/(L+1)$ is a scalar with $0 < n \in \mathbb{N}^+$. The solution of Eq. (13) is correspondingly

$$\widehat{G}(\mathbf{x}; \mathbf{x}_0, L) = \frac{1}{2} \left(\frac{1}{L'} \right)^{d-1} \frac{2}{L+1} \sum_{n=1}^L \sum_{\mathbf{m}=(0, \dots, 0)}^{(L'-1, \dots, L'-1)} \frac{\sin(q_n x) \sin(q_n x_0) \exp(i\mathbf{k}_{\mathbf{m}} \cdot (\mathbf{y} - \mathbf{y}_0))}{2D((1 - \cos(q_n)) + \sum_{i=2}^d (1 - \cos(k_{m_i})))} \quad (15)$$

with $\mathbf{y} \in \{1, 2, \dots, L'\}^{d-1}$, $x \in \{1, 2, \dots, L\}$, $k_{m_i} = 2\pi m_i/L'$ with $m_i \in \{0, 1, \dots, L' - 1\}$ for $i = 2, \dots, d-1$, and $q_n = \pi n/(L+1)$ with $n \in \{1, 2, \dots, L\}$.

The continuum solution Eq. (14) still carries the signature of the lattice: there are L' sites in the periodic direction with site $y = 0$ being identical to site $y = L'$ but only L sites in the open direction, with activity on both sites $x = 0$ and $x = L+1 = L'$ vanishing. The only quantities with the dimension of a length on the right hand side of Eq. (14) are therefore L'^{-d} from the pre-factors and L'^2 from $\mathbf{k}_m^2 + q_n^2$ in the denominator. Anticipating the (simplified) scaling form Eq. (25) we therefore notice that Eq. (14) can be written as $ab^{-z}|\mathbf{x} - \mathbf{x}_0|^{-(d-2)}\tilde{\mathcal{F}}\left(\frac{\mathbf{x}-\mathbf{x}_0}{L'}\right)$ with dimensionless a , b and $\tilde{\mathcal{F}}$. In case of the time-integrated activity, $\hat{G}(\mathbf{x}; \mathbf{x}_0, L)$, which is a two-point response function, one can therefore identify L' as the correlation length analytically.

Integrating Eq. (14) over the periodic directions (sheets of constant x), as used later in Eq. (50), gives L'^{d-1} times the integrand at $\mathbf{k}_m = 0$,

$$\begin{aligned} \int_0^{L'} d^{d-1}y \hat{G}(\mathbf{x}; \mathbf{x}_0, L) &= L'^{d-1} \tilde{G}(x; \mathbf{x}_0, L) \\ &= \frac{1}{2} \frac{2}{L+1} \sum_{n=1}^{\infty} \frac{\sin(q_n x) \sin(q_n x_0)}{D q_n^2} \end{aligned} \quad (16)$$

and on the lattice

$$\begin{aligned} \sum_{\substack{y'_2, \dots, y'_d = (1, \dots, 1) \\ y'_1 = 1, \dots, L'}}^{(L', \dots, L')} \hat{G}(\mathbf{x}; \mathbf{x}_0, L) &= L'^{d-1} \tilde{G}(x; \mathbf{x}_0, L) \\ &= \frac{1}{2} \frac{2}{L+1} \sum_{n=1}^{\infty} \frac{\sin(q_n x) \sin(q_n x_0)}{2D(1 - \cos(q_n))} \end{aligned} \quad (17)$$

from Eq. (15), which recovers exactly Eq. (12) with $D = 1/(2d)$ dependent on the dimension. This is not surprising as integrating over sheets of constant x corresponds to considering hopping of particles only as far as their x -coordinate is concerned. Given the periodicity of $\hat{G}(\mathbf{x}; \mathbf{x}_0, L)$, the integral $L'^{d-1} \tilde{G}(x; \mathbf{x}_0, L)$ obeys $D \partial_x^2 L'^{d-1} \tilde{G}(x; \mathbf{x}_0, L) = -(1/2)\delta(x - x_0)$, the differential equation in one dimension with the reduced diffusion constant of $D = 1/(2d)$, as hops in only one of d directions results in a change of sheets.

Fig. 6 confirms the triangular shape of the time-integrated activity Eq. (12). As discussed above, the origin of the profile is somewhat trivial, but it has two important implications: Firstly, the activity is *shaped* by the boundaries. As opposed to the nearly featureless density profile of the inactive particles, Fig. 1, the activity is very strongly affected by the presence of the boundary, as all activity ceases there. Every particle added is eventually transported to the boundary [56]. Secondly, because time integrals of the response are *exactly* random walker profiles, the \mathbf{k} -dependence of a (suitable) propagator in a field theory will not renormalise. A non-trivial

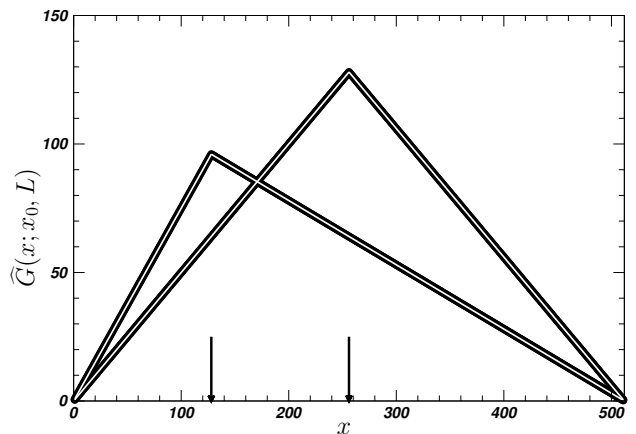


FIG. 6: The time integrated activity $\hat{G}(\mathbf{x}; \mathbf{x}_0, L)$ according to Eq. (10) is in fact half the number of times a random walker starting at x_0 passes through a particular site x before leaving at the boundary. The activity (the response $G(x, t; x_0, L)$ to driving at x_0) has a complicated dependence on time, because of its frequent stops and restarts, but once that is integrated out, the resulting densities are those of random walkers. The exact solution, Eq. (12), shown as a white line, is virtually indistinguishable from the numerical results ($L = 511$ driven at $x_0 = 256$ or $x_0 = 128$ as indicated by the arrows).

dynamical exponent z , which is often obtained through the renormalisation of the diffusion constant, will have to be obtained through the renormalisation of the time-dependence. At frequency $\omega = 0$, the full propagator in a field theory reads exactly $1/(D\mathbf{k}^2)$, whereas the frequency-dependence may deviate from the tree-level $-\dot{\omega}$ in almost arbitrary form, provided only that it vanishes at $\omega = 0$. Anticipating some of the discussion below, we note that the propagator being $1/(D\mathbf{k}^2)$ implies $\eta = 0$.

1. Spatially integrated activity

Instead of integrating the response function over time, to reduce the number of independent variables, one may just as well integrate in space. The simplest version of this quantity is the spatial integral of the activity

$$R(t; \mathbf{x}_0, L) = \sum_{\mathbf{x}} G(\mathbf{x}, t; \mathbf{x}_0, L), \quad (18)$$

i.e. the total (spatially integrated) activity at time t , which in a numerical implementation corresponds to the height of the stack of active sites with each entry being weighted by $\lfloor z_{\mathbf{x}}(t)/2 \rfloor$, the activity at that site. The spatial activity integral is closely related to the order parameter of many absorbing state phase transitions [9], the spatially averaged activity density $\rho_a = R(t; \mathbf{x}_0, L)/L^d$. In fact $R(t; \mathbf{x}_0, L)$ is the area under the activity “slices” shown in Fig. 5. Numerical results, shown in Fig. 7(a), clearly differ across system sizes on the large time scale. Even on the very short time scale ($t = 1, \dots, 10$, not

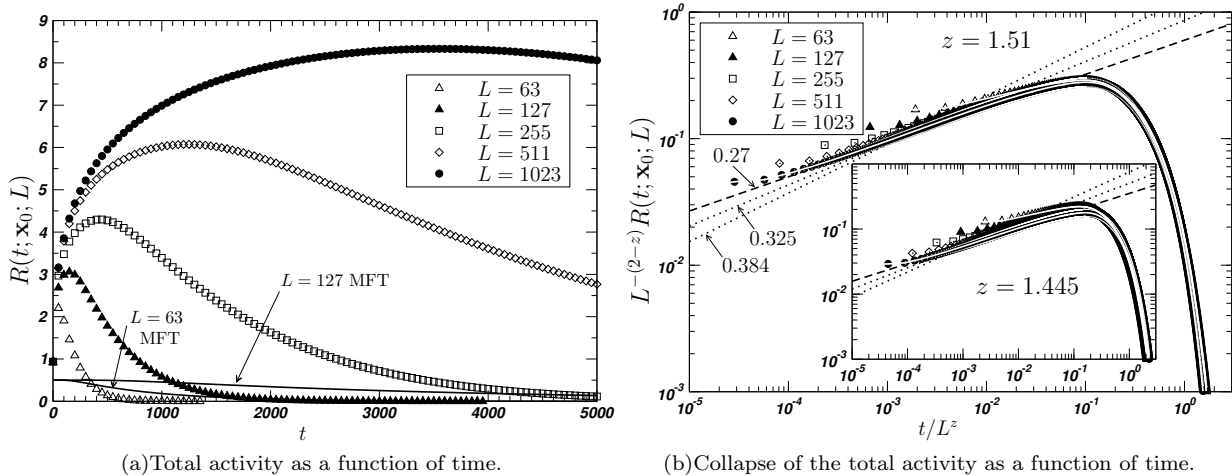


FIG. 7: The total (spatially integrated) activity $R(t; \mathbf{x}_0, L)$ as a function of time t for various system sizes L in one dimension, driven at $x_0 = (L + 1)/2$. (a) Activity as a function of absolute (microscopic) time (symbols, pruned) and comparison to the (badly matching) mean field theory Eq. (19) (full lines). Error bars (not shown) are much smaller than symbols. (b) Collapse of $R(t; \mathbf{x}_0, L)$ for a range of systems sizes L (as indicated) according to Eq. (23). The dashed line in the main panel shows a powerlaw with exponent 0.27, the apparent behaviour of $R(t; \mathbf{x}_0, L)$ in small t . The dotted lines show the expected behaviour $(2 - z)/z = 0.384(10)$ with $z = 1.445(10)$ from literature [18] and $(2 - z)/z = 0.325$ from $z = 1.51$ used in the collapse. The white lines on top of the symbols show the data for $L = 63$ and $L = 1023$ to allow for an easier assessment of the quality of the collapse. The inset shows the same plot for the literature value $z = 1.445$.

shown separately) $R(t; \mathbf{x}_0, L)$ appears to differ systematically for all system sizes considered (although displaying some convergence). If this is solely due to the slightly decreased occupation density by inactive particles, $D_s(\mathbf{x}; \mathbf{x}_0, L)$, then the effect is cumulative and highly non-linear, as $R(t = 0; \mathbf{x}_0, L)$ barely varies between different system sizes. For large t the activity eventually reaches the boundary of the system. As is clear from the collapse in Fig. 7(b) and further discussed below, the position of the maximum total activity, $R(t_{\max}; \mathbf{x}_0, L)$, scales with the dynamical exponent, $t_{\max} \propto L^z$.

Employing again a continuum approximation (where we identify $L = L'$ to ease notation), in an MFT, the spatially integrated activity $R(t; \mathbf{x}_0, L)$ is given by the propagation of the activity profile of a single active particle, which undergoes a Poissonian branching or extinction with equal rates, subject to Dirichlet boundary conditions. In one dimension the resulting profile is the spatial integral of the density $(1/2) \frac{2}{L+1} \sum_{n=1}^L \sin(x_0 q_n) \sin(x q_n) \exp(-D q_n^2 t)$, see Eqs. (16) and (17), with momenta $q_n = n\pi/(L + 1)$ [63], as discussed above, which gives⁴

$$R_{\text{MFT}}(t; \mathbf{x}_0, L) = \frac{2}{\pi} \sum_{n=1, \text{odd}}^L \frac{\sin(x_0 q_n)}{n} e^{-D q_n^2 t}. \quad (19)$$

Fig. 7(a) shows this profile as well. The mean field the-

ory differs very clearly from the one-dimensional Manna Model in a number of points: Firstly, the tail of the mean field activity drags out for very long times, even for moderately large systems, not least as to make up for Eq. (24) below, the “sum rule” relating the mean avalanche size and the time integral over the (total) activity. In comparison, avalanches in the Manna Model are “short and sharp”. Secondly, by construction, the activity in the mean field theory never exceeds $1/2$, whereas the maximum activity in the Manna Model seems to increase with system size, clearly exceeding unity even for the smallest system sizes studied. This is particularly clear at $t = 0$ where the simple mean field assumes an activity of $1/2$, whereas in the Manna Model activity is triggered with the occupation probability at the driven site.

The scaling of $R(t; \mathbf{x}_0, L)$ can be determined by making the usual (Ornstein-Zernike-like) scaling ansatz of the response [2, 78],

$$G(\mathbf{x}, t; \mathbf{x}_0, L) = a |\mathbf{x} - \mathbf{x}_0|^{-(d-2+\eta+z)} \times \mathcal{F}\left(\frac{\mathbf{x} - \mathbf{x}_0}{L}, \frac{\mathbf{x} - \mathbf{x}_0}{bt^{1/z}}\right), \quad (20)$$

where we assume, for simplicity, translational invariance, even when our systems are not translationally invariant in the x -direction. Eq. (20) may be regarded of the definition of the anomalous dimension η and the dynamical exponent z . The dimensionless scaling function $\mathcal{F}(u, v)$ turns off correlations beyond the system size and confines them to a region of linear extent proportional to $t^{1/z}$ at the short time scale. Dimensional consistency is restored by metric factors a and b . Taking the limit

⁴ The integral $\int_0^{L+1} dx \sin(q_n x) = 2/q_n$ for odd n needs to be replaced by $\sum_{x=1}^L \sin(q_n x) = \sin(q_n)/(1 - \cos(q_n))$ on the lattice.

$L \rightarrow \infty$ in Eq. (20), the spatial integral of G gives $R(t; \mathbf{x}_0, L) \propto t^{(2-\eta-z)/z}$. We expect this scaling behaviour to hold for $t \ll L^z$; in fact, re-writing Eq. (20) as

$$G(\mathbf{x}, t; \mathbf{x}_0, L) = a|\mathbf{x} - \mathbf{x}_0|^{-(d-2+\eta+z)} \times \tilde{\mathcal{F}}\left(\frac{t}{b'L^z}, \frac{\mathbf{x} - \mathbf{x}_0}{bt^{1/z}}\right) \quad (21)$$

and integrating over \mathbf{x} at finite L gives

$$R(t; \mathbf{x}_0, L) = a\left(\frac{t}{b}\right)^{(2-\eta-z)/z} \tilde{\mathcal{F}}_0\left(\frac{t}{b'L^z}\right) \quad (22)$$

even for finite L , or alternatively

$$R(t; \mathbf{x}_0, L) = \tilde{a}L^{2-\eta-z} \tilde{\mathcal{F}}'_0\left(\frac{t}{bL^z}\right) \quad (23)$$

with suitable metric factors and scaling function, as used in Fig. 7(b).

It turns out that η in fact vanishes, as suggested in the discussion after Eq. (16). Firstly, this is implied by the sum rule arising from the temporal integral over $R(t; \mathbf{x}_0, L)$, which is the average avalanche size,

$$\langle s \rangle(\mathbf{x}_0, L) = \sum_{t=0}^{\infty} R(t; \mathbf{x}_0, L) \simeq \int_0^{\infty} dt R(t; \mathbf{x}_0, L) \quad (24)$$

written as an integral for convenience. In the present case of centre driving, the average avalanche size scales in L like $\langle s \rangle \propto L^2$ and $\eta = 0$ follows from using the scaling form Eq. (23) in the integrand of Eq. (24).

A more subtle demonstration that $\eta = 0$ follows from the time integral of the activity, which reduces the activity to random walker trajectories. Taking the time integral of Eq. (20) gives

$$\hat{G}(\mathbf{x}; \mathbf{x}_0, L) = ab^{-z}|\mathbf{x} - \mathbf{x}_0|^{-(d-2+\eta)} \hat{\mathcal{F}}\left(\frac{\mathbf{x} - \mathbf{x}_0}{L}\right) \quad (25)$$

with a new, suitably defined scaling function $\hat{\mathcal{F}}$. This observable, \hat{G} , is the average number of topplings at site \mathbf{x} per particle added at site \mathbf{x}_0 , as discussed at the beginning of Sec. III C, see Eq. (10). An Ornstein-Zernike correlation function [78], as the one generated by the density of Brownian paths has $\eta = 0$ and must coincide with Eq. (25), so $\eta = 0$ follows. Alternatively, one may consult \hat{G} in Eq. (12) and Eq. (14), which indeed behave like $x^{2-d}\hat{\mathcal{F}}(x/L)$ for fixed x_0 .

Taking $\eta = 0$ henceforth, Fig. 7(b) shows a good collapse on the basis of Eq. (23) with $z = 1.51$, in poor agreement with the literature value of $z = 1.445(10)$ based on the scaling of avalanche durations [18]. The collapse based on $z = 1.445$ is shown in the inset of Fig. 7(b). White lines for the data of $L = 63$ and $L = 1023$ have been added on top of the symbols to assess the quality of the collapse, which, away from the tail, is clearly worse for $z = 1.445$ than for $z = 1.51$.

Apart from the collapse in L , according to Eq. (22), there is also scaling in t at large enough but early times. Clearly, for fixed t the total activity $R(t; \mathbf{x}_0, L)$ converges in large L , as for sufficiently large L the activity no longer reaches the boundaries, which therefore become irrelevant. Apart from small (but possibly cumulative) effects due to the density of inactive particles, for fixed t a regime exists where $R(t; \mathbf{x}_0, L) \propto t^{(2-z)/z}$ independent of (large) L , so that $\tilde{\mathcal{F}}_0$ in Eq. (22), which carries all L -dependence, is constant, or equivalently, that $\tilde{\mathcal{F}}'_0$ in Eq. (23) behaves like a power law itself, $\tilde{\mathcal{F}}'_0(u) \propto u^{(2-z)/z}$. Therefore in Eq. (22) $t^{(2-z)/z}$ shapes $R(t; \mathbf{x}_0, L)$ on the short time scale, and the scaling function $\tilde{\mathcal{F}}_0$ on the long time scale.

The initial power law regime is clearly visible in Fig. 7(b), which suggests $(2-z)/z \approx 0.27$ and thus $z \approx 1.574\dots$, again quite off the expected value of $(2-z)/z = 0.384(10)$ from $z = 1.445(10)$ [18], also shown in the plot. A third slope shown in Fig. 7(b), $(2-z)/z \approx 0.325$ is determined by z giving the best collapse, $z \approx 1.51$. However, measuring exponents by fitting a section of the data against a straight line in a double logarithmic plot ignores the rôle of the scaling function and is generally prone to errors [79–81]. The significance of the slopes shown in Fig. 7(b) is therefore that both slopes of 0.27 and 0.325 (corresponding to $z = 1.574$ and $z = 1.51$ respectively) seem to be consistent with the data, whereas the literature value of $z = 1.445(10)$ fails, producing a slope of 0.384, which is clearly off.

2. Temporal shape of the avalanche

The Manna Model differs from the MFT above in that particles and thus activity display some complicated “resting”, but otherwise trajectories are random walks. Time integrals over the activity therefore remove any non-trivial behaviour, whereas space integrals retain it. It is thus worthwhile to look for ways of extracting universal features from $R(t; \mathbf{x}_0, L)$ or similar quantities.

Because $R(t; \mathbf{x}_0, L)$ is bound to scale in order to accommodate the average avalanche size, no convergence of $R(t; \mathbf{x}_0, L)$ can be expected in large L at large $t \propto L^z$. To observe convergence for all t , the profile has to be rescaled by the duration of the avalanche and the mean activity. Theory has access (at least at MFT level) to an approximation of the spatial integral of the activity conditional to a certain time of termination, T , the duration of the avalanche, but it is difficult to condition in addition to a certain avalanche size. Numerically, on the other hand, this would be trivial: If $R_i(t; \mathbf{x}_0, L) = \sum_{\mathbf{x}} n_i(\mathbf{x}, t; \mathbf{x}_0, L)$ is an individual measurement of the space-integrated activity at time t of an avalanche that has size s_i and duration T_i , then $R_i(t; \mathbf{x}_0, L)/(s_i/T_i)$ would be the relevant quantity to consider. Instead we note that

$$s_i = \sum_{t=0}^{T_i-1} R_i(t; \mathbf{x}_0, L) \quad (26)$$

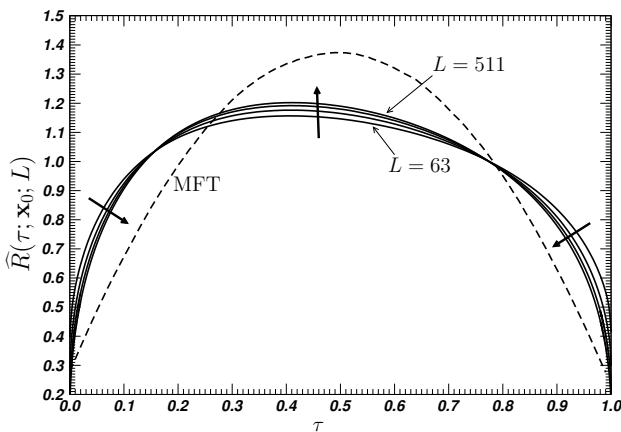


FIG. 8: The rescaled activity $\hat{R}(\tau; \mathbf{x}_0, L)$ (“temporal shape of the avalanche”), Eq. (27), in one-dimensional systems of size $L = 63, 127, 255, 511$ driven at the centre, $x_0 = (L+1)/2$. The rescaling (see main text) maps the times of each (spatially integrated) activity time series to the interval $\tau \in [0, 1]$ and the data is normalised so that the integral under the curve is unity. The numerical data are shown as full lines, as the error bars are exceedingly small. The thick arrows point in the direction of increasing system size. The data seems to suggest that there is slow convergence to a shape one might suspect to be universal. It is noticeably lopsided compared to the mean-field theory (MFT) shown as a dashed line. The mean-field theory is based on a branching random walk on a (finite) lattice ($L = 255$). Numerical data for larger systems are computationally prohibitively expensive, see Sec. II B.

is the avalanche size if T_i is the duration and averaging over the rescaled measurements $R_i(\tau T_i; \mathbf{x}_0, L)$,

$$\bar{f}(\tau) = \frac{1}{M} \sum_{i=1}^M R_i(\lfloor \tau T_i \rfloor; \mathbf{x}_0, L)$$

gives $\int_0^1 d\tau \bar{f}(\tau) = \frac{1}{M} \sum_{i=1}^M s_i/T_i$, so that normalising by (the estimate of) $\langle s/T \rangle$ produces

$$\hat{R}(\tau; \mathbf{x}_0, L) = \frac{1}{\langle s/T \rangle} \frac{1}{M} \sum_{i=1}^M R_i(\lfloor \tau T_i \rfloor; \mathbf{x}_0, L), \quad (27)$$

a quantity that has a unit-integral and may therefore be expected to converge. Closely related to this is a quantity sometimes referred to as the “temporal shape of the avalanche” [82, 83], first studied by Kuntz and Sethna [84] (see also [85]), and closely connected to the $(1/f)$ power spectrum [86]. To make $\langle s/T \rangle$ in Eq. (27) well-defined in case of $T_i = 0$ (and thus $s_i = 0$), one may consider the above derivation with T_i replaced by $T_i + \epsilon > T_i$ and take the limit $\epsilon \rightarrow 0$.

Fig. 8 shows $\hat{R}(\tau; \mathbf{x}_0, L)$ for different system sizes L , demonstrating the expected convergence. Notably, the graph displays a slight, unexpected asymmetry that is absent in the mean-field theory of a branching process.

Because the time averaged total activity $\langle s/T \rangle$ diverges (slowly) for $L \rightarrow \infty$ and $R_i(t; \mathbf{x}_0, L)$ at $t = 0$ is exactly the finite occupation density at \mathbf{x}_0 and expected

to be small at $t = T_i$, in the thermodynamic limit, $\hat{R}(\tau; \mathbf{x}_0, L)$ is expected to vanish at $\tau = 0$ and $\tau = 1$ (and one may speculate that the MFT gives asymptotically $\hat{R}(\tau) = 6\tau(1 - \tau)$). In a suitable theory, one may redefine time and observables such that $R_i(t; \mathbf{x}_0, L)$ is exactly unity at these points.

3. Width of the response

In the following we want to characterise further the deviation of the activity density from plain diffusion. In Fig. 5 we have demonstrated that the spatial distribution of activity $G(x, t; x_0, L)$ at (x, t) in response to driving at x_0 at $t = 0$ is very close to Gaussian. We may proceed by determining the kurtosis *etc*, but as mentioned above, it is difficult to attribute any deviation correctly, because there are several sources for corrections: finiteness of the lattice, boundaries, discretisation in space, discretisation in time and separation into even and odd sublattices. Only the time integral of the activity can be mapped exactly to a random walk, which is *approximated* by a Gaussian in the continuum. It turns out that the *temporal evolution* of the spatial distribution of activity is strongly superdiffusive. To see this more clearly, we may calculate the spatial variance of the *normalised* $G(\mathbf{x}, t; \mathbf{x}_0, L)$, using the spatial integral $R(t; \mathbf{x}_0, L)$, Eq. (18). The width of the response $G(x, t; x_0, L)$ may be defined as

$$\Delta^2(t; \mathbf{x}_0, L) = R^{-1}(t; \mathbf{x}_0, L) \sum_{\mathbf{x}} (\mathbf{x} - \mathbf{x}_0)^2 G(x, t; x_0, L). \quad (28)$$

In the present definition, $\Delta^2(t; \mathbf{x}_0, L)$ looks very much like a mean squared displacement, except that many particles contribute to $G(x, t; x_0, L)$ simultaneously and only very few have actually been displaced starting from \mathbf{x}_0 , the origin. In fact, many may have been moved *towards* \mathbf{x}_0 and most may have moved only a couple of sites.

Fig. 9(a) shows a very clear power law dependence of $\Delta^2(t; \mathbf{x}_0, L)$ on (small) time t , scaling faster than linear in t for intermediate times (below a cutoff set by the system size), thus rendering the process superdiffusive. To relate this to the results above, we integrate $|\mathbf{x} - \mathbf{x}_0|^2 G$ using Eq. (21) over \mathbf{x} , which gives

$$\Delta^2(t; \mathbf{x}_0, L) = \left(\frac{t}{b}\right)^{2/z} \frac{\tilde{\mathcal{F}}_2\left(\frac{t}{bL^z}\right)}{\tilde{\mathcal{F}}_0\left(\frac{t}{bL^z}\right)}, \quad (29)$$

using Eq. (22), regardless of $\eta = 0$.

If $\Delta^2(t; \mathbf{x}_0, L) \propto t^{2/z}$ (expected for $t \ll L^z$ but not guaranteed as the scaling function may contribute, Eq. (29)), Fig. 9(a) suggests $2/z \approx 1.28$ and thus $z \approx 1.5625$ rather than $z = 1.445(10)$ of [18]. This is confirmed by a collapse, Fig. 9(b). The value of $z \approx 1.5625$ from the t -dependence of $\Delta^2(t; \mathbf{x}_0, L)$ is reasonably consistent with the value of $z \approx 1.574$ from the t -dependence of $R(t; \mathbf{x}_0, L) \propto t^{(2-z)/z}$ in Fig. 7(b) ($(2 - 1.574)/1.574 \approx 0.27$). The literature value of

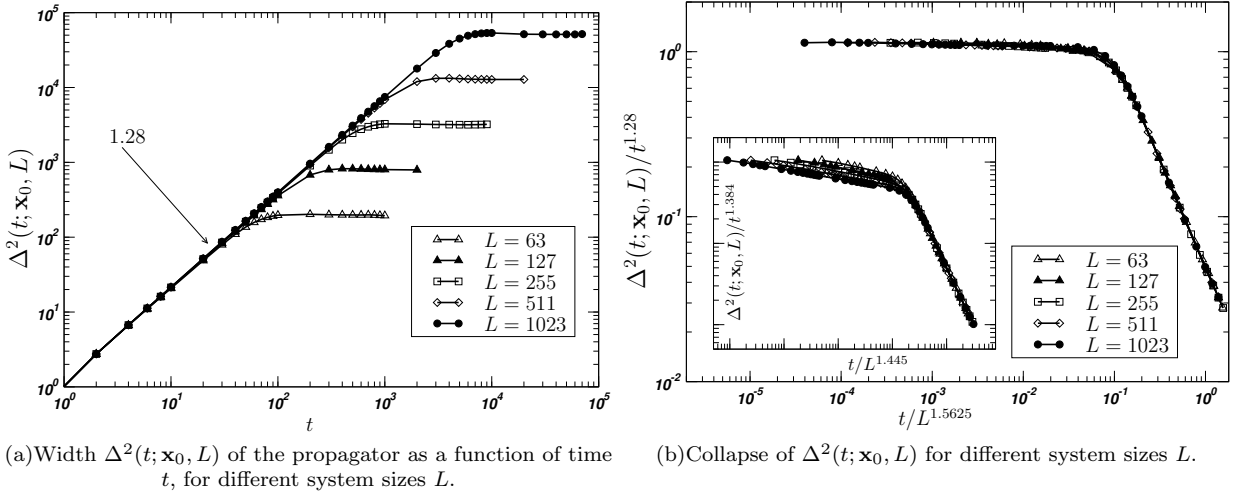


FIG. 9: Width $\Delta^2(t; \mathbf{x}_0, L)$ of the response propagator $G(x, t; x_0, L)$, as defined in Eq. (28), in one dimension for centre drive, $x_0 = (L + 1)/2$, and for different system sizes L . (a) The apparent scaling in time t suggests $2/z \approx 1.28$ and thus a dynamical exponent $z = 1.5625$ very different from $z = 1.445(10)$ determined from the moments of the avalanche duration [18]. The scaling is confirmed by the collapse shown in (b). The inset of that figure shows the same collapse with the latter literature value of $z = 1.445(10)$.

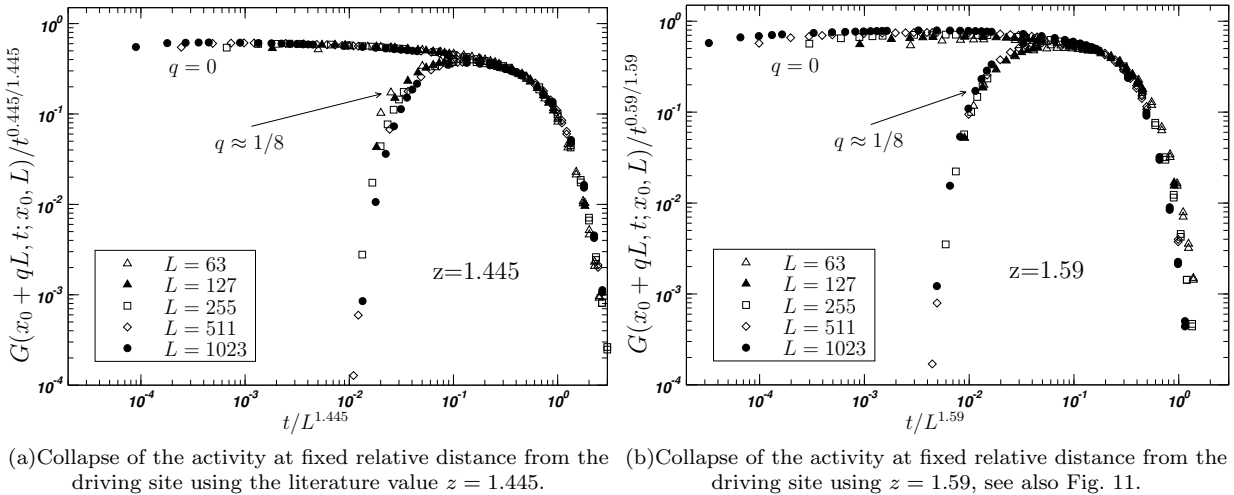


FIG. 10: The activity $G(x_0 + qL, t; x_0, L)$ in one dimension for fixed $q = 0$ and $q \approx 1/8$ collapsed by plotting $G(x_0 + qL, t; x_0, L)t^{(z-1)/z}$ against t/L^z , using two different exponents, (a) $z = 1.445$ (literature [18]) and (b) $z = 1.59$ (larger than any estimate above, but see Fig. 11).

$z = 1.445(10)$ produces a rather dissatisfying collapse shown in the inset of Fig. 9(b), that improves in the tail (large t) only because Δ^2 converges to L^2 and so $\Delta^2/t^{2/z'}$ plotted versus $(L^2/t^{2/z'})^{-z'/2} = t/L^{z'}$ produces a straight line in a double logarithmic plot with slope $-z'/2$ for any z' . We will discuss the range of results for z further in Sec. V.

4. Further spatial scaling of the response

A *quantitative* test for scaling is to extract “moments” by integrating out all but one independent variable. This

procedure leads to the measurements normally taken in SOC [87], such as moments of the avalanche size (for example, the temporal integral of $R(t; \mathbf{x}_0, L)$ gives $\langle s \rangle$). The usual caveats apply, in particular finite size corrections, which we have largely ignored in the present analysis. A *qualitative* test of scaling is to attempt a collapse of the data, such as the one for $R(t; \mathbf{x}_0, L)$ in Fig. 7(b). However, for $G(\mathbf{x}, t; \mathbf{x}_0, L)$ this is difficult to attain in the form (20) as there are at least *three* independent parameters, $|\mathbf{x} - \mathbf{x}_0|$ (assuming translational invariance), t and L , listed in order of increasing sparseness. In principle such a collapse can be done in three-dimensional plots, but the small range of L compared to the high density of

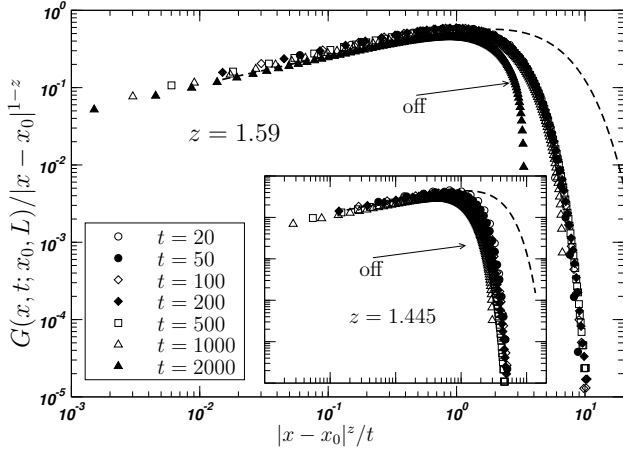


FIG. 11: Attempt of a collapse of the activity (response) $G(\mathbf{x}, t; \mathbf{x}_0, L)$ with $L = 511$, according to Eq. (20) using $z = 1.59$ (see Fig. 10(b)) in the main panel and $z = 1.445$ in the inset. The data were selected so that *apparently* $L^z \gg t$, except for $t = 2000$ marked by “off”. The dashed lines shows the Gaussian of Fig. 5(b).

points in $|\mathbf{x} - \mathbf{x}_0|$ and the still fairly large range and number of measurements in t , makes it difficult to assess the quality of such a collapse, which becomes nearly useless when projected into two dimensions.

To investigate further the spatial dependence of the activity $G(x, t; x_0, L)$, we consider fixed $(x - x_0)/L = q$, so that according to Eq. (20) with $\eta = 0$,

$$G(x_0 + qL, t; x_0, L) = a|qL|^{-(d-2+z)} \mathcal{F}\left(|q|, \frac{t}{b|qL|^z}\right), \quad (30)$$

which for fixed q ought to collapse when plotting $G(x_0 + qL, t; x_0, L)L^{d-2+z}$ against t/L^z (for the earliest to the latest times t). Fig. 10 shows a collapse for $x = x_0$ ($q = 0$) as well as $x = (L + 1)/8$ ($q \approx 1/8$) with centre driving, $x_0 = (L + 1)/2$. While the literature value of $z = 1.445$ works fairly well, Fig. 10(a), the collapse is relatively insensitive against different choices of the dynamical exponent ($z = 1.59$ is shown in Fig. 10(b), exceeding even $z = 1.574$ above, see Fig. 7(b), but identical to the z used in Fig. 11).

Assuming instead $L^z \gg t$ produces a collapse of G on the basis of Eq. (20) when plotting $G(\mathbf{x}, t; \mathbf{x}_0, L)|\mathbf{x} - \mathbf{x}_0|^{-(d-2+z)}$ against $|\mathbf{x} - \mathbf{x}_0|^z/t$ for different t and L , Fig. 11. The main panel shows a fairly neat collapse in the tail, while the inset shows a somewhat broader tail which, however, seems to cover a wider range of data, incorporating even the data marked by “off”. Picking, however, the data as to exclude those that do not produce a collapse, presumably on the basis that $L^z \gg t$ is violated, is a form of biased selection.

In summary, the scaling of the response $G(\mathbf{x}, t; \mathbf{x}_0, L)$ is exactly as expected in a critical finite system: on the short time scale the characteristic length is set by the time $t^{1/z}$, Eqs. (20) and (22) (demonstrated in Fig. 7(b)),

and on the long time scale by the system size L in the form L^z , as discussed in Sec. III C 1 (Eq. (22) and discussion towards the end). Indeed, with the time-dependence integrated out, activity has all characteristics of a random walk (Fig. 6), so that all the non-trivial features are to be found in the time-dependence. While collapses such as Fig. 7(b) and Fig. 9 confirm the presence of scaling, the exponent z we found in one dimension varied: In Fig. 7(b) $z \approx 1.51$ from the collapse but $z \approx 1.574$ from the scaling in t of $R(t; \mathbf{x}_0, L)$, in Fig. 9(a) $z \approx 1.5625$ from the collapse and the scaling in t of the width $\Delta^2(t; \mathbf{x}_0, L)$ and in Fig. 10 no clear outcome ($z = 1.445$ but also $z = 1.59$) for the scaling of the activity $G(x, t; x_0, L)$. On the other hand, the dynamical exponent determined in the literature from the scaling of the cutoff of the avalanche duration is $z = 1.445(10)$ [18]. We will discuss this discrepancy further in Sec. V.

5. Activity-activity correlations

There are very little spatial correlations in the density of the inactive particles (Fig. 2). This is very different for the activity. The correlation function to be considered next is, strictly speaking, a three-point function, as it measures the correlations of activity at different sites \mathbf{x}_1 and \mathbf{x}_2 in a system driven at \mathbf{x}_0 . Although we have also considered data where all three sites are distinct, generally statistics is better for $\mathbf{x}_0 = \mathbf{x}_1$ (or $\mathbf{x}_0 = \mathbf{x}_2$, which amounts to the same), so we have focused on that case.

This correlation function is also a function of two times relative to the time of driving. We decided to consider only equal time correlations, with the aim to extract interesting *spatial* behaviour. The estimators for the unconnected activity-activity correlation function

$$C_u(\mathbf{x}_2, \mathbf{x}_1, t; \mathbf{x}_0, L) = \frac{1}{M} \sum_{i=1}^M n_i(\mathbf{x}_2, t; \mathbf{x}_0, L) n_i(\mathbf{x}_1, t; \mathbf{x}_0, L) \quad (31)$$

and the connected correlation function

$$C_c(\mathbf{x}_2, \mathbf{x}_1, t; \mathbf{x}_0, L) = \frac{1}{M} \sum_{i=1}^M n_i(\mathbf{x}_2, t; \mathbf{x}_0, L) n_i(\mathbf{x}_1, t; \mathbf{x}_0, L) - \frac{1}{M} \sum_{i=1}^M n_i(\mathbf{x}_2, t; \mathbf{x}_0, L) \frac{1}{M} \sum_{i=1}^M n_i(\mathbf{x}_1, t; \mathbf{x}_0, L) \quad (32)$$

are based on the same measurements of local activity as Eq. (9). Choosing $\mathbf{x}_1 = \mathbf{x}_0$ still leaves us with four independent variables. To capture the temporal evolution, we chose to take samples only at $t = 1, 2, 3, \dots, 9, 10, 20, \dots, 90, 100, 200, \dots, 9000$ for a range of different system sizes, all driven at the centre. However, as mentioned in Sec. II A, activity vanishes on sites whose distance to the driven site \mathbf{x}_0 has a parity different from that of t , and in particular $n_i(\mathbf{x}_0, t; \mathbf{x}_0, L) = 0$ strictly

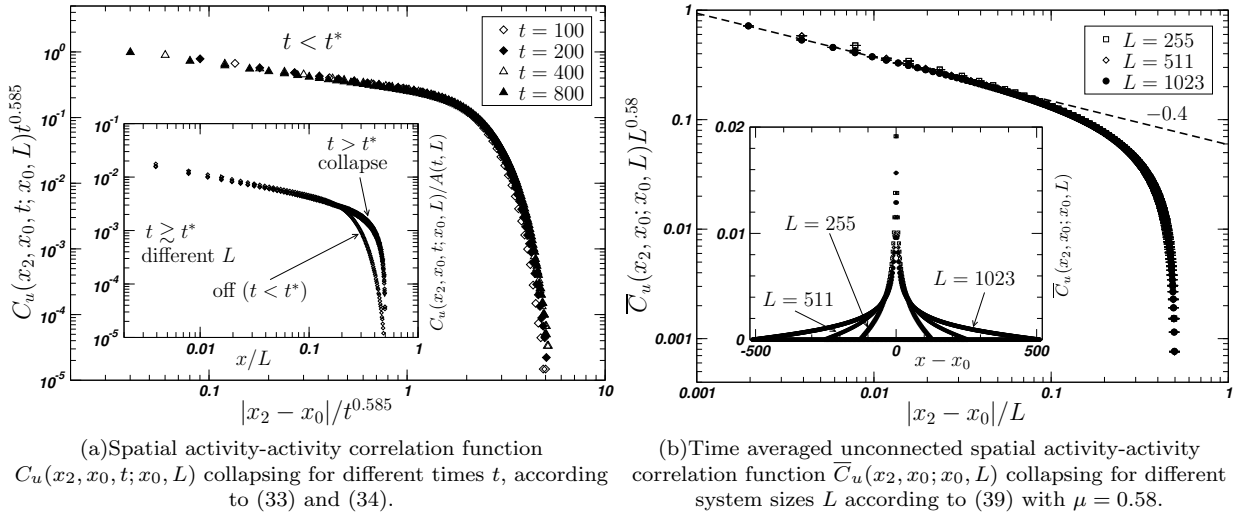


FIG. 12: Spatial correlations of the activity. (a) Activity-activity correlation function $C_u(x_2, x_0, t; x_0, L)$, Eq. (31), at different (equal) times and for various system sizes L and with centre drive, $x_0 = (L+1)/2$. The main panel shows a collapse for $L = 511$ by rescaling both axes by a suitable power of the time t , here $\lambda = 0.585$. The collapse Eq. (33), however, works only up until some saturation time t^* from when on $C_u(x_2, x_0, t; x_0, L)$ displays essentially the same shape with a time-dependent pre-factor, Eq. (34). This is shown in the inset, where data for different times and system sizes ($t = 3000, 5000, 7000$ for $L = 511$ as well as $t = 2000$ for $L = 255$ and $t = 500$ for $L = 127$) is made to collapse by plotting $C_u(x_2, x_0, t; x_0, L)$ divided by a suitable amplitude $A(t, L)$ against x/L . That amplitude drops roughly exponentially in time (shown are $A(t, 511) = 0.59^{(t-1000)/2000}$, but also $A(2000, 255) = 0.513$ and $A(500, 127) = 1.35$); it is, for fixed system size L , to large part given by the fraction of avalanches that last until t . The set marked “off” shows data for $L = 511$ and $t = 1000$, before the saturation. (b) Collapse Eq. (39) of the time-averaged spatial correlation function $\bar{C}_u(x_2, x_0; x_0, L)$, Eq. (37), on a double logarithmic scale using $\mu = 0.58$. That the distance has to be rescaled by the system size, is a reminder of the latter coinciding with the correlation length. The straight, dashed line shows a power law with exponent -0.4 . Inset: Correlation function on a linear scale. Because of the parallel update, $n_i(x_2, t; x_0, L)n_i(x_1, t; x_0, L)$ vanishes for all t if x_1 and x_2 are on sublattices of different parity resulting in vanishing $\bar{C}_u(x_2, x_0; x_0, L)$, thus not shown in the logarithmic main panel.

for all \mathbf{x}_0 at odd t , so that both $C_u(\mathbf{x}_2, \mathbf{x}_0, t; \mathbf{x}_0, L)$ and $C_c(\mathbf{x}_2, \mathbf{x}_0, t; \mathbf{x}_0, L)$ vanish at odd t . From the data shown in Fig. 12(a), it is clear that the unconnected correlation function $C_u(\mathbf{x}_2, \mathbf{x}_1, t; \mathbf{x}_0, L)$ collapses in one dimension for different, early $t \ll t^*(L)$ according to

$$C_u(x_2, x_0, t; \mathbf{x}_0, L) = A_0 t^{-\lambda} \mathcal{C} \left(\frac{t}{b|x_2 - x_0|^{1/\lambda}} \right) \quad (33)$$

with some amplitude A_0 , exponent λ (here $\lambda = 0.585$ similar to the exponent μ in Eq. (39) below, whereas $1/z = 0.692(5)$ [18]) and scaling function \mathcal{C} , but “saturates” for $t \gg t^*(L)$ like (inset of Fig. 12(a))

$$C_u(x_2, x_0, t; \mathbf{x}_0, L) = A(t, L) \mathcal{C}'(|x_2 - x_0|/L) \quad (34)$$

where $A(t, L)$ is no longer a power-law in t (as effectively in (33)), but is instead dominated by an exponential in t . For fixed L , that amplitude is essentially the fraction of “survivors”, *i.e.* the probability of an avalanche lasting at least until t . Data for $t \gtrsim t^*(L)$ is shown in the inset of Fig. 12(a), together with data of the correlation function not quite at saturation (labelled “off” as opposed to “collapse”). The evolution of the activity-activity correlation function is therefore compatible with the classic narrative of correlations spreading throughout

the system as the avalanche unfolds [34–36], until the effective correlation length (the cutoff length t^λ in Eq. (33)) reaches the boundaries, suggesting $\lambda = 1/z$ (see below). For essentially all the time thereafter and thus most of the time, the correlation function has the form (34), although numerical data for very long times becomes very noisy.

We are unable to offer an explanation for the scaling form Eq. (33), because of the many different variables and scales involved. It depends on at least two different points in space and on a time that needs to be small enough so that Eq. (33) applies, determining $t^*(L)$ implicitly. The most striking feature of the scaling form is that the exponent in the pre-factor $t^{-\lambda}$ is identical to the exponent in the argument of the scaling function, which we expect to be $1/\lambda = z$. However, $1/\lambda \approx 1.71$ (based on $\lambda = 0.585$ in Fig. 12(a)) is greater than any z measured above. Below we will derive the scaling of the time-averaged correlation function \bar{C}_u , but it is difficult to relate it to the scaling of (33), as the latter requires $t \ll t^*(L)$.

Repeating the analysis for the connected correlation function C_c , Eq. (32), shows rather poor collapses. It remains somewhat unclear why that happens. The second term in (32) has a fairly small contribution, yet big

enough to spoil most collapses. A collapse like Fig. 12(a) for C_c is rather noisy and dissatisfying, producing no reasonable estimate of λ according to Eq. (33).

If the activity correlations can be regarded as “almost stationary” (or quasi-stationary as in fixed energy sandpiles [9, 35, 88]), it is justified to take their time average. If T_i is the duration of the i th avalanche, then

$$\bar{G}(\mathbf{x}; \mathbf{x}_0, L) = \frac{1}{\sum_{i=1}^M T_i} \sum_{i=1}^M \sum_{t=1}^{T_i} n_i(\mathbf{x}, t; \mathbf{x}_0, L) \quad (35)$$

estimates the time-averaged activity at site \mathbf{x} conditional to activity (somewhere) [89], as otherwise time stops passing. Because $\langle \sum_{i=1}^M T_i \rangle = M \langle T \rangle$, the time-average $\bar{G}(\mathbf{x}; \mathbf{x}_0, L) \langle T \rangle$ is the average number of topplings of site \mathbf{x} per avalanche, *i.e.*

$$\bar{G}(\mathbf{x}; \mathbf{x}_0, L) \langle T \rangle = \hat{G}(\mathbf{x}; \mathbf{x}_0, L) \quad (36)$$

see Eqs. (9) and (10). Correspondingly, the unconnected time-averaged correlation function may be written as

$$\begin{aligned} \bar{C}_u(\mathbf{x}_2, \mathbf{x}_1; \mathbf{x}_0, L) \\ = \frac{1}{\sum_{i=1}^M T_i} \sum_{i=1}^M \sum_{t=1}^{T_i} n_i(\mathbf{x}_2, t; \mathbf{x}_0, L) n_i(\mathbf{x}_1, t; \mathbf{x}_0, L) \end{aligned} \quad (37)$$

and the connected one as

$$\begin{aligned} \bar{C}_c(\mathbf{x}_2, \mathbf{x}_1; \mathbf{x}_0, L) \\ = \frac{1}{\sum_{i=1}^M T_i} \sum_{i=1}^M \sum_{t=1}^{T_i} n_i(\mathbf{x}_2, t; \mathbf{x}_0, L) n_i(\mathbf{x}_1, t; \mathbf{x}_0, L) \\ - \bar{G}(\mathbf{x}_2; \mathbf{x}_0, L) \bar{G}(\mathbf{x}_1; \mathbf{x}_0, L). \end{aligned} \quad (38)$$

The unconnected time-averaged correlation function for $x_1 = x_0$ (in one dimension) is shown in Fig. 12(b) and displays a remarkably good collapse

$$\bar{C}_u(x_2, x_0; x_0, L) = L^{-\mu} \mathcal{G}\left(\frac{|x_2 - x_0|}{L}\right) \quad (39)$$

for different system sizes with $\mu \approx 0.58$ (for an earlier estimate of $\mu = 0.658$ based on uniform driving see [17]). The denominator in the argument of the scaling function $\mathcal{G}(|x_2 - x_0|/L)$ should be regarded as the correlation length, which is in fact proportional to the system size, exactly as expected for a finite system at the critical point [3, 4, 6, 9, 14]. The exponent μ that scales the amplitude in Eq. (39) can be related via a sum-rule to known scaling exponents, such as the scaling of the activity variance $\Delta\rho_a/L^d$ [9, 17] (see Eq. (2.36) in [9], $\Delta\rho_a L^{-d}$ is the variance of the density ρ_a and $\Delta\rho_a$ is the spatial integral of the variance),

$$\frac{\Delta\rho_a}{L^d} = \frac{1}{L^{2d}} \int d^d x_1 d^d x_2 \bar{C}_u(\mathbf{x}_2, \mathbf{x}_1; \mathbf{x}_0, L) \propto L^{\gamma'/\nu_\perp - d} \quad (40)$$

where we have used the notation of [9], except that we use d for the spatial dimension (denoted by D in [9]). If the scaling of $\bar{C}_u(\mathbf{x}_2, \mathbf{x}_1; \mathbf{x}_0, L)$ is essentially translationally invariant, as suggested in Eq. (39), then $\Delta\rho_a L^{-d} \propto L^{-\mu}$ from Eq. (40) and thus $\mu = d - \gamma'/\nu_\perp = 2\beta/\nu_\perp$. The estimate $\mu \approx 0.58$ above (Fig. 12(b)) is perfectly in line with literature values of $1 - \gamma'/\nu_\perp = 0.59(4)$ in one dimension [9].

Alternatively, one may relate \bar{C}_u to the second moment of the avalanche size. Given that the instantaneous avalanche size is Eq. (26), the estimator for the second moment $\langle s^2 \rangle = M^{-1} \sum_{i=1}^M s_i^2$ is *exactly* equivalent to

$$\langle s^2 \rangle = \frac{1}{M} \sum_{i=1}^M \sum_{t_1, t_2=1}^{T_i} \sum_{\mathbf{x}_1, \mathbf{x}_2} n_i(\mathbf{x}_2, t_2; \mathbf{x}_0, L) n_i(\mathbf{x}_1, t_1; \mathbf{x}_0, L) \quad (41)$$

resulting in a corresponding sum rule on the unconnected correlation function. It requires, however, the *two (three) point, two time* correlation function. Assuming that it follows essentially Eq. (39) with x_1/x_2 and t_1/t_2 as additional arguments in the scaling function, gives

$$\langle s^2 \rangle \propto \langle T \rangle L^{2d+z} L^{-\mu} \quad (42)$$

where $\langle T \rangle$ undoes the normalisation in Eq. (37) compared to Eq. (41), L^{2d} is due to the double space integral (or sum, Eq. (41)), L^z is due to the additional time integral in Eq. (41) compared to Eq. (37) and, finally, $L^{-\mu}$ is due to Eq. (39). Given that $\langle s^2 \rangle \propto L^{D(3-\tau)}$, $\langle T \rangle \propto L^{z(2-\alpha)}$ and $D(1-\tau) = z(1-\alpha)$ (all exponents explained in detail in [4]), one arrives at $\mu = 2(d+z-D)$ which is in line with $\mu = d - \gamma'/\nu_\perp = 2\beta/\nu_\perp$ because what is denoted D here is $D_f + z$ in [9] and so $d+z-D$ here is in fact β/ν_\perp there. However, $\mu = 2(d+z-D)$ gives $\mu = 0.38(5)$ using the values of $z = 1.445(10)$ and $D = 2.253(14)$ of [18]. The mismatch with $\mu = 0.59(4)$ mentioned above cannot be explained by the dynamical exponent of $z = 1.393(37)$ measured in [9], which gives an even smaller value of $2(d+z-D)$. Rather, it is the poor match of $D_f + z = d - \beta/\nu_\perp$ in [9], which gives $D = 2.11(4)$ based on measurements in the fixed energy sandpile (FES) version of the Manna Model, and $D = 2.253(14)$ of [18] taken in the SOC mode.

The slope of $\mathcal{G}(q)$, Eq. (39), that is so clearly visible in Fig. 12(b) (dashed line) may be captured by fitting against a power law with a cutoff, so that $\mathcal{G}(q) \propto q^{-0.4}$ for small z . For sufficiently small $x_2 - x_0$ and sufficiently large L , the correlation function $\bar{C}_u(x_2, x_0; x_0, L)$ thus behaves like $L^{-\mu+0.4} |x_2 - x_0|^{-0.4}$. It is difficult to see how to relate this behaviour to known exponents through scaling relations.

The connected time-averaged correlation function $\bar{C}_c(\mathbf{x}_2, \mathbf{x}_1; \mathbf{x}_0, L)$ collapses as well, but is much less sensitive to a change of the exponent μ in Eq. (39). While it is compatible to $\mu = 0.58$, with some small deviations, its tail ($|\mathbf{x}_2 - \mathbf{x}_1|/L$ close to unity) still collapses even for $\mu = 0.3$. That the tail collapses so easily is of course unsurprising, as $\bar{C}_c(\mathbf{x}_2, \mathbf{x}_1; \mathbf{x}_0, L)$ vanishes as sites become

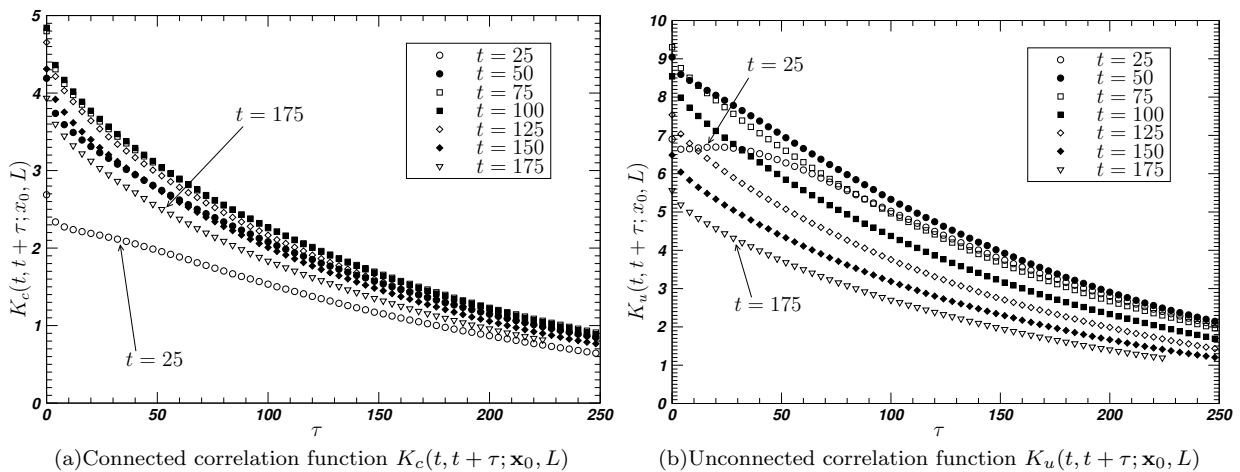


FIG. 13: The two-time correlation functions $K_{c,u}(t, t + \tau; \mathbf{x}_0, L)$, Eqs. (44) and (45), for a range of times $t = 25, 50, \dots, 175$ against the time lag τ (pruned) for centre driving of a one-dimensional system of size $L = 63$. (a) For $t \geq 50$ and $t \leq 150$ the connected correlation functions are very similar. About 52% of avalanches have a duration of $T \geq 50$. (b) For $t \geq 50$ the shape of correlation functions differ very little, while their amplitude clearly does.

uncorrelated, *i.e.* when $|\mathbf{x}_2 - \mathbf{x}_1|$ approaches L , and a sharp drop is very insensitive to rescaling.

6. Two-time activity correlations and $1/f$ -noise

Historically, SOC was introduced as an “explanation for $1/f$ noise” [3], even when that notion quickly took a less prominent place [4, 6]. The initial measurement [3] of the power-law characteristics of the power spectrum of the BTW Model was soon revised by Jensen *et al* [7], who had to make a number of drastic assumptions in order to link the power spectrum to the avalanche duration distribution. A more recent, detailed numerical analysis by Laurson *et al* [86] found non-trivial $1/f^\alpha$ noise in both the BTW and the Manna Model.

In the following, we analyse the correlations in the spatially integrated activity signal

$$\hat{n}_i(t; \mathbf{x}_0, L) = \sum_{\mathbf{x}} n_i(\mathbf{x}, t; \mathbf{x}_0, L) \quad (43)$$

of avalanche i with duration T_i , which, of course, varies among avalanches. That makes the calculation of correlations somewhat ambiguous,⁵ in particular when taking averages over ensembles. We intend to carry out the following analysis in the spirit of the original link of SOC and $1/f$ spectra. To arrive at a single time series, we effectively concatenate consecutive $\hat{n}_i(t; \mathbf{x}_0, L)$ by inserting an infinite trail of zeros.

⁵ Apart from allowing for vanishing n_i (see below), one may, for example, rescale time to the unit interval or weight avalanches of different durations differently.

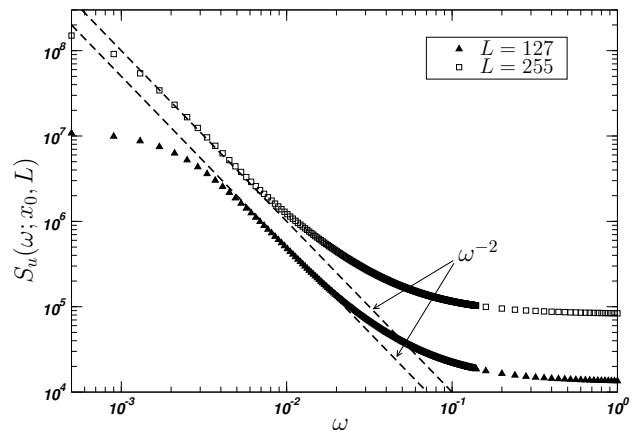


FIG. 14: Double logarithmic plot of the (pruned) power spectrum $S_u(\omega; x_0, L)$, Eq. (47), of the unconnected correlation function K_u , Eq. (44), in a the centre-driven one-dimensional Manna Model of size L as indicated. There is a possibly increasing (with L) intermediate regime that displays some power law scaling $\propto \omega^{-2}$ (dashed line).

We will make use of the estimators (*cf.* Eqs. (31) and (32))

$$K_u(t_2, t_1; \mathbf{x}_0, L) = \frac{1}{M} \sum_{i=1}^M \hat{n}_i(t_2; \mathbf{x}_0, L) \hat{n}_i(t_1; \mathbf{x}_0, L), \quad (44)$$

and

$$K_c(t_2, t_1; \mathbf{x}_0, L) = K_u(t_2, t_1; \mathbf{x}_0, L) - R(t_2; \mathbf{x}_0, L)R(t_1; \mathbf{x}_0, L), \quad (45)$$

where the second term makes use of $R(t; \mathbf{x}_0, L)$, which is the expectation of $\hat{n}_i(t; \mathbf{x}_0, L)$, Eqs. (9) and (18). To make $\hat{n}_i(t; \mathbf{x}_0, L)$ well-defined for all t , we take

$\hat{n}_i(t; \mathbf{x}_0, L) = 0$ for $t > T_i$. This together with Eq. (44) that never mixes different avalanches, amounts to analysing correlations in concatenated activity histories as if each was succeeded by an infinite trail of zeros, thereby implementing separation of time scales. Other choices have been made in the literature, notably by Laurson *et al* who suggest the effect of trailing zeros is negligible [86].

As the process is not time-homogeneous, $K_{c,u}(t_2, t_1; \mathbf{x}_0, L)$ are functions of two times t_1 and t_2 . In the past, this feature was to large extent ignored. In [7] the authors assume that \hat{n}_i is a top-hat function with duration T_i and height s_i/T_i , approximating K_u by a suitably weighted integral of convolutions of that top-hat.

From Fig. 7 it is clear that in the Manna Model, \hat{n}_i is not overly well approximated by a top-hat. In the following, we want to explore the shape of the unconnected and connected correlation functions K_u and K_c . The first question that arises is whether it is justified to assume that K_u and K_c are essentially functions of the time lag $|t_2 - t_1|$, but otherwise independent of t_1 . Fig. 13(a) shows that this is indeed the case for a range of t_1 at least as far as the connected correlation function is concerned. This feature is clearly less pronounced for the unconnected correlation function, Fig. 13(b), which, however, is closer to the one studied in the past with regard to its $1/f$ characteristics in the BTW Model [7, 86].

Carrying on along the lines of Jensen *et al* [7] but also Laurson *et al* [86], the unconnected two-time correlation function is time-integrated (not time-averaged, as usual, *e.g.* [90]) over t ,

$$\overline{K}_u(\tau; \mathbf{x}_0, L) = \sum_{t=0}^{\infty} K_u(t, \tau; \mathbf{x}_0, L) \quad (46)$$

and Fourier-transformed,

$$S_u(\omega; \mathbf{x}_0, L) = 2 \sum_{\tau=0}^{\infty} \cos(\omega\tau) \overline{K}_u(\tau; \mathbf{x}_0, L) \quad (47)$$

which resembles a sigmoidal shape, as shown in Fig. 14, quite different to what Laurson *et al* [86] obtain using a different concatenation scheme. The intermediate drop may be approximated by a power law, ω^{-2} , consistent with similar findings in the BTW Model [7], but it is difficult to trace that behaviour back to the decay of temporal correlations.

In fact, there is little non-trivial, asymptotic long-time behaviour in K_u or K_c at all. What displays scaling in these quantities is their cutoff (because of the scaling of durations), but not the correlation functions themselves, Fig. 13(a). The approach by Laurson *et al* [86] has clearly been more successful in that respect.

One might be tempted to repeat the above analysis for the connected correlation function K_c as defined in Eq. (45). However, taking an average like Eq. (46) over the unconnected part $R(t_2; \mathbf{x}_0, L)R(t_1; \mathbf{x}_0, L)$ remains ambiguous. It is arguably to be replaced by the

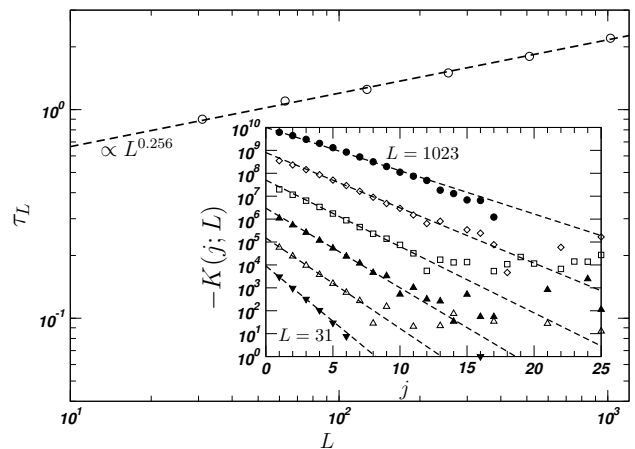


FIG. 15: Scaling of the macroscopic avalanche-avalanche correlation time τ_L with the system size L . The power law fitted (dashed line), $\tau_L \propto L^{0.256}$, is compatible with the prediction $\tau_L \propto L^{D-2}$ with $D = 2.253(14)$ [18]. In one dimension, correlation times are rather short, well under 10 for the system sizes considered. Inset: The negative of the actual correlation function $K(j; L)$ for $L = 31, 63, \dots, 1023$ with the exponential fits, $A_L \exp(-j/\tau_L)$ shown as dashed lines.

square of the average activity $\langle s \rangle / \langle T \rangle$, in which case, however, the time averaged \overline{K}_c no longer drops to 0 for $t \rightarrow \infty$ as normally expected for a connected correlation function. Given that our main interest in the present correlation functions was to make contact with the historic research focus, namely $1/f$ -noise as studied in [7], we did not pursue this approach any further.

7. Macroscopic time correlations

We finally consider the correlations in the size s_i of consecutive avalanches, $\langle s_i s_{i+j} \rangle - \langle s \rangle^2$ as a function of j , estimated via [91]

$$K(j; L) = \frac{1}{M-j} \sum_{i=1}^{M-j} s_i s_{i+j} - \frac{1}{M-j} \sum_{i=1}^{M-j} s_i \frac{1}{M-j} \sum_{i=1}^{M-j} s_{i+j}. \quad (48)$$

In the Oslo Model [64] the avalanche size can be interpreted as the displacement of an interface pulled on one end over a rough surface [4, 12, 13] and the macroscopic correlation time is, in this model, therefore related to the interface's roughness, which scales like L^χ with $\chi = D-d$. In the present case, neither the mapping exists nor can the driving be interpreted easily as a pulling force. Following nevertheless the same argument as in [12], the typical total number of topplings needed to avoid an overlap between initial and final interface configuration scales like $L^{\chi+d}$. The number of avalanches to be triggered to reach essentially independence is therefore of order $L^{\chi+d} / \langle s \rangle$,

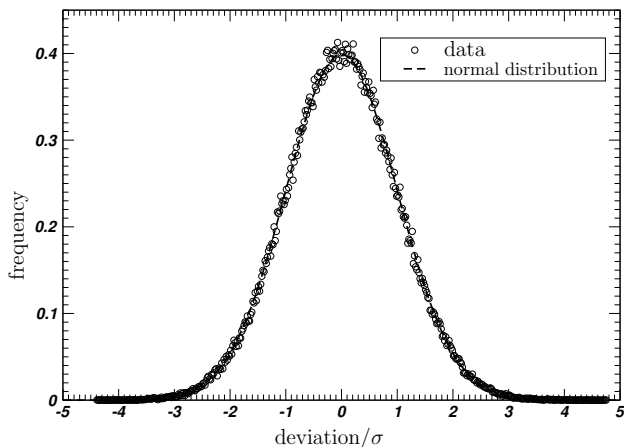


FIG. 16: A histogram of the deviation of the local density $D_s(\mathbf{x}; \mathbf{x}_0, L)$ from the average $\overline{D_s}(x; \mathbf{x}_0, L)$ in a sheet of constant x , in units of standard deviations of the density within a sheet, for a three dimensional system of size $63 \times 64 \times 64$. Within numerical error, the data follows a normal distribution shown as a dashed line.

which in the present case scales like L^{X+d-2} as $\langle s \rangle \propto L^2$, Eq. (1) with $x_0 = (L+1)/2$. In other words, the macroscopic correlation time should scale like $D-2 = 0.253(14)$ [18].

It is difficult to extract good estimates of the macroscopic correlation time from the data. As observed in directed models [92], correlations for $j > 0$ are anti-correlations, $K(j; L) < 0$, as large avalanches are normally followed by smaller ones and vice versa. Fig. 15 shows $-K(j; L)$ in a semi-logarithmic plot in the inset, suggesting an exponential decay of correlations, which are quite short-lived in one dimension (and obviously orders of magnitude shorter than the transient). Fitting them (by eye), $K(j; L) = A_L \exp(-j/\tau_L)$ with amplitude A_L , and plotting the resulting estimates for the correlation times τ_L yields a scaling of approximately $\tau_L \propto L^{0.256}$, as shown in Fig. 15, compatible with $D-2$ quoted above.

IV. HIGHER DIMENSIONS

We have repeated many of the measurements discussed above in three and five dimensions. Because the upper critical dimension of the Manna Model is $d_c = 4$ [9, 43, 44], $d = 3$ is expected to be much closer to mean-field results (and in that sense better behaved), whereas $d = 5$ is expected to reproduce them at least as far as universal quantities are concerned.

As the most interesting observables to consider in higher dimensions, we have selected the density of inactive particles in the quiescent state (*cf.* Sec. III A), the spatially integrated activity (*cf.* Sec. III C 1), the temporal shape of the avalanche (*cf.* Sec. III C 2), the width of the response (*cf.* Sec. III C 3), the spatial activity-

activity correlation function (*cf.* Sec. III C 5), and the macroscopic time avalanche-avalanche correlations (*cf.* Sec. III C 7).

Numerically, dimensions greater than one pose the disadvantage of high memory requirements for comparatively “small” system sizes as far as linear extent is concerned. In particular in five dimensions, lattices of linear extent beyond $L = 63$ are difficult to realise. The largest lattice we used in five dimensions therefore was $L = 95$. We have avoided scanning lattices as much as possible (see discussion before Eq. (3)), so that CPU-time requirements are mostly determined by the average avalanche size $\propto L^2$. The largest lattice in three dimensions was $L = 511$. As discussed above, periodic boundary conditions were applied in all but one (open) direction.

The periodic boundary conditions may suggest that observables do not depend on the coordinates y_2, \dots, y_d orthogonal to the open direction (parameterised by x). We will indeed consider in the following certain observables with respect to their sheet-average (spatial average at constant x) and their deviation from it. Yet, given centre driving at one single site $x_0 = (L+1)/2$, $y_{2,\dots,d} = 0$, translational invariance is broken in every direction.⁶ This is expected to be reflected in the observables, for example the response function: Periodic boundary conditions or not, activity that begins in a point will not spread instantaneously across entire sheets of constant x (which are of size L^{d-1}).

A. Three dimensions

It turns out, however, that even with (non-translational invariant) centre driving the density of inactive particles displays translational invariance within sheets of constant x . It is rather futile to attempt to visualise that by plotting the density profile for constant y_2, y_3 (coordinates within a sheet). Fig. 16 shows instead a histogram of the number of standard deviations by which the (estimated) density at each and every point within the sheets deviates from the average within a sheet,

$$\overline{D_s}(x; \mathbf{x}_0, L) = \sum_{y_2, y_3} D_s(\mathbf{x}; \mathbf{x}_0, L), \quad (49)$$

where $\mathbf{x} = (x, y_2, y_3)$. The result is a distribution very close to a normal distribution (also shown), suggesting that the small deviations of local densities from the sheet average $\overline{D_s}(x; \mathbf{x}_0, L)$ are possibly random and independent rather than systematic. However, confirming that by direct measurements of correlations is difficult, firstly because of the statistical noise (as seen in

⁶ If one is not interested in the particular symmetries of the system, this can be cured by driving (randomly) across entire sheets of constant x .

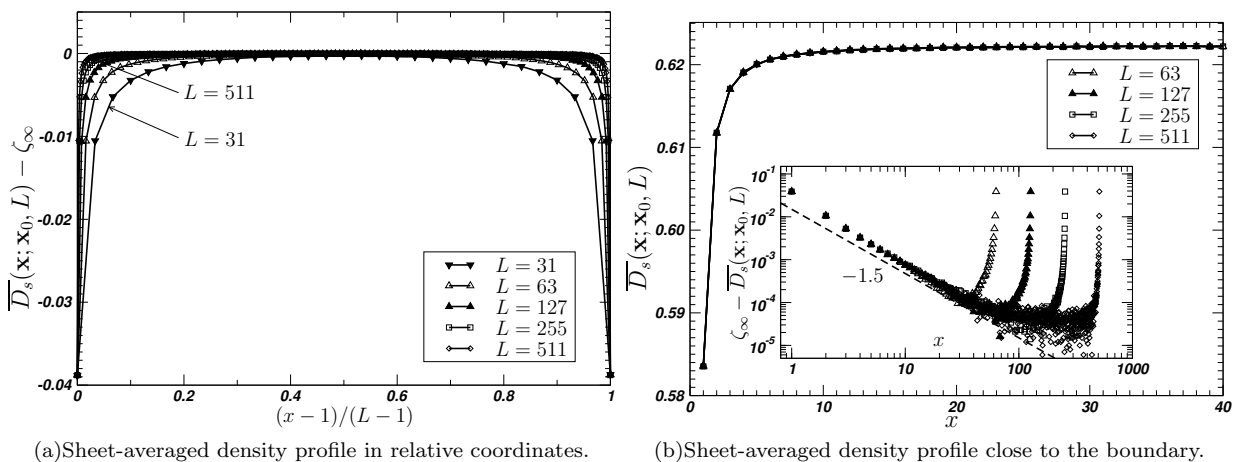


FIG. 17: The sheet-averaged density of inactive particles in three dimensions, $\overline{D}_s(x; \mathbf{x}_0, L)$, as deviation from the bulk value ($\zeta_\infty = 0.622325$ [19]) in the quiescence state at stationarity in three dimensions, *cf.* Fig. 1. Lines to guide the eye. (a) Plotting $\overline{D}_s(x; \mathbf{x}_0, L) - \zeta_\infty$ versus the relative position $(x-1)/(L-1)$ shows that the deviation of the density from the bulk value decays quickly away from the boundaries, producing an increasingly sharp shoulder with increasing system size. (b) Close to the boundary, on an absolute scale x (distance from the boundary), the density profile shows very quick convergence with increasing L . There is no noticeable difference between different L . However, as shown in the inset, the deviation from the bulk density ζ_∞ shows a (noisy) power law decay away from the boundary, roughly with exponent -1.5 (dashed line) and with a cutoff linear in L .

Fig. 2(b)) and secondly because of the wide range of correlations to consider. For example the two point function $C_s(\mathbf{x}_2, \mathbf{x}_1; \mathbf{x}_0, L)$, Eq. (6), depends on the positions relative to the open ends, x_1 and x_2 , as well as the $d-1$ displacements in the periodic direction, $\mathbf{y}_1 - \mathbf{y}_2$. Again, integrated observables, such as the window-averaged density Eq. (7), might be better suited to reveal (anti-) correlations.

Given the (observed) translational invariance in the periodic directions, Fig. 17 shows the sheet-averaged density profile $\overline{D}_s(x; \mathbf{x}_0, L)$ across the open direction in three-dimensional systems as the deviation from the bulk value $\zeta_\infty = 0.622325$ [19]. This data shows little qualitative difference compared to Fig. 1, except that the density remains much closer to the bulk value throughout, even close to the boundaries and even for comparatively small systems. The range of the ordinate of Fig. 17(a) is about an order of magnitude smaller than in one dimension. Fig. 17(b) shows that the profile close to the boundary displays no discernible difference among the system sizes considered; there is certainly no finite size scaling of the amplitude of the profile. However, similar to one dimension, Fig. 1, boundary effects decay like a power law. We estimate the exponent to be around -1.5 (as shown in the inset of Fig. 17(b)), but a reliable estimate is hampered by the high level of noise in the data and does not improve much when the data is binned. For comparison (see discussion in Sec. III A) $1/\nu_\perp = 1.7(4)$ [9], compatible with the exponent estimated here.

Integrating the local activity over the entire lattice produces the total activity, $R(t; \mathbf{x}_0, L)$, as defined in Eq. (18). As discussed in Sec. III C 1, we expect plotting $L^{2-z}R(t; \mathbf{x}_0, L)$ against t/L^z to produce a collapse.

In $d = 3$ dimensions this is indeed the case and works very well using $2 - z = 0.223$, based on the dynamical exponent $z = 1.777(4)$ as obtained in [19]; Fig. 18 shows a corresponding collapse like the one obtained in Fig. 7(b) in $d = 1$ dimensions.

Also shown in this figure is the slope of the rescaled total activity in rescaled time, which we expected to display an exponent of $(2 - z)/z$ (see the discussion in Sec. III C 1). While this was not fully confirmed in one dimension, it is perfectly in line with the findings in three dimensions.

Normalising the activity profile in the form introduced in Eq. (27) produces the “temporal shape of the avalanche” shown in Fig. 19 together with the mean field theory introduced in Sec. III C 1 and Sec. III C 2. The curves are remarkably close given that the mean field theory should apply only in dimensions of $d \geq d_c = 4$. The data still shows a slight skew which is difficult to see by naked eye. The mean field data displays a similar slant (possibly a finite size effect), but in the opposite direction. The collapse thus improves when plotting $\widehat{R}(1 - \tau; \mathbf{x}_0, L)$ against the MFT.

The width of the response propagator, $\Delta^2(t; \mathbf{x}_0, L)$, as defined in Eq. (28) produces a collapse if rescaled suitably, as shown for $d = 1$ in Fig. 9(a). In Sec. III C 3 it was demonstrated that in one dimension the collapse requires a dynamical exponent, $z \approx 1.5625$, that deviates quite clearly from the expected value of $z = 1.445(10)$ from the literature. In Fig. 20 we show that the data in three dimensions is compatible with the expected value, $z = 1.777(4)$ [19], apparently validating the scaling arguments in Sec. III C 3. The possible causes of the mismatch in one dimension is discussed further in Sec. V.

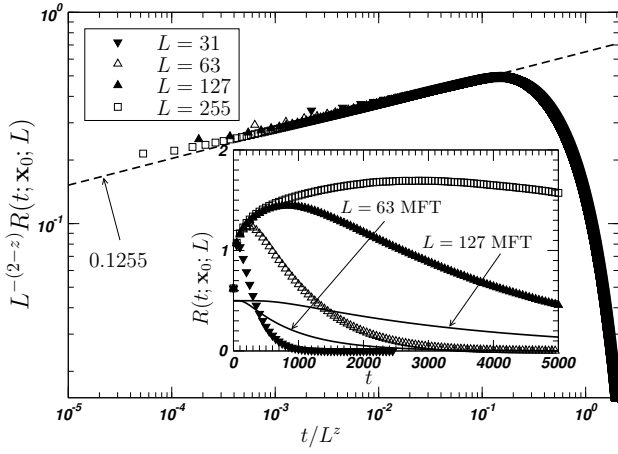


FIG. 18: Collapse of the spatially integrated activity, $R(t; \mathbf{x}_0, L)$, Eq. (18), for the centre driven Manna Model in $d = 3$ dimensions (see Fig. 7(a) for the result in one dimension), plotting $R(t; \mathbf{x}_0, L)L^{-(2-z)}$ against t/L^z using the literature value of $z = 1.777(4)$ [19]. The dashed line shows the expected slope $(2 - z)/z = 0.1255(25)$, in line with the discussion in Sec. III C 1. The inset shows the (pruned) data on a linear scale together with the MFT as in Fig. 7(a).

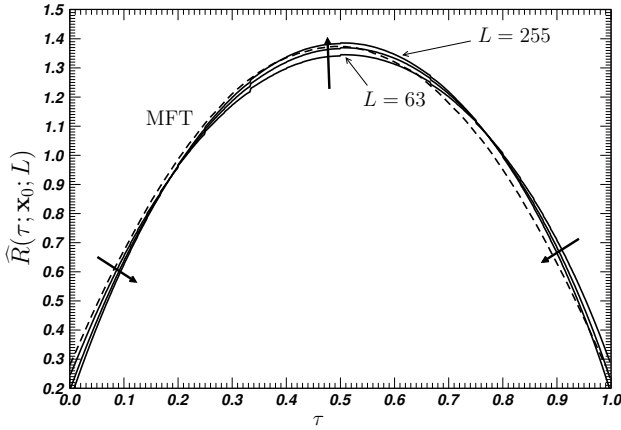


FIG. 19: The rescaled activity $\widehat{R}(\tau; \mathbf{x}_0, L)$ in three-dimensional systems of size $L = 63, 127, 255$ driven at the centre, $x_0 = (L + 1)/2$, to be compared to Fig. 8. The thick arrows point in the direction of increasing system size. The rescaling maps the spatially integrated activity to the interval $\tau \in [0, 1]$. Normalisation is applied so that the integral under the curve is unity. The data is remarkably close to that of the mean-field theory, shown as a dashed line, ($L = 255$, see Fig. 8).

As mentioned above, the propagation of activity (the response function) is certainly not expected to be translationally invariant, as activity surely is correlated to the position of the initial driving. However, it is numerically very challenging to analyse spatial data as a function of all d components. We have therefore decided to study activity and its correlations after spatially averaging in the periodic direction. This way we obtain enough statistics and yet can still test for the expected scaling behaviour.

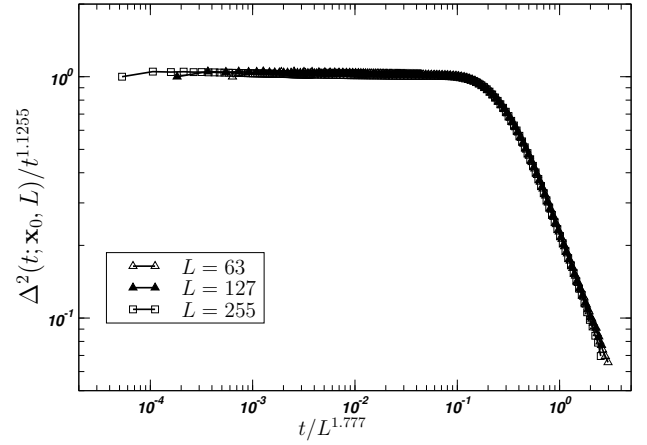


FIG. 20: Collapse of the width $\Delta^2(t; \mathbf{x}_0, L)$ (Eq. (28)) in the three-dimensional, centre driven Manna Model. Data is binned. Both axes have been rescaled using the dynamical exponent $z = 1.777(4)$ found in the literature [19], with $2/z \approx 1.1255$.

As indicated in Eqs. (16) and (17), averaging (or, for that purpose, summing) the time-integrated activity over the periodic direction reproduces the one-dimensional profile Eq. (12). The resulting profiles of the time-integrated activity summed over the periodic direction look therefore up to a pre-factor exactly like Fig. 6.

Activity-activity correlations on the other hand show some clear non-trivial scaling as a function of space. Defining the time-integrated, sheet-averaged activity in terms of the numerical observable $n_i(\mathbf{x}, t; \mathbf{x}_0, L)$ as

$$\widetilde{G}(x; \mathbf{x}_0, L) = \frac{1}{\sum_{i=1}^M T_i} \sum_{i=1}^M \sum_{t=1}^{T_i} \frac{1}{L^{d-1}} \sum_{y'_2, \dots, y'_d} n_i(\mathbf{x}, t; \mathbf{x}_0, L) \quad (50)$$

produces a function of essentially only one variable, x , the position in the open direction with the shape shown in Fig. 6, see Eq. (17). The activity-activity correlation functions may be defined in the same vein,

$$\begin{aligned} \widetilde{C}_u(x_2, x_1; \mathbf{x}_0, L) &= \frac{1}{\sum_{i=1}^M T_i} \sum_{i=1}^M \sum_{t=1}^{T_i} \frac{1}{L^{d-1}} \\ &\times \sum_{y''_2, \dots, y''_d} n_i(\mathbf{x}_2, t; \mathbf{x}_0, L) \sum_{y'_2, \dots, y'_d} n_i(\mathbf{x}_1, t; \mathbf{x}_0, L) \end{aligned} \quad (51)$$

and

$$\begin{aligned} \widetilde{C}_c(x_2, x_1; \mathbf{x}_0, L) &= \frac{1}{\sum_{i=1}^M T_i} \sum_{i=1}^M \sum_{t=1}^{T_i} \frac{1}{L^{d-1}} \\ &\times \sum_{y''_2, \dots, y''_d} n_i(\mathbf{x}_2, t; \mathbf{x}_0, L) \sum_{y'_2, \dots, y'_d} n_i(\mathbf{x}_1, t; \mathbf{x}_0, L) \\ &\quad - \widetilde{G}(x_2; \mathbf{x}_0, L) \widetilde{G}(x_1; \mathbf{x}_0, L), \end{aligned} \quad (52)$$

with $\mathbf{x}_1 = (x_1, y'_2, y'_3, \dots, y'_d)$ and $\mathbf{x}_2 = (x_2, y''_2, y''_3, \dots, y''_d)$. Noticeably, \mathbf{x}_1 and \mathbf{x}_2 have

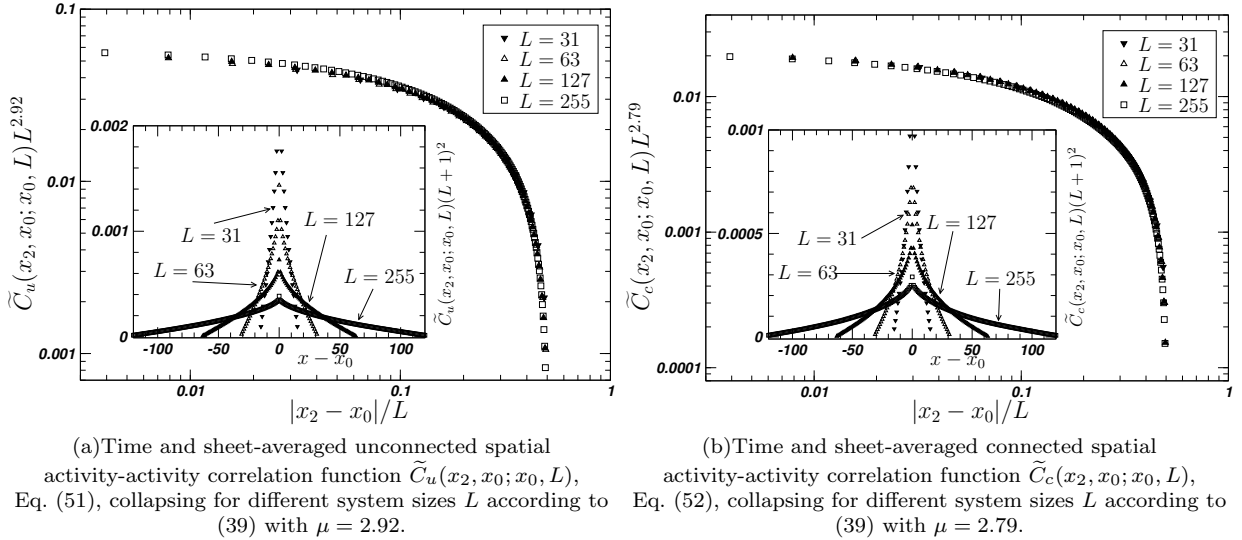


FIG. 21: Collapses according to Eq. (39) of the two point spatial correlation function \tilde{C}_u and \tilde{C}_c as defined in Eqs. (51) and (52) respectively for different three-dimensional system sizes as indicated. The exponent μ used is largely consistent with literature values. The insets show the correlation function on linear scales, however rescaled by the size of a sheet, $(L + 1)^2$, so that different system sizes L can be shown simultaneously. See also Fig. 12(b).

each $d - 1$ dashed components which are summed over independently, with the intention to render $\tilde{C}_{c,u}$ correlation functions of spatial averages rather than spatially averaged correlation functions. This is a matter of choice, motivated by the independence of the two coordinates in Eq. (40).

Both correlation functions collapse very nicely under suitable rescaling, similar to Fig. 12(b). Fig. 21 shows the collapses by plotting $\tilde{C}_{u,c}(x_2, x_1; \mathbf{x}_0, L)L^\mu$ against $|x_2 - x_1|/L$, Eq. (39), with $\mu = 2.92$ for the unconnected correlation function \tilde{C}_u and $\mu = 2.79$ for \tilde{C}_c . Just like in one dimension, we have chosen $x_1 = x_0$, *i.e.* one sheet in the two-point correlation function is the one where the driving takes place. The exponent μ should be compared to $1 - \gamma'/\nu_\perp = 2.74(3)$ from [9] or $2(d + z - D) = 2.81(3)$ [19], see the discussion after Eq. (39). These two values from scaling relations do not fully agree, but not as significantly as in one dimension, where they suggest 0.59(4) and 0.38(5) respectively. Moreover, the collapses with $\mu = 2.92$ and $\mu = 2.79$ are relatively better compatible with these literature values in both cases (in contrast to $\mu = 0.58$ in one dimension, which is much less compatible with 0.38(5) than with 0.59(4)). One may wonder that the unexpectedly inconsistent scaling is a feature of one dimension (see also [93]).

Finally we consider correlations of avalanche sizes on the macroscopic time scale. Compared to one dimension, where correlation “times” (measured in number of avalanches attempted) are fairly short and do not increase dramatically with system size, correlations in three dimensions last much longer and rise significantly. Fig. 22 shows the correlation function (in the inset, Eq. (48)) and the estimated correlation times, which change from

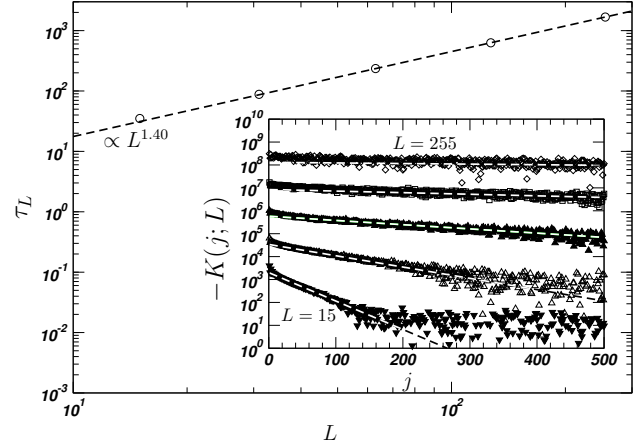


FIG. 22: Scaling of the macroscopic avalanche-avalanche correlation time τ_L with the system size L . The power law fitted (dashed line), $\tau_L \propto L^{1.40}$ is compatible with the prediction $\tau_L \propto L^{D-2}$ with $D = 3.370(11)$ [19]. In three dimensions, correlation times are very long and rise quickly compared to one dimension (*cf.* Fig. 15). The inset shows the negative of the actual correlation function $K(j; L)$ for $L = 15, 31, \dots, 255$ with the exponential fits (by eye), $A_L \exp(-j/\tau_L)$, shown as dashed lines.

around 35 avalanches at $L = 15$ to about 1680 avalanches at $L = 255$. Fitting the correlation time against the system size results in an exponent of 1.40, which is not too far off the expected value of $D - 2 = 1.370(11)$ [19] (see discussion after Eq. (48)).

B. Five dimensions

Five dimensions are supposedly above the upper critical dimension and so the Manna Model should display the same asymptotes and, in particular, the same scaling, as its Mean Field Theory [60], where $z = 2$ and $D = 4$ [9]. Because of the high dimensionality, the linear extent of the systems studied numerically is rather limited. The largest lattice we used was thus $L = 95$ with $95 \cdot 96^4 \approx 8 \cdot 10^9$ sites. With a particle density of $\zeta_\infty \approx 0.55$ that means one cannot reasonably expect the system to equilibrate within 10^7 avalanches when starting from an empty lattice. For these very large systems, we decided to determine the bulk density on a smaller lattice (starting from $L = 15$, having $983040 < 10^6$ sites) over the course of 10^8 avalanches, and use that density uniformly as the initialisation for the next bigger lattice. In each case, we dismissed $2 \cdot 10^7$ avalanches as transient.

As seen already in the sharpening of the density profile from one dimension, Fig. 1, to three dimensions, Fig. 17, in five dimensions, Fig. 23, the density across different four-dimensional sheets of constant x is nearly the same everywhere in the system. Only around $x = 1, 2, 3$ and $x = L, L - 1, L - 2$ a deviation from the bulk density ζ_∞ is actually noticeable but still is minute. To determine ζ_∞ , we have fitted ζ_L against $\zeta_\infty + aL^{-\epsilon}$ with fitting parameters ζ_∞ , a and ϵ . From $L = 15, 31, 63, 95$ we found $\zeta_\infty = 0.559780(5)$ (and $\epsilon = 0.94(1)$) with a goodness of fit of 0.70, which is to some extent owed to the small number of data points and the comparatively large number of fitting parameters. In the inset of Fig. 23(b) we used $\zeta_\infty = 0.55975$ instead, as it produced a more systematic dependence of the apparent cutoff on the system size. In that figure, we show that the small deviations of the substrate density from the bulk value close to the boundaries is reproduced for different system sizes and may display some power law dependence on the distance (similar to Figs. 1(b) and 17(b)). Unfortunately the data is too noisy to extract a reliable estimate of the exponent. Fig. 23(b) shows exponent -2 for comparison.

While the particle density is non-universal and difficult to capture theoretically, the total activity $R(t; \mathbf{x}_0, L)$, Eq. (18) (Sec. III C 1), as shown in Fig. 24 and its normalised form $\widehat{R}(\tau; \mathbf{x}_0, L)$, Eq. (27) (Sec. III C 2), as shown in Fig. 25, display universal scaling, as shown in Figs. 7(b) and 8, in one dimension and in Figs. 18 and 19 in three dimensions. The former, $R(t; \mathbf{x}_0, L)$, is based on the collapse of the rescaled activity as a function of suitably rescaled time, the latter, $\widehat{R}(\tau; \mathbf{x}_0, L)$ on the universal shape of the activity profile averaged after scaling it to the interval $[0, 1]$.

Fig. 24 shows the activity $R(t; \mathbf{x}_0, L)$ as a function of rescaled time using the exponent $z = 2$, Eq. (23). Indeed, no initial slope $\propto t^{(2-z)/z}$ is visible in $R(t; \mathbf{x}_0, L)$, as expected for $z = 2$, Eq. (22) (see Sec. III C 1). Accordingly, the collapse occurs when time is rescaled by L^2 . The inset shows a comparison to the MFT as introduced in Sec. II B. While the match is far from perfect, it

shows a noticeable improvement over the data for $d = 3$, Fig. 18, and the data for $d = 1$, Fig. 7. It could surely be improved further by rescaling the activity so that it matches, initially, the density of immobile particles, ζ_∞ , as the activity at $t = 0$ is exactly the probability of the initial particle (supplied by the external drive) arriving at an occupied site. A qualitative difference to the situation in $d = 3$ and $d = 1$ (Fig. 18 and Fig. 7(a) respectively) is the fact that the activity drops almost monotonically, apart from a very slight initial increase. In $d = 3$ and $d = 1$ it shows a very clear maximum, that exceeds unity in both cases.

Fig. 25 shows a comparison of the (specially normalised) activity profile $\widehat{R}(\tau; \mathbf{x}_0, L)$ according to Eq. (27) and the profile expected from mean field theory, *i.e.* the branching random walk (Sec. III C 1), which are expected to share the same universal shape. The data for the five-dimensional lattice is in good agreement with the MFT. Because of the large avalanche duration exponent $\alpha = 2$ and avalanche size exponent $\tau = 3/2$ [4] in five dimensions, relatively many avalanches are short in time and small in size, so that the data used for $\widehat{R}(\tau; \mathbf{x}_0, L)$ in Eq. (27) is mostly rather stepped. That results in visible artefacts as seen in Fig. 25, made worse by the fact that the artefacts align for different system sizes. The situation can be improved by using Poissonian updating which smears out the steps or by introducing a cutoff to suppress avalanches below a certain size.

Comparing the data in Fig. 25 to that in Fig. 19 suggests that the mean-field theory works better or applies at least as well in three dimensions as in five. One possible explanation is that system sizes in five dimensions are much smaller and so the coincidence between mean field theory and data in five dimensions would actually be significantly better, if bigger system sizes were available. Inspecting the data in Fig. 19 suggests that the data may display convergence away from the mean-field curve, whereas the data in Fig. 25 is still compatible with a convergence towards it. However, even the mean-field data is based on a comparatively small lattice ($L = 255$, see Sec. III C 1) and might change slightly as bigger lattices are considered. As in three dimensions, there is a slight slant in opposite directions in the MFT data and the data from the Manna Model. Plotting $\widehat{R}(1 - \tau; \mathbf{x}_0, L)$ against the MFT significantly improves the collapse.

We expected the mean squared displacement $\Delta^2(t; \mathbf{x}_0, L)$, Eq. (28), to be almost perfectly linear in time t in five dimensions, corresponding essentially to the behaviour of a random walker, so that the data collapses under rescaling of time by L^2 and $\Delta^2(t; \mathbf{x}_0, L)$ by t , Fig. 26. The data in three dimensions, Fig. 20, displayed a near-perfect collapse and very clear asymptotics. It turns out, however, that the data for the five-dimensional system, Fig. 26, is not as clear and clean as in three dimensions, although it collapses nicely under the rescaling expected. Two issues might play an important rôle: Firstly, the linear extent of the lattices, which effectively limit the maximum mean-square displacement

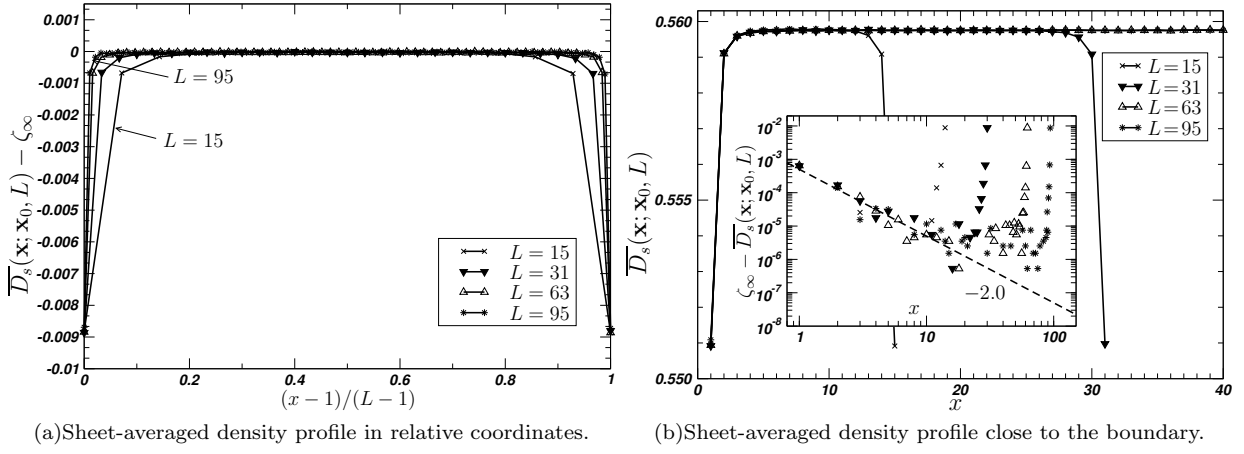


FIG. 23: The density of inactive particles in the quiescent state at stationarity in five dimensions as the deviation from the bulk density $\zeta_\infty = 0.559780(5)$, cf. Figs. 1 and 17. As in three dimensions, the observable has been taken as a spatial average in the periodic direction (sheets of constant x). (a) The shoulder of the density close to the boundary is even sharper than in three dimensions, Fig. 17(a). (b) Different system sizes show essentially identical shoulders (spatial scale identical to Fig. 1(b) and Fig. 17(b)). As shown in the inset, we were unable to detect a clear power law decay away from the boundary of the deviation of the density from its bulk value ζ_∞ , because the deviations are minute, the data comparatively noisy and any estimate for the exponent clearly dependent on the estimate of ζ_∞ , which we adjusted here to 0.55975. The line for -2 is shown for comparison to Fig. 17(b). The numerical data is shifted by 1 on the x -axis to produce a cleaner power law.

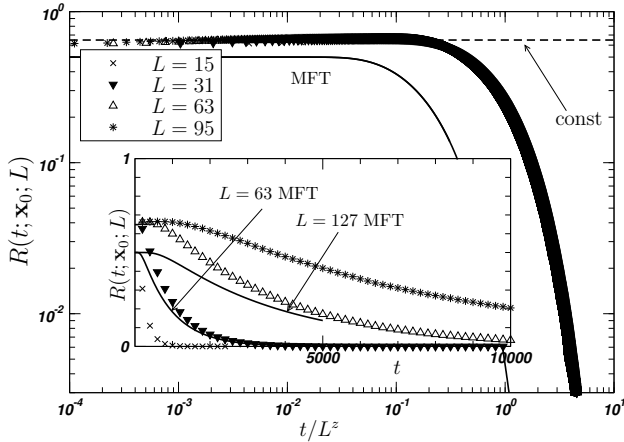


FIG. 24: Collapse of the spatially integrated activity, $R(t; \mathbf{x}_0, L)$, for the centre driven Manna Model in five dimensions (see Fig. 7 and Fig. 18 for the data in one and three dimensions respectively), plotting $R(t; \mathbf{x}_0, L)L^{2-z}$ against t/L^z using the literature value of $z = 2$ [9]. The dashed line shows the expected slope $(2 - z)/z = 0$, the full line the collapse ($L = 63, 127$) of the MFT (labelled). The inset shows the (pruned) data on a linear scale together with the MFT as in Fig. 7(a).

from above and the finite size corrections from below. These are small in five dimensions (maximum $L = 95$) compared to three (maximum $L = 255$). Secondly, the exponents used in the collapse in five dimensions are the analytical values expected. Allowing them to deviate slightly from that (thus becoming effective exponents for the given range of system sizes) improves the quality

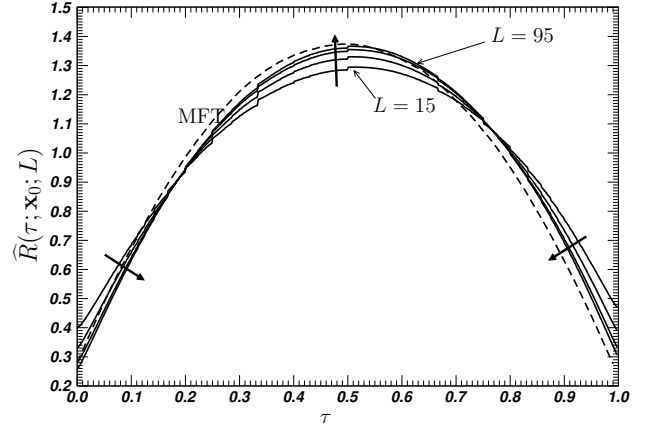


FIG. 25: The rescaled activity $\hat{R}(\tau; \mathbf{x}_0, L)$ in five-dimensional systems of size $L = 15, 31, 63, 95$ driven at the centre, $x_0 = (L + 1)/2$, to be compared to the behaviour in one (Fig. 8) and three dimensions (Fig. 19). The thick arrows point in the direction of increasing system size. The rescaling of time maps the spatially integrated activity to the interval $\tau \in [0, 1]$. Normalisation is applied so that the integral under the curve is unity. The numerical data for five dimensions is somewhat “rugged” (mostly for small system sizes) because of the many small avalanches which produce stepped activity profiles. The mean-field theory is shown as a dashed line, ($L = 255$, see Fig. 8).

of the collapse by compensating for some of the finite size corrections, something that was not needed in three dimensions (possibly because of the larger linear extents used there), which was based on the literature value.

Finally, Fig. 27 shows a collapse of the unconnected

and the connected activity-activity correlation functions, Eq. (51) and (52) respectively. Again, the collapse is based on the analytical value of the exponent $\mu = 2(d+z-D)$ (see Eq. (39) and the discussion thereafter), which gives $\mu = 6$ because $z = 2$ and $D = 4$ at $d = 5$. This is not equivalent to $\mu = d - \gamma'/\nu_\perp$ which gives $\mu = d$ as γ' is expected to vanish for all $d \geq d_c = 4$ [44]. The reason for the mismatch is that in dimensions above the upper critical dimension, the variance of the total activity no longer follows $\Delta\rho_a \propto L^{\gamma'/\nu_\perp}$ with $\gamma' = 0$ as suggested in Eq. (40), but, rather, drops off like L^{4-d} , so that $\Delta\rho_a L^{-d} \propto L^{-\mu}$ produces $\mu = 2d - 4$ (see also the discussion around Eq. (40)). This is because activity is confined to a volume of size L^4 whenever $d \geq 4$, while the variance of the activity density drops like L^{-d} , so the space integrated variance is $\Delta\rho_a \propto L^{4-d}$.

However, the collapses in Fig. 27 are surprisingly poor compared to the three-dimensional counterpart (Fig. 21). The same qualifications as above apply (small system sizes in five dimensions and the exponents in five dimensions not chosen to optimise the collapse as in $d = 1$, Fig. 12, but not in $d = 3$). In the present case $\mu = 6.2$ works best for \tilde{C}_u and $\mu = 6.1$ works best for \tilde{C}_c . Moreover, one may argue that space is more accurately rescaled by $|x_2 - x_0|/(L-1)$, because $|x_2 - x_0|$ ranges from 0 to $(L-1)/2$. However, even at the small linear system sizes used, this makes only a very small visible difference and does not improve the collapse significantly.

Considering finally the avalanche-avalanche correlations on the macroscopic time scale in five dimensions, it turns out that correlation times are extremely long and the signal prohibitively noisy. It is virtually impossible to fit an exponential against the correlation function, even when allowing for very large error bars. After some window-averaging, the smallest system size $L = 15$ gives a correlation time (measured in number of attempted avalanches) of about 4000, but the next larger, $L = 31$ has one at around 20000 avalanches. Data for $L = 63$ does not produce any reasonable results even after taking

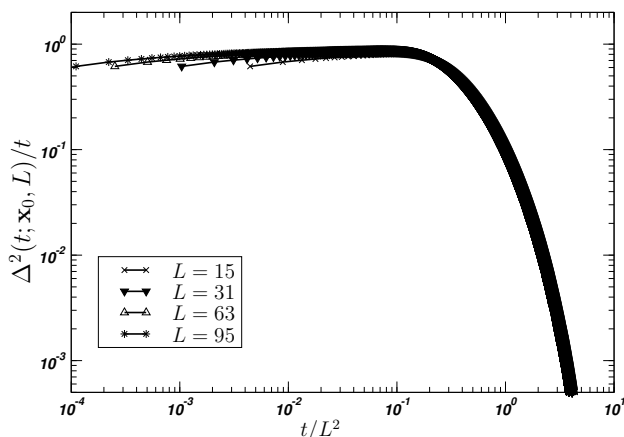


FIG. 26: Collapse of the width $\Delta^2(t; \mathbf{x}_0, L)$ (Eq. (28)) in the five-dimensional, centre driven Manna Model. Data is binned.

window averages. This result is all the more lamentable, as it would have been interesting to verify the scaling $\propto L^{D-2}$ of the correlation time above the upper critical dimension. This will require, however, many more than the $8 \cdot 10^7$ avalanches that we considered.

V. DISCUSSION AND CONCLUSION

The key-objective of the present numerical study was to provide an extensive survey of spatio-temporal correlations in SOC. They are frequently overlooked as the hallmark of criticality, as the vast majority of numerical studies focuses on integrated observables, such as the space-time integral of the activity during an avalanche (avalanche size) or its duration. As most clearly seen in one dimension, this is to large extent justifiable by the complications that arise from the additional independent variables (such as distances in time and space), the often noisier numerics and the less convincing scaling behaviour, even when modern computing resources can compensate for some of these disadvantages.

On the other hand, much of what “self-organised criticality” ought to display, in particular self-organisation and spatio-temporal self-similarity [6], is very well captured and in fact confirmed by the correlation functions studied above. Among the numerical results presented, the independence of the density profile of the substrate from the driving position, further supported by the calculations in the appendix, stands out as one of the clearest signs of self-organisation [40]. Interestingly, correlations in the substrate (Fig. 2) have a small amplitude, which does not scale with the system size. This is very much in contrast to other models, such as the OFC Model [94], where correlations are very visible and part of the evolution towards a (supposedly) scale invariant steady state [36, 95]. The lack of correlations is apparently also in sharp contrast to the fixed energy version of the Manna Model, as Basu *et al* refer to “the natural long-range correlations in the background” [37] and the hyperuniformity found by Hexner and Levine [75], which we confirmed above Sec. III B. In fact, Grassberger, Dhar and Mohanty [40] have successfully used *periodic* initial conditions in the closely related Oslo Model to reduce transients. In other words, there are clear indications of correlations, but they are not easily measured in the density autocorrelation function studied above.

The effect of the boundary on the substrate particle density further in the bulk is discernible only for a small, fixed number of sites (a number of sites that does not increase with system size), because the amplitude of the deviation from the bulk density does not scale in L . Yet, there is a visible power law decay of the boundary effect, cut off by the system size, see Figs. 1(b), 17(b) and 23(b). As that data is rather noisy and the amplitude does scale up with system size, at a large scale the boundary will barely be noticeable in the density of immobile particles in the bulk. In contrast, it is very clearly visible in the

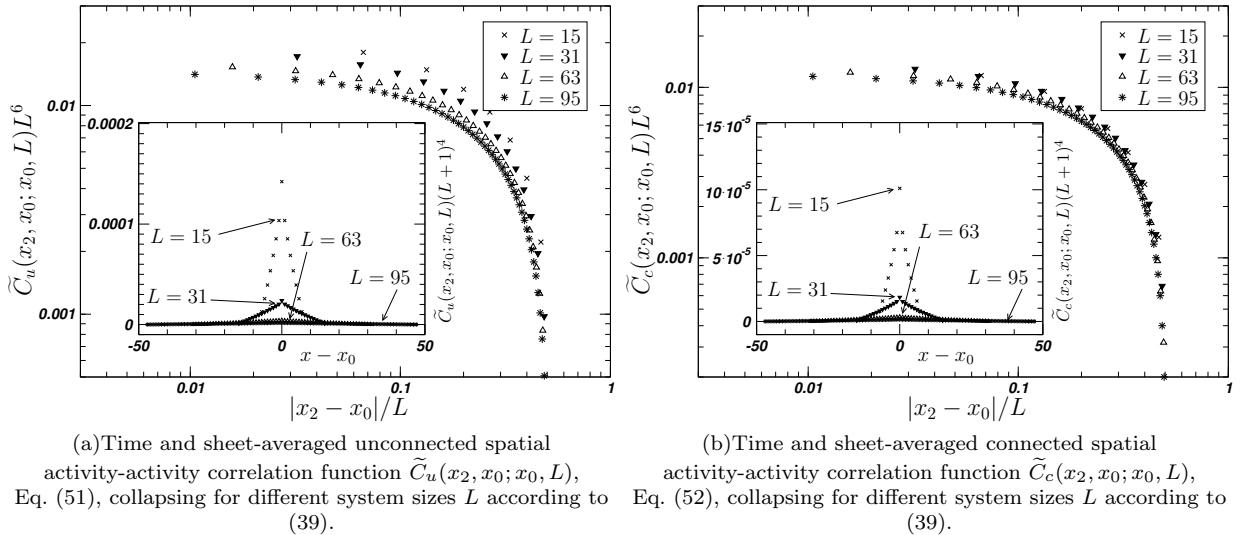


FIG. 27: Collapses according to Eq. (39) of the two point spatial correlation function \tilde{C}_u and \tilde{C}_c as defined in Eqs. (51) and (52) respectively for different five-dimensional systems as indicated. The exponent $\mu = 6$ is the theoretical value (see main text). The insets show the correlation function on linear scales, however rescaled by the size of a sheet, $(L + 1)^4$, so that different system sizes L can be shown simultaneously. See also Fig. 12 and Fig. 21.

activity, Fig. 6 and Eq. (12), which is dissipated at the open boundaries of the system [55, 56]. The triangular shape of the time-integrated activity is certainly not “guided” by the almost featureless density of particles in the substrate. The activity throughout would surely be affected by a change in substrate density, but the latter self-organises such that the time integral of the former displays the behaviour of mere random walkers, which at stationarity have no sinks or sources in the bulk other than by driving.

That the environment organises visibly only as far as a scalar density is concerned is different to the seemingly more complicated picture emerging from experiments, say the ricepile [96], where particles appear to arrange so a newly added one finds itself in a system that mediates long range interaction. In the Manna Model, self-organisation manifests primarily in a scalar density of substrate particles and during avalanches, when large correlations of active particles arise whose amplitude scales with system size. One may test this hypothesis further by destroying the spatial correlations explicitly, while leaving the densities profile unchanged [97]. This is probably best done in dimensions $d > 1$, because of the uniformity of the density in the periodic directions.

In summary, the self-organisation on the macroscopic time scale affects almost exclusively the bulk density of immobile particles and does not seem to result in them being significantly correlated. As far as self-organisation towards the critical state is concerned, in the present study we have not encountered significant effects in the system, other than the critical scaling in the active state itself. Even, the algebraic scaling of the density away from the boundary, as shown in Figs. 1(b), 17(b) and 23(b), has no discernible effect on the bulk, even when

the correlation length seems to be of order L . None of the features in the bulk of the substrate (can) have an amplitude that scales with the system size and therefore may easily be overlooked in natural systems. Although self-organisation to the critical density takes place, at quiescence we were unable to detect an unambiguous fingerprint of criticality.

The substrate particle density displays a noisy power law decay of the (small) deviation from the bulk value away from the boundaries, see Figs. 1, 17 and 23. The amplitude of that deviation cannot possibly increase indefinitely with system size and thus may, again, be difficult to detect in real systems in particular without a well-defined lattice spacing. Otherwise, the space-dependence of the substrate particle density is rather trivial and almost featureless. One may be tempted to say the same about the time-integrated response function (Fig. 6), although a characteristic scale, *i.e.* a correlation length, can be (analytically) identified as the system size and the amplitude scales linearly in L . The time-resolved response has some significant spatial structure (Fig. 5, also Fig. 10) and the characteristic length scale, a correlation length, is indeed the system size, as can be seen vividly in Fig. 6. However, without time-dependence, the response function is that of a random walker with $\eta = 0$ and no renormalisation of the diffusion constant.

The scaling of the correlation function of the activity, on the other hand, confirms the picture that spatial correlations build up over microscopic time (such as $t \propto |x - x_0|^z$ in Fig. 11 and $t^*(L)$ in Fig. 12(a)) but are eventually curbed by the system size L (*e.g.* inset of Fig. 12(a), Fig. 12(b)). As a result, the scaling that is ultimately (in the long-time limit) displayed by the Manna Model is finite size scaling. For the correlation

functions, this result is far from trivial — as the process takes place on the lattice, there is no dimensional reason for the correlation length not to be a non-trivial power of the system size. Nevertheless, the correlation length (*i.e.* the decay length of the correlation functions) is indeed proportional to the system size (as demonstrated in Fig. 12), so that standard finite size scaling applies.

For quantities such as the time-integrated response $\widehat{G}(\mathbf{x}; \mathbf{x}_0, L)$, the scaling with $(x - x_0)/L'$ can be determined analytically, Eqs. (12) and (14). This is a general theme: the scaling in space of the response is to large extent determined by the particles' trajectories being random walks. No such mapping exists for higher order correlation functions. Scaling in time, on the other hand, is generally non-trivial. For example, the mean squared displacement $\Delta^2(t; \mathbf{x}_0, L) \propto t^{2/z}$ (for $t \ll L^z$, see discussion after Eq. (20)) displays strongly superdiffusive behaviour as activity ceases only at low local (immobile) particle densities, *i.e.* where it has not ceased in the past. Only above the upper critical dimension, where $z = 2$, does the mean squared displacement slow down to reach $\Delta^2(t; \mathbf{x}_0, L) \propto t$, Fig. 26. In that sense, the temporal behaviour is richer than the spatial behaviour.

On the other hand, higher correlation functions (technically, three-point correlation functions) display a highly non-trivial spatial structure, *e.g.* Fig. 12, Fig. 21 and Fig. 27. The presence of spatio-temporal scaling of the activity (including its amplitude) is reassuring and has to be seen in contrast to the absence of finite size scaling of the amplitude of the (weak) anti-correlations in the (immobile) substrate particles, Fig. 2, which are bounded just as the density is. Summarising these findings, one might be tempted to generalise that the substrate, the “backdrop” of the activity, is not the best place to search for correlations and scaling in SOC. At least our direct measurements of the one-point and two-point correlation functions did not reveal any scaling of the amplitude with system size. In the Manna Model, interesting behaviour is most easily found in the activity.

We have also considered temporal correlations on the macroscopic timescale, not least in order to validate and generalise the mapping of SOC to interfacial growth [12]. This seems to work well in one and three dimensions, but in five dimensions was hampered by the enormously long correlation times. If valid, the correlation time between avalanche sizes on the macroscopic time scale scales like L^{D-2} , *i.e.* avalanches separated by $\propto L^{D-2}$ avalanche attempts may be considered as independent. As the average number of topplings scales like L^2 and determines the CPU-time needed to perform the avalanches, the average amount of CPU-time for independent events scales like L^D , to be considered when selecting observables (possibly in the presence of self-averaging [4, 98]).

The most concerning result above is the significant deviation from the literature value of the dynamical exponent z in one dimension, as estimated in the collapses above. Worse, some of the exponents are inconsistent even for the same observable. The problem is confined

to one dimension, with data for $d = 3$ producing all the expected behaviour, while $d = 5$ shows some deviations, likely to be caused by finite size effects. In the following, we focus on the problems in one dimensions and discuss possible explanations.

The dynamical exponents in one dimension that we found were $z = 1.51$ for the collapse of the spatially integrated activity (Fig. 7(b)), but also $z = 1.574$ from the slope in small t in the same plot (which however assumes constant $\tilde{\mathcal{F}}_0$, see discussion at the end of Sec. III C 1). Further, we found $z = 1.5625$ from the scaling of the mean squared displacement (Fig. 9(a)), $z = 1.445$ to $z = 1.59$ for the scaling of the response propagator in time at fixed spatial coordinates (Fig. 10), $z = 1.59$ (but not $z = 1.445$) for the scaling of the response in space at short times (Fig. 11) and finally $z = 1.71$ if $\lambda^{-1} = z$ for the spatial scaling of the unconnected correlation function in Fig. 12(a). The scaling of the time averaged correlation function can be related to the dynamical exponent through two different scaling relations which are not fully consistent. Choosing the one based on SOC observables (see discussion after Eq. (42)) gives $z = \mu/2 + D - d = 1.543(14)$ for the data shown in Fig. 12(b) and using $D = 2.253(14)$ from [18]. The alternative scaling relation $\mu = d - \gamma'/\nu_\perp$ produces $\mu = 0.59(4)$ [9], validating the scaling found in Fig. 12(b), but seems to clash with $\mu = 2(d + z - D)$.

To acknowledge the significance of the disparity of the dynamical exponents in one dimension, it is worth comparing to three dimensions, where results are quite consistent: The spatially integrated activity collapses nicely with the literature value $z = 1.777(4)$ (Fig. 18) even for the slope in small t , as does the mean squared displacement (Fig. 20). The average spatial activity-activity correlation function shows some variability, Fig. 21, as $z = \mu/2 + D - d = 1.830(11)$ for the unconnected correlation function (Fig. 21(a), $\mu = 2.92$) and $z = \mu/2 + D - d = 1.765(11)$ for the connected one (Fig. 21(b), $\mu = 2.79$), based on $D = 3.370(11)$ in the literature [19]. The collapse of the unconnected correlation function is not as good as for the connected one and may generally be expected to display slightly worse scaling. In all, it seems that the numerics in three dimensions validate the methods and the scaling proposed. Further support comes from the numerics in five dimensions, if one accepts that the scaling was spoiled to some extent by finite size corrections.

The results in one dimension (*i.e.* the value of the dynamical exponent z) are worrying firstly because they clash with the literature values obtained in traditional SOC simulations. This is put in perspective by the variety of results reported, ranging from 1.393(37) [93] to 1.66(7) [99]. However, all literature values known to us, except $z = 1.445(10)$ in [18] were taken in variants of the Abelian Manna Model; $z = 1.47(7)$ [74] was obtained in the non-Abelian version of the Manna Model, $z = 1.66(7)$ [99] in the FES version, $z = 1.45(3)$ and $z = 1.54(5)$ [100] in different versions of the height-restricted FES

version, $z = 1.393(37)$ [93] in the non-Abelian version and $1.50(4)$ [101] in the FES version with height restriction. We would expect that as a matter of universality, the exponents found for these models should coincide with the measurements of correlation functions obtained above. In fact, some traditional SOC observables such as the avalanche size are “coarse grained” variations of observables used above, such as the spatial integral of the activity, $R(t; \mathbf{x}_0, L)$.

Secondly, as seen above, estimates for the dynamical exponent in one dimension found in the present work are inconsistent across different observables. This is particularly worrying in cases when the exponent is not measured by finding a collapse whose quality is difficult to assess, but when it is determined by measuring an “obvious” slope. Such a slope may, however, be obscured by the presence of a lower cutoff and a scaling function [79–81]. In case of $R(t; \mathbf{x}_0, L)$, shown in Fig. 7(b), a good collapse was obtained using $z = 1.51$. A less good one was obtained from $z = 1.445$. On the other hand, the initial slope ought to be $(2-z)/z \approx 0.325$ for $z = 1.51$, but turns out to be much closer to 0.27 , suggesting $z \approx 1.574$. Although the exponents characterising the slope are small, close inspection leaves little doubt about the latter. A similar clash of the dynamical exponents used in the collapse versus the one used in the initial time-dependence was *not* found for the width of the propagator Fig. 9(a).

To reconcile these results, one may revisit the scaling form Eq. (20) and relax it to

$$G(\mathbf{x}, t; \mathbf{x}_0, L) = a|\mathbf{x} - \mathbf{x}_0|^{-(d-2+\eta+z')} \times \mathcal{F}\left(\frac{\mathbf{x} - \mathbf{x}_0}{L^\sigma}, \frac{\mathbf{x} - \mathbf{x}_0}{bt^{1/z}}\right), \quad (53)$$

with additional exponents z' and σ . The time integral gives $\hat{G}(\mathbf{x}; \mathbf{x}_0, L)$, whose scaling is known exactly, Eq. (12), $\propto x^{2-d} \tilde{\mathcal{F}}(x/L)$ leading to Eq. (25) with $\eta = 0$. The corresponding result for the form (53) is $\eta + z' = z$ and $\sigma = 1$, reproducing Eq. (20). The pre-factor of L^{2-z} in Eq. (23) then follows from the spatial integral of Eq. (53) which gives $-(d-2+\eta+z') + d\sigma = 2-z$. As for the scaling in small $t \ll L^z$, integrating Eq. (53) in space to produce $R(t; \mathbf{x}_0, L)$ gives necessarily the scaling form Eq. (22) with $\eta = 0$,

$$R(t; \mathbf{x}_0, L) = a \left(\frac{t}{b}\right)^{(2-z)/z} \tilde{\mathcal{F}}_0\left(\frac{t}{b'L^z}\right).$$

The only possible reason why $R(t; \mathbf{x}_0, L)$ scales in small t not as $t^{(2-z)/z}$ is that $\tilde{\mathcal{F}}_0(\dots)$ is itself a power law. That, however, implies that $\lim_{L \rightarrow \infty} R(t; \mathbf{x}_0, L)$ is not finite, *i.e.* either diverges or vanishes, which cannot possibly happen, because the total activity across the entire system at fixed time must be monotonically increasing in L , yet is bounded from above (for example by 2^t).

The exponent describing the initial slope is rather small, we found $(2-z)/z \approx 0.27$ as shown in Fig. 7(b), whereas the collapse was done with $z = 1.51$, so that

$(2-z)/z \approx 0.325$ as if $\tilde{\mathcal{F}}_0(u) \propto u^{-0.055}$. However, the numerics giving $(2-z)/z \approx 0.27$ is very reliable, suggesting that one should much rather consider $z = 2/1.27 \approx 1.575$ as the “correct” value of z . That value of z produces a good collapse in small t , but a comparatively poor one in the tail. The picture thus remains dissatisfying: As far as the collapse Fig. 7(b) is concerned, the powerlaw of the initial slope $\propto t^{(2-z)/z}$ cannot be made consistent with the exponents needed for a satisfactory collapse. Both exponents are larger than what we think is the most reliable literature value, $z = 1.445(10)$, which is close to the conjectured value of $z = 10/7 = 1.42857\dots$ for the Oslo Model [40].

Based on our data we conclude that the scaling form Eq. (20) must be suffering from very significant corrections. One might wonder whether this is a matter of, say, the assumption of translational invariance mentioned after Eq. (20). This assumption could be relaxed by allowing x_0/L (in one dimension) as an argument of the scaling function. However, $x_0/L = 1/2 + 1/(2L)$ was essentially constant for the different L considered.

A more daunting explanation for the poor consistency of the exponents is the definition of the time scale. We have repeated some of the simulations in one dimension using a Poissonian waiting time between topplings and found that the picture does not change significantly. While a collapse like Fig. 7(b) works well with $z = 1.48$ (*cf.* 1.51 above), the initial slope still suggests $z = 1.59$ (*cf.* 1.575 above).

Another observable that, in one dimension, displays unexpectedly poor scaling with exponents from the literature is the width of the propagator $\Delta^2(t; \mathbf{x}_0, L)$, Eq. (28), as shown in Fig. 9 (with $z = 1.5625$). Like the total activity $R(t; \mathbf{x}_0, L)$, this is essentially a spatial integral of the propagator. In this case, the initial slope, $\propto t^{2/z}$, which features very clearly, and the exponent to collapse can be chosen consistently. However, $z = 1.5625$ is well away from the expected value of $z = 1.445(10)$. In fact, further inspection suggests that the collapse and the match of the initial slope may possibly be further improved by taking z as large as $z = 1.59$. An exponent of $z = 1.445$ looks very poor in comparison, certainly for the initial slope, which is more clearly visible for $\Delta^2(t; \mathbf{x}_0, L)$ in Fig. 9(a) than for $R(t; \mathbf{x}_0, L)$ in Fig. 7(b).

A possible explanation for the inconsistencies with the literature values for the exponents are the corrections that were allowed for in the latter, but are difficult to capture in a collapse. According to Eq. (29) $\Delta^2(t; \mathbf{x}_0, L)L^2$ collapses when plotted against t/L^z . Instead of taking any specific z , one may use an estimate of the characteristic time scale $T_c(L)$, which scales like L^z only to leading order, to rescale time by $1/T_c(L)$ rather than $1/L^z$. The characteristic time scale is proportional to the moment ratio $\langle T^2 \rangle / \langle T \rangle$ (the second moment of the duration over the first). A collapse is therefore expected by plotting $\Delta^2(t; \mathbf{x}_0, L)L^2$ against $t \langle T \rangle / \langle T^2 \rangle$.

However, there is no improvement of the collapse in comparison to using L^z with $z = 1.445$. Even when con-

sidering only very small system sizes, $\langle T^2 \rangle / \langle T \rangle$ clearly scales with an exponent of less than $z = 1.5$, while the collapse clearly needs a dynamical exponent larger than $z = 1.55$.

In comparison with three dimensions, the one dimensional collapses display many inconsistencies. It was argued by Lübeck and Heger [93] that the Manna universality class splits in one dimension into two distinct ones, at least as far as absorbing state phase transitions are concerned. Basu *et al* [37] suggested that such fixed energy sandpiles (FES) belonged “generically to [the] directed percolation” universality class, although they studied in fact only the Manna Model and only in one dimension. Interestingly, Lee [102] pointed out that the observations made by Basu *et al* are confined to one dimension. In two dimensions, the scaling of the FES Manna Model clearly differs from that of directed percolation. The original claim by Basu *et al* was based on the observation that under improved numerical conditions five exponents studied (α , β , ν_{\perp} , ν_{\parallel} and z) were closer to directed percolation than previously reported in the literature [9].⁷ Their finding of $z = 1.51(5)$ is within the range of some of the findings above and remarkably far from their own estimate of $\nu_{\perp} = 1.095(5)$ and $\nu_{\parallel} = 1.75(5)$, which gives $\nu_{\parallel}/\nu_{\perp} = 1.60(5)$, supposedly equal to z . One may speculate whether their *de facto* observation of an inconsistent z (in one dimension only) is linked to ours. As far as the dynamical exponent is concerned, in one dimension many of the findings above for the Manna Model are not incompatible with directed percolation, $z = 1.580745(10)$ [103]. However, many others are incompatible. One may speculate whether this is due to an interplay of two microscopic timescales, the other one characterising avalanche durations, one characterising correlations, or the two microscopic length scales, namely finite distances on the lattice and its size.

Another surprise was the unexpectedly poor scaling in five dimensions. While the collapses worked (mostly) with exponents as expected from theory, their quality was not as good as most of those in three dimensions. In Fig. 24 the collapse worked essentially as expected, but Fig. 25 showed visible artefacts and produced results seemingly further away from MFT than the corresponding ones in three dimensions, Fig. 19. Similarly, the collapse of the width, Fig. 26, was good given the (expected) MFT exponent, yet somewhat disappointing for early times t/L^2 . The worst behaviour was found for the correlation function, Fig. 27, which showed clear deviations from the expected exponents. As mentioned above, the system sizes are bound to be very small in five dimensions — observables like the width are necessarily

bounded from above by the system size, while corrections are bounded from below. However, it seems somewhat inconsistent to accept finite size corrections as an explanation for the poor behaviour in $d = 1$ and $d = 5$ in the light of the very convincing results in three dimensions (which, nevertheless, validates many of the scaling assumptions).

To put the inconsistencies in perspective, one should keep in mind that collapses are a comparatively poor tool to extract exponents and as a result, to some extent also a poor test for scaling. Firstly, there are the corrections alluded to above. While these are well understood for the finite size scaling of individual moments [104, 105], we are not aware of a systematic way of introducing and assessing them in a data collapse, say

$$G(\mathbf{x}, t; \mathbf{x}_0, L) = a_1 |\mathbf{x} - \mathbf{x}_0|^{-(d-2+z)} \tilde{\mathcal{F}} \left(\frac{t}{b'L^z}, \frac{\mathbf{x} - \mathbf{x}_0}{bt^{1/z}} \right) + a_2 |\mathbf{x} - \mathbf{x}_0|^{-(d-2+z+\omega)} \tilde{\mathcal{F}}_2 \left(\frac{t}{b'L^z}, \frac{\mathbf{x} - \mathbf{x}_0}{bt^{1/z}} \right) \quad (54)$$

with $\omega > 0$, *cf.* Eq. (21). Secondly, the range within which the collapse is supposed to “work” is cut off towards the smaller scale, yet it is difficult to assert the value of that cutoff. Thirdly, statistical errors are difficult to estimate, other than via the range of exponents that seem to result in an acceptable collapse (whatever that may be). Finally, even a very simple form like (Eq. (29))

$$\Delta^2(t; \mathbf{x}_0, L) = a't^{2/z} \tilde{\mathcal{F}}_4 \left(\frac{t}{b'L^z} \right), \quad (55)$$

suggests a collapse of $\Delta^2(t; \mathbf{x}_0, L)t^{q-2/z}L^{-qz}$ versus t/L^z for *any* value of q . Technically, different q should make little difference, but a choice that makes the resulting range of the ordinate large, will blur displacements in that direction. Depending on the choice of q some deviations are more readily identified than others. For example, $q = 0$ (Fig. 9(b)) is more forgiving for deviations in the tail, whereas $q = 2/z$ is more forgiving for deviations in small t (*cf.* Fig. 9(a)). We used this choice consciously when we collapsed $R(t; \mathbf{x}_0, L)$ in Fig. 7(b), Fig. 18 and Fig. 24 by rescaling it by a power of L according to Eq. (23) (and “read off” the t -dependence according to Eq. (22)) rather than collapsing by Eq. (22).

In response to this ambiguity, and in light of the fact that a data collapse is best regarded as a tool to illustrate and possibly test for scaling, our initial decision was to plot all collapses with what is expected from the SOC literature [18, 19]. However, in one dimension, this led to very poor results, which could be improved easily by using different exponents, namely those shown. In contrast, in three and five dimensions, we mostly used literature values and the results were mostly good or satisfactory (mild but clear deviations were visible in the spatial activity-activity correlation function shown in Fig. 21 and Fig. 27).

⁷ Closer inspection reveals, however, that both α and ν_{\parallel} had already been reported [93] within one standard deviation of those by Basu *et al*, *i.e.* there has not been a claim that α or ν_{\parallel} were much different from those in directed percolation.

In summary, we see scaling of spatio-temporal correlations confirmed in the Manna Model of SOC. As far as self-organisation and scaling of activity and its correlations with system size go, the behaviour is as expected. In contrast, scaling in the substrate has small, fixed amplitudes and is difficult to detect. Some results in one dimension are inconsistent, but this is in line with other findings for the Manna Model in the FES mode [37, 93].

Acknowledgments

The authors gratefully acknowledge interesting discussions with D. Dhar, N. Huynh, P. Grassberger and N. Wei. The authors would also like to thank Andy Thomas and Niall Adams for computing support.

-
- [1] H. E. Stanley, *Introduction to Phase Transitions and Critical Phenomena* (Oxford University Press, New York, NY, USA, 1971).
- [2] U. C. Täuber, *Critical dynamics* (Cambridge University Press, Cambridge, UK, 2014).
- [3] P. Bak, C. Tang, and K. Wiesenfeld, *Phys. Rev. Lett.* **59**, 381 (1987).
- [4] G. Pruessner, *Self-Organised Criticality* (Cambridge University Press, Cambridge, UK, 2012).
- [5] A. van der Ziel, *Physica* **16**, 359 (1950).
- [6] N. W. Watkins, G. Pruessner, S. C. Chapman, N. B. Crosby, and H. J. Jensen, *Space Sci. Rev.* **198**, 3 (2016).
- [7] H. J. Jensen, K. Christensen, and H. C. Fogedby, *Phys. Rev. B* **40**, 7425 (1989).
- [8] D. Stauffer and A. Aharony, *Introduction to Percolation Theory* (Taylor & Francis, London, UK, 1994).
- [9] S. Lübeck, *Int. J. Mod. Phys. B* **18**, 3977 (2004).
- [10] H.-M. Bröker and P. Grassberger, *Phys. Rev. E* **56**, 3944 (1997).
- [11] K. Christensen and N. R. Moloney, *Complexity and Criticality* (Imperial College Press, London, UK, 2005).
- [12] M. Paczuski and S. Boettcher, *Phys. Rev. Lett.* **77**, 111 (1996).
- [13] G. Pruessner, *Phys. Rev. E* **67**, 030301(R) (pages 4) (2003), arXiv:cond-mat/0209531.
- [14] P. Bak, C. Tang, and K. Wiesenfeld, *Phys. Rev. A* **38**, 364 (1988).
- [15] C. Tang and P. Bak, *Phys. Rev. Lett.* **60**, 2347 (1988).
- [16] C. Tang and P. Bak, *J. Stat. Phys.* **51**, 797 (1988).
- [17] R. T. J. McAteer, M. J. Aschwanden, M. Dimitropoulou, M. K. Georgoulis, G. Pruessner, L. Morales, J. Ireland, and V. Abramenko, *Space Sci. Rev.* **198**, 217 (2016).
- [18] H. N. Huynh, G. Pruessner, and L. Y. Chew, *J. Stat. Mech.* **2011**, P09024 (2011), arXiv:1106.0406.
- [19] H. N. Huynh and G. Pruessner, *Phys. Rev. E* **85**, 061133 (2012), arXiv:1201.3234.
- [20] D. Dhar, *Phys. Rev. Lett.* **64**, 1613 (1990).
- [21] D. Dhar and S. N. Majumdar, *J. Phys. A: Math. Gen.* **23**, 4333 (1990).
- [22] S. N. Majumdar and D. Dhar, *J. Phys. A: Math. Gen.* **24**, L357 (1991).
- [23] S. N. Majumdar and D. Dhar, *Physica A* **185**, 129 (1992).
- [24] V. B. Priezzhev, *J. Stat. Phys.* **74**, 955 (1994).
- [25] E. V. Ivashkevich, *J. Phys. A: Math. Gen.* **27**, 3643 (1994).
- [26] S. Mahieu and P. Ruelle, *Phys. Rev. E* **64**, 066130 (pages 19) (2001), arXiv:hep-th/0107150.
- [27] P. Ruelle, *Phys. Lett. B* **539**, 172 (2002), arXiv:hep-th/0203105.
- [28] M. Jeng, *Phys. Rev. E* **71**, 016140 (pages 12) (2005).
- [29] M. Jeng, *Phys. Rev. E* **71**, 036153 (pages 17) (2005).
- [30] M. Jeng, G. Piroux, and P. Ruelle, *J. Stat. Mech.* **2006**, P10015 (2006), arXiv:cond-mat/0609284.
- [31] A. A. Saberi, S. Moghimi-Araghi, H. Dashti-Naserabadi, and S. Rouhani, *Phys. Rev. E* **79**, 031121 (pages 5) (2009).
- [32] N. Azimi-Tafreshi, H. Dashti-Naserabadi, S. Moghimi-Araghi, and P. Ruelle, *J. Stat. Mech.* **2010**, P02004 (2010), arXiv:0912.3331v2.
- [33] D. Dhar and R. Ramaswamy, *Phys. Rev. Lett.* **63**, 1659 (1989).
- [34] G. Grinstein, in *Scale Invariance, Interfaces, and Non-Equilibrium Dynamics*, edited by A. McKane, M. Droz, J. Vannimenus, and D. Wolf (Plenum Press, New York, NY, USA, 1995), pp. 261–293, NATO Advanced Study Institute on *Scale Invariance, Interfaces, and Non-Equilibrium Dynamics*, Cambridge, UK, Jun 20–30, 1994.
- [35] R. Dickman, A. Vespignani, and S. Zapperi, *Phys. Rev. E* **57**, 5095 (1998).
- [36] S. Lise, *J. Phys. A: Math. Gen.* **35**, 4641 (2002), arXiv:cond-mat/0204490.
- [37] M. Basu, U. Basu, S. Bondyopadhyay, P. K. Mohanty, and H. Hinrichsen, *Phys. Rev. Lett.* **109**, 015702 (2012).
- [38] S. D. da Cunha, L. R. da Silva, G. M. Viswanathan, and R. Dickman, *J. Stat. Mech.* **2014**, P08003 (2014), arXiv:1405.1134.
- [39] R. Dickman and S. D. da Cunha, *Phys. Rev. E* **92**, 020104 (2015).
- [40] P. Grassberger, D. Dhar, and P. K. Mohanty, *Phys. Rev. E* **94**, 042314 (2016).
- [41] P. Le Doussal and K. J. Wiese, *Phys. Rev. Lett.* **114**, 110601 (2015).
- [42] G. Pruessner (2017), in preparation.
- [43] S. Lübeck and A. Hucht, *J. Phys. A: Math. Gen.* **35**, 4853 (2002).
- [44] S. Lübeck and P. C. Heger, *Phys. Rev. Lett.* **90**, 230601 (pages 4) (2003).
- [45] K. Christensen, H. Flyvbjerg, and Z. Olami, *Phys. Rev. Lett.* **71**, 2737 (1993).
- [46] H. Flyvbjerg, K. Sneppen, and P. Bak, *Phys. Rev. Lett.* **71**, 4087 (1993).
- [47] S. A. Janowsky and C. A. Laberge, *J. Phys. A: Math. Gen.* **26**, L973 (1993).
- [48] S. Zapperi, K. B. Lauritsen, and H. E. Stanley, *Phys. Rev. Lett.* **75**, 4071 (1995).
- [49] K. B. Lauritsen, S. Zapperi, and H. E. Stanley, *Phys. Rev. E* **54**, 2483 (1996).
- [50] M. Vergeles, A. Maritan, and J. R. Banavar, *Phys. Rev. E* **55**, 1998 (1997).

- [51] A. Vespignani and S. Zapperi, *Phys. Rev. Lett.* **78**, 4793 (1997).
- [52] A. Vespignani and S. Zapperi, *Phys. Rev. E* **57**, 6345 (1998).
- [53] S. Lübeck (2003), personal communication.
- [54] C. B. Yang, *J. Phys. A* **37**, L523 (2004).
- [55] T. Hwa and M. Kardar, *Phys. Rev. Lett.* **62**, 1813 (1989).
- [56] M. Paczuski and K. E. Bassler (2000), eprint arXiv:cond-mat/0005340v2, arXiv:cond-mat/0005340v2.
- [57] A. Chessa, E. Marinari, and A. Vespignani, *Phys. Rev. Lett.* **80**, 4217 (1998).
- [58] A. Barrat, A. Vespignani, and S. Zapperi, *Phys. Rev. Lett.* **83**, 1962 (1999).
- [59] R. Pastor-Satorras and A. Vespignani, *Phys. Rev. E* **62**, 6195 (2000).
- [60] P. Le Doussal, K. J. Wiese, and G. Pruessner (2016), in preparation.
- [61] D. Dhar, *Physica A* **263**, 4 (1999), proceedings of the *20th IUPAP International Conference on Statistical Physics*, Paris, France, Jul 20–24, 1998, arXiv:cond-mat/9808047.
- [62] S. S. Manna, *J. Phys. A: Math. Gen.* **24**, L363 (1991).
- [63] G. Pruessner, *Int. J. Mod. Phys. B* **27**, 1350009 (2013), arXiv:1208.2069.
- [64] K. Christensen, Á. Corral, V. Frette, J. Feder, and T. Jøssang, *Phys. Rev. Lett.* **77**, 107 (1996).
- [65] D. Dhar, *Physica A* **340**, 535 (2004), arXiv:cond-mat/0309490.
- [66] Á. Corral, *Phys. Rev. E* **69**, 026107 (pages 12) (2004), arXiv:cond-mat/0310181v1.
- [67] S. Lübeck, *Phys. Rev. E* **61**, 204 (2000).
- [68] R. Pastor-Satorras and A. Vespignani, *Eur. Phys. J. B* **19**, 583 (2001), arXiv:cond-mat/0101358.
- [69] J. A. Bonachela, Ph.D. thesis, Departamento de Electromagnetismo y Física de la Materia & Institute Carlos I for Theoretical and Computational Physics, University of Granada, Granada, Spain (2008), accessed 12 Sep 2009, URL <http://hera.ugr.es/tesisugr/17706312.pdf>.
- [70] M. Matsumoto and T. Nishimura, *ACM Trans. Model. Comp. Sim.* **8**, 3 (1998).
- [71] P. Bak and K. Sneppen, *Phys. Rev. Lett.* **71**, 4083 (1993).
- [72] J. A. Bonachela and M. A. Muñoz, *Physica A* **384**, 89 (2007), proceedings of the *International Conference on Statistical Physics*, Raichak and Kolkata, India, Jan 5–9, 2007.
- [73] J. A. Bonachela and M. A. Muñoz, *AIP Conf. Proc.* **1091**, 204 (2009), proceedings of *Modeling and Simulation of New Materials: Tenth Granada Lectures*, Granada, Spain, Sep 15–19, 2008, arXiv:0905.1827.
- [74] H. Nakanishi and K. Sneppen, *Phys. Rev. E* **55**, 4012 (1997).
- [75] D. Hexner and D. Levine, *Phys. Rev. Lett.* **114**, 110602 (2015).
- [76] S. Torquato and F. H. Stillinger, *Phys. Rev. E* **68**, 041113 (2003).
- [77] D. Dhar, G. Pruessner, P. Expert, K. Christensen, and N. Zachariou (2015), arXiv:1511.06088.
- [78] J.-P. Hansen and I. R. McDonald, *Theory of simple liquids* (Academic Press, London, UK, 2006).
- [79] A. Clauset, C. R. Shalizi, and M. E. J. Newman, *SIAM Rev.* **51**, 661 (2009), arXiv:0706.1062v2.
- [80] A. Deluca and Á. Corral, *Acta Geophys.* **61**, 1351 (2013).
- [81] K. Christensen, N. Farid, G. Pruessner, and M. Stapleton, *Eur. Phys. J. B* **62**, 331 (2008).
- [82] P. Le Doussal and K. J. Wiese, *Phys. Rev. E* **88**, 022106 (2013).
- [83] T. Thiery, P. L. Doussal, and K. J. Wiese (2015), arXiv:1504.05342v1.
- [84] M. C. Kuntz and J. P. Sethna, *Phys. Rev. B* **62**, 11699 (2000).
- [85] A. Baldassarri, F. Colaiori, and C. Castellano, *Phys. Rev. Lett.* **90**, 060601 (2003).
- [86] L. Laurson, M. J. Alava, and S. Zapperi, *J. Stat. Mech.* **2005**, L11001 (2005).
- [87] M. De Menech, A. L. Stella, and C. Tebaldi, *Phys. Rev. E* **58**, R2677 (1998).
- [88] A. Vespignani, R. Dickman, M. A. Muñoz, and S. Zapperi, *Phys. Rev. Lett.* **81**, 5676 (1998), arXiv:cond-mat/9806249v2.
- [89] G. Pruessner, *Phys. Rev. E* **76**, 061103 (pages 4) (2007), arXiv:0712.0979v1.
- [90] C. W. Gardiner, *Handbook of Stochastic Methods* (Springer-Verlag, Berlin, Germany, 1997), 2nd ed.
- [91] T. W. Anderson, *The Statistical Analysis of Time Series* (John Wiley & Sons, New York, NY, USA, 1971).
- [92] P. Welinder, G. Pruessner, and K. Christensen, *New J. Phys.* **9**, 149 (pages 18) (2007).
- [93] S. Lübeck and P. C. Heger, *Phys. Rev. E* **68**, 056102 (pages 11) (2003).
- [94] Z. Olami, H. J. S. Feder, and K. Christensen, *Phys. Rev. Lett.* **68**, 1244 (1992).
- [95] A. A. Middleton and C. Tang, *Phys. Rev. Lett.* **74**, 742 (1995).
- [96] V. Frette, K. Christensen, A. Malthe-Sørensen, J. Feder, T. Jøssang, and P. Meakin, *Nature* **379**, 49 (1996).
- [97] M. A. Stapleton, Ph.D. thesis, Imperial College London, University of London, London SW7 2AZ, UK (2007), accessed 12 May 2007, URL <http://www.matthewstapleton.com/thesis.pdf>.
- [98] A. M. Ferrenberg, D. P. Landau, and K. Binder, *J. Stat. Phys.* **63**, 867 (1991).
- [99] R. Dickman, M. Alava, M. A. Muñoz, J. Peltola, A. Vespignani, and S. Zapperi, *Phys. Rev. E* **64**, 056104 (pages 7) (2001).
- [100] R. Dickman, T. Tomé, and M. J. de Oliveira, *Phys. Rev. E* **66**, 016111 (pages 8) (2002).
- [101] R. Dickman, *Phys. Rev. E* **73**, 036131 (pages 5) (2006).
- [102] S. B. Lee, *Phys. Rev. Lett.* **110**, 159601 (2013).
- [103] I. Jensen, *J. Phys. A: Math. Gen.* **32**, 5233 (1999).
- [104] F. J. Wegner, *Phys. Rev. B* **5**, 4529 (1972).
- [105] M. N. Barber, in *Phase Transitions and Critical Phenomena*, edited by C. Domb and J. L. Lebowitz (Academic Press, New York, NY, USA, 1983), vol. 8, pp. 145–266.
- [106] A. Chua and K. Christensen (2002), arXiv:cond-mat/0203260v2.
- [107] Wolfram Research Inc., *Mathematica* (Wolfram Research, Inc., Champaign, IL, USA, 2014), version 10.0.2.0.
- [108] T. Sadhu and D. Dhar, *J. Stat. Phys.* **134**, 427 (2009).

- [109] D. Dhar, *Physica A* **270**, 69 (1999), rooted in [61], arXiv:cond-mat/9902137.
- [110] G. Willis, Ph.D. thesis, Imperial College London, Department of Mathematics, London, UK (2015), accessed 6 Aug 2016, URL <https://spiral.imperial.ac.uk/handle/10044/1/28952>.
- [111] G. R. Grimmett and D. R. Stirzaker, *Probability and Random Processes* (Oxford University Press, New York, NY, USA, 1992), 2nd ed.
- [112] N. G. van Kampen, *Stochastic Processes in Physics and Chemistry* (Elsevier Science B. V., Amsterdam, The Netherlands, 1992), third impression 2001, enlarged and revised.

Appendix A: Markov matrices of the one-dimensional Manna Model

In the appendices we determine properties of the distribution of quiescent or “relaxed” configurations of the one-dimensional Manna Model in the stationary (or steady) state. A configuration is said to be quiescent or relaxed if none of the sites carries more than one particle. Given that the particle number at each site is non-negative, there are therefore $N = 2^L$ relaxed configurations in a system with L sites.

The distribution of quiescent configurations will be captured in a (column) probability vector $|p\rangle \in \mathbb{R}^N$, with each component $p_i \geq 0$ corresponding to the probability to find the system in configuration $i \in \{1, 2, \dots, N\}$. The evolution of this probability vector is due to $N \times N$ Markov matrices a_x , “charging” the system at site $x \in \{1, 2, \dots, L\}$ and fully relaxing it. The elements $(a_x)_{ji}$ of these matrices are the probability with which relaxed configuration j goes over to relaxed configuration i after charging the system at x . The distribution of final configurations after charging an ensemble of systems given by $|p\rangle$ on site x is thus given by $a_x |p\rangle$. The steady state is described by a distribution $|p_{0,x}\rangle$, not necessarily unique and initially expected to depend on x , which is invariant under the application of a_x , *i.e.* $a_x |p_{0,x}\rangle = |p_{0,x}\rangle$.

Further below, we will make extensive use of the equation $a_x^2 = (1/4)(a_{x-1} + a_{x+1})^2$ due to Dhar [61], Eq. (B1), which encapsulates the toppling rules of the Manna Model by relating the charging of x to the charging of its neighbours (subject to boundary conditions). For illustration purposes, we will occasionally distinguish a_{x_0} , the charging at a particular initial position x_0 and a_x , the charging at any other x .

Much of the calculations in the present section are more straight forward in the Oslo Model [64], where (in one dimension) two particles are moved away from the toppling site by moving one particle to each neighbour (corresponding to a downhill movement of height-units). In contrast to the Manna Model, in the Oslo Model avalanches cannot last indefinitely. As we will see, this is related to a certain nil-potency of matrices (which is not found in the Manna Model) and thus leads to a simplification of the Markov matrices a_x which have

been determined in the Oslo Model for systems up to size $L = 8$ [66]. The nil-potency, however, also has the consequence of certain configurations being inaccessible [106].

In the following, we briefly outline how the Markov matrices a_x can be determined in closed form, using computer algebra and some simple enumeration. As set out above, there are precisely $N = 2^L$ relaxed configurations in a system with L sites. After charging site x the configuration may no longer be relaxed, *i.e.* the number of particles residing at site x (and in the course of the avalanche at other sites) may exceed 1. We will refer to a configuration that *may* still decay into a relaxed configuration as an “excited configuration”. In a slight abuse of terminology, the set of excited configurations contains all relaxed configurations but not *vice versa*. While there is in principle no “height restriction” in the Manna Model, given we allow only single charges, there are at most $M = (L+2)^L$ excited configurations, because after being charged once, a system cannot contain more than $L+1$ particles, which may be distributed among the L sites in all possible ways during the course of an avalanche. In other words, the M excited configurations are certainly closed under the evolution of the Manna Model. In fact, M is a rather generous over-estimate, as many of those $(L+2)^L$ excited configurations may not be accessible from any relaxed configuration, because they contain more than $L+1$ particles.

To construct the Markov matrices a_x (for all x at once), we will first construct the rectangular $N \times M$ matrix E which contains the probabilities with which each configuration (mostly, however, non-relaxed ones) decays to a particular relaxed one. The entries of a_x are those N columns of E (which has M columns) which correspond to initial configurations that are relaxed configurations except for one additional particle added at site x . For example, to extract the resulting distribution of configurations after charging the relaxed configuration $(1, 0, 1)$ at the first site, one has to consult the entries for $(2, 0, 1)$ in E .

To construct E , we first introduce the (column) vectors $|e_i\rangle \in \mathbb{R}^N$, with $i \in \{1, 2, \dots, M\}$, whose entries are the probabilities for an excited configuration i to end up in a particular relaxed configuration $k \in \{1, 2, \dots, N\}$. These e_{ki} can be determined implicitly as

$$|e_i\rangle = |r_i\rangle + E|\epsilon_i\rangle \quad (\text{A1})$$

where E is the $N \times M$ matrix that maps each excited configuration to a relaxed configuration, *i.e.*

$$E = \left(|e_1\rangle |e_2\rangle \dots |e_M\rangle \right) \quad (\text{A2})$$

is made up of the M column vector $|e_i\rangle \in \mathbb{R}^N$. The vector $|\epsilon_i\rangle \in \mathbb{R}^M$ is a column vector where each entry ϵ_{ji} is the probability with which the non-relaxed configuration i goes over into the non-relaxed configuration j , by toppling, *at least* one active site. The column vector

$|r_i\rangle \in \mathbb{R}^N$, $i = 1, 2, \dots, M$ is the vector of probabilities r_{ji} that excited configuration i goes over into relaxed configuration j . If i is a relaxed configuration then $|r_i\rangle$ and $|\epsilon_i\rangle$ have a single non-vanishing entry and $|\epsilon_i\rangle$ vanishes everywhere. Each relaxation (or “decay channel”) is to be accounted for exactly once in Eq. (A1) either by $|r_i\rangle$ or by $E|\epsilon_i\rangle$. No overcounting ought to take place, even when $|r_i\rangle$ and $E|\epsilon_i\rangle$ both evolve excited configuration i to a relaxed configuration; $|r_i\rangle$ does it directly while $E|\epsilon_i\rangle$ does it via non-relaxed configurations not considered in $|r_i\rangle$. To simplify accounting, $|r_i\rangle$ may account for relaxations to a relaxed configuration in exactly one step (or none, namely when i is relaxed already) and $|\epsilon_i\rangle$ for the transition to another non-relaxed configuration in exactly one step.

Combining Eq. (A1) and Eq. (A2) gives the implicit equation

$$E = R + E\mathcal{E} \quad (\text{A3})$$

and thus

$$E = R(\mathbf{1} - \mathcal{E})^{-1} \quad (\text{A4})$$

with

$$R = \left(|r_1\rangle |r_2\rangle \dots |r_M\rangle \right) \quad (\text{A5})$$

the $N \times M$ matrix of relaxations of M excited configurations to N relaxed configurations directly (via relaxation of at least one site) and

$$\mathcal{E} = \left(|\epsilon_1\rangle |\epsilon_2\rangle \dots |\epsilon_M\rangle \right) \quad (\text{A6})$$

the $M \times M$ matrix of transitions from one excited configuration to another excited configuration (by relaxation of at least one site). One may read Eq. (A3) as indicating that the decay of any configuration into a relaxed one happens either within one step (R) or by the decay of a configuration that has evolved by one step (\mathcal{E}).

If R is easy to populate and all decay channels are considered at once, then \mathcal{E} vanishes and $E = R$. In general, however, this is not the case and both R and \mathcal{E} contain single topplings (mostly, as R may contain entries corresponding to no toppling at all). Because the probabilities involving single relaxations are integer multiples of $1/4$, the matrices \mathcal{E} and R , which are easily determined by automated enumeration, can be represented as (sparse) matrices containing integers, preceded by a factor $1/4$. Once R and \mathcal{E} are determined for a given system size in such an *exact* enumeration scheme, a computer algebra system (such as Mathematica [107]) can derive E in exact form and extract all a_x . Other successful methods to characterise the transition matrices, in particular for the Manna Model by Sadhu and Dhar [108], can be found in the literature [66].

In the following we discuss a number of numerical implementation details. Given that memory requirements

become a significant constraint, the matrices are best kept small, which can be achieved by considering only those excited configurations, which are actually encountered in the decay channels of every singly charged (initially relaxed) configuration. In other words, in a numerical implementation, all N relaxed configurations are generated first and charged at the L different sites to generate precisely $LN/2$ excited configurations (namely those L times N configurations which carried 1 particle at the site that is being charged, which is the case for precisely $N/2$ of the configurations). Those excited configurations must be part of the following considerations, as are all excited configurations that appear as intermediate configuration in the various decay channels.

These initially excited configurations are placed on a stack, which in the following contains one entry for each excited configuration not considered yet. In addition, a lookup-table of all possible excited configurations is maintained. That list contains an index for each excited configuration that indicates their position in the matrices, with -1 signalling that the configuration has not been considered yet. The indices for the relaxed configurations are most easily determined by interpreting their binary representation as the occupation; for example the index 3 indicates the first two sites occupied and the rest empty. However, in general, configurations are best represented as an L digit number with base $L+2$ (namely up to $L+1$ particles per site). The first two sites singly occupied therefore translates to $1+(L+2)$. Because not all excited configurations will be generated, not all indices are used and therefore maps are needed from indices to configurations and vice versa.

For simplicity and to reduce memory requirements, the size of the matrices is determined first by relaxing all $LN/2$ initially excited states and all excited states appearing in their decay channels. Only then the matrices are allocated and populated, by repeating this process, as described in the following.

Taking an element off the stack of unprocessed excited states, it is processed by, say, finding the leftmost excited site, generating three (two for boundary sites) excited states, and putting them on the stack if they have not been considered already. Repeating this process until the stack is empty provides the total number $M' \leq M$ of excited configurations to be considered.

After reserving memory for the M' excited configurations (or, rather, for the matrices of size $M' \times M'$), the matrices described above can be generated. They are populated by repeating the process above (filling the stack with singly excited configurations and updating those) using the lookup-table described above to determine rows and columns of R and \mathcal{E} , which in an actual implementation may better be realised as parts of a bigger, joint matrix, as they share the number and indexing of the columns. After determining and outputting those two matrices, E can be calculated in closed form using Eq. (A4) in a computer algebra system.

In principle, one could generate the relevant matrix at

the time of determining the indices (each configuration on the stack has been assigned an index at the time it enters the stack, so in principle, at the time of determining possible new configurations, all their indices are known). However, the memory to be reserved for the matrix $M' \times M'$ is significantly smaller than for $M \times M$, so M' should be determined first. This is not a computationally costly exercise.

Further code is needed to extract the correct data to compile the Markov matrices a_{x_0} for each of the driving sites x_0 . In line with the notation above, each *row* of the Markov matrix corresponds to a particular target configuration, *i.e.* the probabilities to make the transition from i to j is stored in row j and column i . This is the same for E . The Markov matrix for a particular driving site x_0 is compiled column by column or line by line,⁸ half of which contain a single entry (unity) for a transition from one relaxed configuration to another relaxed configuration, as the driven site x_0 is empty. The other half contain the entries from the matrix E for those excited configurations, which actually feature as those reached from driving any of the relaxed configurations at site x_0 . All other elements of E may be thought of as “stepping stones” to compile the entries that make up the Markov matrix a_{x_0} .

Finally, some more code may be needed to determine observables from the eigenvectors of the Markov matrix, for example a suitable density matrix, that translates each relaxed configuration to an occupation for each site.

The procedure above may appear rather cumbersome, in particular in comparison to similar procedures for, say, the Oslo Model [64–66]. The reason for the extra complication, embodied in Eq. (A4) is the appearance of decay channels of arbitrary duration in the Manna Model for any $L > 1$: In principle a pair of particles might move back and forth indefinitely, therefore requiring the implicit determination of decay probabilities. This cannot possibly happen in the Oslo Model, where particle transport is deterministic (even when the decision whether or not it takes place is stochastic) and so each system size has a finite maximum avalanche size. In the Oslo Model, determining the Markov matrices is therefore a “mere” counting exercise, which may be tedious, but is finite. The Manna Model necessitates the solution of an additional set of linear equations, Eq. (A4).

To see the difference between Oslo and Manna Model mathematically we note that the excited-excited relaxation matrix \mathcal{E} is nilpotent in the Oslo Model, *i.e.* a finite number of relaxations produces a relaxed configuration. This is not the case in the Manna Model. The problem

is vividly expressed in Eq. (A4), as

$$(\mathbf{1} - \mathcal{E})^{-1} = \sum_{i=0}^{\infty} \mathcal{E}^i \quad (\text{A7})$$

assuming convergence. In the Oslo model, the right hand side contains a finite number of terms, because \mathcal{E} is nilpotent.

Appendix B: Eigenstates

In the following we carry on with the characterisation of operators and their eigenvectors in the one-dimensional Manna Model. We will call an eigenvector $|e\rangle$ of a_x with eigenvalue unity, $a_x |e\rangle = |e\rangle$, an *eigenstate*. An eigenstate is thus a distribution of configurations that is invariant under the action of a_x . By normalisation, a row of unities is a left eigenvector with eigenvalue unity of any Markov matrix, and a corresponding right eigenvector exists. We will call a “joint eigenstate” any eigenstate that is common to all operators a_x .

As prominently pointed out by Grassberger, Dhar and Mohanty [40] (also [108]), the Abelianess (in particular the commutation property) of the a_x guarantees that a joint eigenstate exists. For many applications, it may be enough to know of the existence of a joint stationary state, that is the same eigenstate independent of the site driven. However, eigenstates may be degenerate and different ones reached depending on the site driven and the initial condition. Yet, by the Perron-Frobenius theorem, the eigenstate is *unique* provided all final (recurrent) states are “accessible” from every initial state; otherwise the set of all final states may be decomposable into disjoint subsets. As shown explicitly in Appendix B 2 accessibility is easily demonstrated for any global, random drive operator a [109], driving randomly with finite probability on every site, as defined in Eq. (B5). As any such operators commute, their eigenstates are thus identical and unique.

However, accessibility is much more difficult to demonstrate for an individual, single a_{x_0} , *i.e.* if driving takes place at only one site x_0 . In Appendix B 1, we show that all eigenstates of a_1 and a_L are common to all operators, including any random drive, which has a unique eigenstate. It follows that a_1 and a_L have the same unique eigenstate as any random drive. The proof does not hinge on accessibility by a_1 and a_L , but on the operator equation Eq. (B1), due to Dhar [61] as mentioned above.

That accessibility is a non-trivial hurdle is shown in Appendix B 3, as the eigenstates of a_x are *not unique* if L is odd and x is even. The argument presented applies to other models, such as the Oslo Model [64]. Consequently, the (degenerate) eigenstates of some operators do not coincide with those obtained for random drive, but depend on initial conditions.

⁸ Most easily done so that each line corresponds to a particular *initial* state, which requires some transpose operations.

1. Joint eigenstates

The key insight (to be proved in the following) is that every eigenstate of a_1 , that is the Markov matrix (or operator) controlling the evolution of the system after charging the first site once (the left-most site, $x_0 = 1$) is also an eigenstate of all other operators a_{x_0} (which is what we call a “joint eigenstate”) [110]. The argument can obviously be inverted to demonstrate the same for a_L for driving the right-most site. What makes these two sites, $x_0 = 1$ and $x_0 = L$, special are the boundary conditions. To show that every eigenstate of a_1 and a_L is an eigenstate of all a_x goes beyond demonstrating that there is a common eigenstate of all a_x , because the uniqueness of the latter implies the uniqueness and thus the identity of the eigenstates of a_1 , a_L and the common one. In other words, the unique eigenstate that is common to all a_x is the *only* eigenstate of a_1 and a_L and so boundary drive always arrives at the same stationary state as any global drive, irrespective of initial conditions. As shown in Appendix B3, in general, the same does not apply to a_{x_0} for $x_0 \notin \{1, L\}$, *i.e.* the eigenstates of, say, a_2 may be degenerate and thus may *not* coincide with the unique, common one, even when the numerics (Fig. 28) suggests that *asymptotically* the density profile at stationarity is independent of the driving position. All that follows for the eigenstates of a_x from their Abelianess and the uniqueness of the eigenstate of random drive, is that one particular linear combination of their eigenstates coincides with the unique, common one.

Squared Markov matrices of the Manna Model have the important property [61]

$$a_x^2 = \frac{1}{4} (a_{x-1} + a_{x+1})^2, \quad (\text{B1})$$

for all $x \in \{1, 2, \dots, L\}$ with boundary conditions $a_0 = \mathbf{1} = a_{L+1}$, identities, as charging the system outside the boundary sites $x = 1$ and $x = L$ leaves it invariant. Abelianess of the Manna Model means that a_x and a_y commute, so that the crossterm of Eq. (B1) may be written as $2a_{x+1}a_{x-1}$.

In the following, we will show that if $|e\rangle$ is an eigenstate of a_{x-1} and a_x , *i.e.* for charging the left two sites, then it is also an eigenstate of a_{x+1} , the rightmost site of the three consecutive ones at $x-1$, x and $x+1$. A proof by induction then starts by considering an eigenstate of a_1 and using $a_0 = \mathbf{1}$.

If $a_{x'}|e\rangle = |e\rangle$ for both $x' = x-1$ and $x' = x$, then it follows from $a_x^2|e\rangle = |e\rangle$ and (B1) that

$$|e\rangle = \frac{1}{4} (|e\rangle + 2a_{x+1}|e\rangle + a_{x+1}^2|e\rangle). \quad (\text{B2})$$

If we define $|\delta\rangle$ such that $a_{x+1}|e\rangle = |e\rangle + |\delta\rangle$, *i.e.* the deviation of $a_{x+1}|e\rangle$ from $|e\rangle$, we have $a_{x+1}^2|e\rangle = a_{x+1}(|e\rangle + |\delta\rangle) = |e\rangle + |\delta\rangle + a_{x+1}|\delta\rangle$ and therefore

$$a_{x+1}|\delta\rangle = -3|\delta\rangle, \quad (\text{B3})$$

i.e. $|\delta\rangle$ is either an eigenvector of a_{x+1} with eigenvalue -3 or it vanishes. Because a_{x+1} is a Markov matrix, its spectrum is bounded by the unit circle and it follows that $|\delta\rangle$ vanishes and thus $a_{x+1}|e\rangle = |e\rangle$, *i.e.* $|e\rangle$ is an eigenstate of a_{x+1} . In summary, if $a_{x'}|e\rangle = |e\rangle$ for $x' = x-1$ and $x' = x$, then $a_{x+1}|e\rangle = |e\rangle$. By induction it follows that if $a_{x'}|e\rangle = |e\rangle$ for $x' = 0$ and $x' = 1$ then $a_{x'}|e\rangle = |e\rangle$ for $x' \in 0, \dots, L+1$. The base case is easily established for $x' = 1$ and $|e\rangle$ an eigenstate of a_1 , because $a_0|e\rangle = |e\rangle$ follows trivially from $a_0 = \mathbf{1}$. This concludes the proof.

The proof can obviously be applied “in reverse” to demonstrate that an eigenstate $|e\rangle$ with $a_L|e\rangle = |e\rangle$ must be an eigenstate of all $a_{x'}$. This is no longer possible if boundary conditions are modified, for example to reflecting ones, $a_{L+1} = a_L$, so that

$$a_L^2 = \frac{1}{4} (a_{L-1} + a_{L+1})^2 = a_{L-1}^2. \quad (\text{B4})$$

One might think that means the proof above no longer applies in the presence of reflecting boundaries, because they imply that Eq. (B1) does not apply for $x = L$. However, to prove that $a_x|e\rangle = |e\rangle$ for $x \in \{0, \dots, L\}$ (no longer including the “irrelevant” site $x = L+1$) Eq. (B1) is only ever invoked for $x \leq L-1$, *i.e.* the modification of Eq. (B1) for a_L^2 , Eq. (B4), never enters. It follows that all eigenstates of a_1 are eigenstates of all operators. The proof can even be generalised to systems with anisotropy, but not to those with ballistic motion, *i.e.* when all particles moved during a toppling are moved to one side only, which makes perfect sense, as that dynamics excludes evolution of sites upstream, so charging there or charging downstream produces a different sequence of configurations and thus a different eigenstate.

A similar proof is available for the Oslo Model [64] where $a_x^3 = a_{x+1}a_xa_{x-1}$ [65] replaces Eq. (B1) above, again in the presence of Abelianess. To arrive at a statement about the independence of the steady state from the driving or the uniqueness of the joint eigenstate [40] by invoking Perron-Frobenius, one has to consider accessibility, as done below for the Manna Model.

2. Uniqueness of eigenstate

Above, we have shown that every eigenstate of a_1 and a_L remains invariant under the application of any of the operators a_x (for any $x \in \{1, 2, \dots, L\}$). However, we have also shown that *any* eigenstate of a_1 and a_L is an eigenstate of all a_x . This is specific to a_1 and a_L . We have no proof of that property for any other operator a_x . In the following, we show that the eigenstates of a_1 and a_L are unique, which follows from them being joint eigenstates of all a_x . In Appendix B3 we will demonstrate that eigenstates of a_x for even x are degenerate if L is odd, so that not all of their eigenstates are also joint eigenstates.

In the following, we will consider the operators a_x in a linear combination to make them amenable to the Perron-Frobenius theorem in its simplest form: if a is an irreducible Markov matrix, *i.e.* there exists a power $k_{fi} > 0$ for each initial configuration i and each final configuration f , such that $(a^{k_{fi}})_{fi} > 0$, then the eigenvector with eigenvalue 1 is unique [111].

If $|e\rangle$ is an eigenstate of all operators a_{x_0} , with $x_0 \in \{1, 2, \dots, L\}$, then

$$a = \sum_{x_0=1}^L p_{x_0} a_{x_0}, \quad (\text{B5})$$

which is the operator of “random drive” with probabilistic weights $p_{x_0} > 0$ so that $\sum_{x_0} p_{x_0} = 1$, has obviously also that eigenstate, $a|e\rangle = |e\rangle$. The Markov matrix a is what is referred to above as random drive and what is being studied in the following. We will show that its eigenstate is unique, by demonstrating accessibility explicitly. Because every joint eigenstate is necessarily an eigenstate of a , it follows that joint eigenstates (simultaneous eigenstates of all a_x) are unique. Because all eigenstates of a_1 and a_L are joint eigenstates, it follows that a_1 , a_L and a have the same, unique eigenstate.

To determine the positivity of the entries of a positive power of a , all that matters is whether a decay channel exists, that connects initial configuration i and final configuration f within a finite number of relaxations, which therefore occur with a finite probability.⁹ By demonstrating that such a channel exists for each of the N^2 pairs of initial and final states, we also demonstrate that all are recurrent. In the following, we may consider very unlikely decay channels, yet that suffices for the argument. Unlike the Abelian Sandpile [4], not all recurrent states appear with the same frequency.

The relevant decay channels are easily constructed explicitly: Any initial quiescent configuration containing in total n_i particles can be emptied by applying a repeatedly and choosing the decay channel whereby each site containing a particle already is charged and the resulting pair of particles moved to a boundary until it is dissipated by leaving the system. This procedure requires n_i charges, *i.e.* a^{n_i} contains entries indicating that the empty configuration is obtained with finite probability starting from a configuration containing n_i particles. To reach any configuration with n_f particles from there, a is repeatedly applied and the “decay” channel is chosen whereby each site to be occupied is charged, requiring n_f further charges. It takes therefore never more than $n_i + n_f$ charges to go from one quiescent configuration to another, *i.e.* $k_{fi} = n_i + n_f$ and $(a^{n_i+n_f})_{fi} > 0$.

⁹ If some final states are accessible only from some particular initial states (and thus not all are recurrent), it may happen that several distinct stationary states exist, which may be reached depending on initialisation or, given not all are recurrent, are accessed depending on the initial (random) sequence of charges.

Given that $n_i = L$ is a unique state and $n_f = L$ from $n_i = L$ therefore reached trivially,¹⁰ the maximum number of charges to access a particular quiescent configuration from another, given, quiescent configuration is $2L - 1$ for $L > 1$ (it is 2 for $L = 1$).

It follows that a is irreducible and thus, by Perron-Frobenius, has a unique eigenvector with eigenvalue unity.¹¹ By construction, Eq. (B5), one eigenstate of a is known, namely the eigenstate $|e\rangle$ of $x_0 = 1$ or $x_0 = L$ studied in Appendix B 1, which turned out to be a joint eigenstate such that $a_x |e\rangle = |e\rangle$ for all $x \in \{1, 2, \dots, L\}$. With the present accessibility argument, we know that any such joint eigenstate $|e\rangle$ is unique (there exists at most one joint eigenstate) and that it is also the eigenstate of random drive, in particular uniform drive. Because all 2^L states are accessible for a from all initial 2^L states, the eigenstate $|e\rangle$ has strictly positive elements (all states recur with positive frequencies).

This concludes the proof that there is exactly one stationary state $|e\rangle$ that is reached by either driving only at site $x_0 = 1$, or only at site $x_0 = L$ or randomly throughout the lattice, Eq. (B5). In the next section we consider the question whether the same can be said about driving only at site $x_0 = 2, 3, \dots, L - 1$. It turns out, that this is not the case. There are certain x_0 (namely even x_0 in lattices with odd L), that reach different stationary states depending on initial conditions. Their degenerate eigenstates form a subspace such that the eigenstate $|e\rangle$ of a_1 , a_L and a is only one particular linear combination of their eigenstates. In other words, driving at these sites x_0 generally leads to a different stationary state. However, as far as density profiles are concerned, in reasonably large systems, these different stationary states are numerically indiscernible, as shown below.

3. Degeneracy

In the proof above, the uniqueness of the stationary state hinges on the positivity of the elements of the Markov matrix a raised to some power k . In contrast to random drive Eq. (B5), this positivity cannot be shown for individual a_{x_0} . In the following, we will demonstrate that certain configurations are inaccessible from certain other configurations for certain a_{x_0} , *i.e.* that some

¹⁰ Of course, we cannot allow $k_{fi} = 0$ as a valid number of applications of a to go from i to f , but from the completely full lattice $n_i = L$ the completely full $n_f = L$ is accessed within two charges, namely by emptying one site and refilling it. The same argument applies to $n_i = 0 = n_f$.

¹¹ In fact, one can show, taking a route via the completely filled lattice, that a for $L > 1$ is primitive (there is a single power $k = 2(L + 2)$ such that $(a^k)_{fi} > 0$ for all i and f), so that periodic behaviour can be excluded as well, *i.e.* all eigenvalues other than 1 have magnitude strictly less than unity. For $L = 1$ that is not the case, as is easily seen by the periodic behaviour of that system.

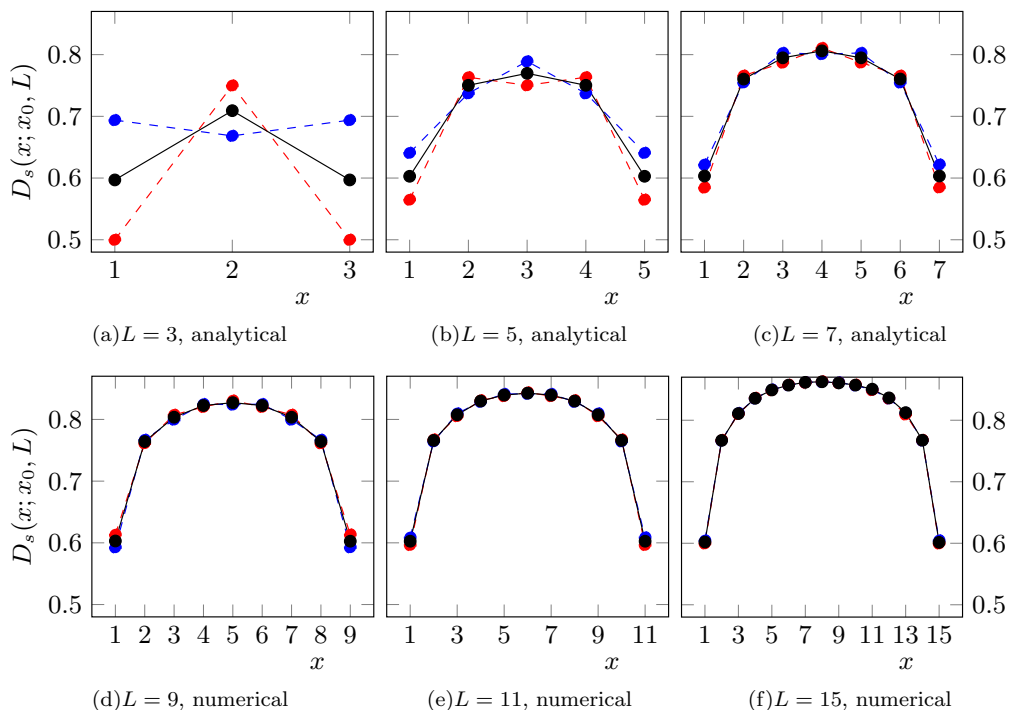


FIG. 28: Density profiles observed in a range of system sizes L , for driving at $x_0 = 1$ (black, full line) and driving at $x_0 = 2$ (red and blue, dashed lines), lines to guide the eye. The only degeneracy we observed was for odd L and driving at even x_0 . Analytically, the profiles were obtained for $L \leq 7$ by summing over the weights in the eigenstate vector which correspond to configurations that had a given site occupied. Numerically, they were obtained for $L \geq 9$ by driving (typically 10^7 times) at a given site, starting from an empty lattice and, in a separate run, from a lattice occupied initially only at $x_0 + 1$, thereby enforcing the other parity (see main text).

of the a_{x_0} are decomposable [112] (the chain not irreducible [111]). As a result, these operators have (at least) two distinct, *i.e.* degenerate eigenstates, whose equally weighted superposition is in fact the unique eigenstate $|e\rangle$ of a_1 , a_L and a , Eq. (B5), discussed above.

It is generally very difficult to demonstrate which set of states is accessible by driving the system only at one particular site (but, as seen above, very straight forward to show that all states are accessible when the system is driven randomly at all sites). All we can demonstrate in the following is that the eigenstate of some a_{x_0} are *at least* two-fold degenerate (although we have convinced ourselves numerically that no higher degeneracy occurs). From the proof in Appendix B 1 eigenstates of a_1 and a_L are common to all a_{x_0} and from Appendix B 2 we also know that this eigenstate is unique, *i.e.* we know that a_1 and a_L have unique eigenstates, so they they do *not* possess a degenerate eigenstate. We show now that the a_{x_0} with even x_0 have a degenerate eigenstate if L is odd (we know already that a_L never has a degenerate eigenstate).

The degeneracy is due to parity conservation, namely the inaccessibility of the set of configurations with an even number of particles on the odd sublattice (which is the set of sites with odd coordinates $1 \leq x \leq L$) from those with an odd number of particles there and

vice versa: Focusing on bulk-dynamics and thus ignoring boundaries and driving site for a moment, the number of particles transferred in a toppling from one sublattice to the other is always even, *i.e.* under bulk dynamics the parity of the particle number on each sublattice is conserved. As far as boundaries and driving is concerned, topplings at boundary sites break that symmetry whenever one particle is lost. Driving at site x_0 changes the parity of its sublattice.

One boundary site is always odd, $x_0 = 1$, *i.e.* the parity of the particle number on the even sublattice is never conserved. The second boundary site is $x_0 = L$. If L is even the parity on the odd sublattice is also not conserved, *i.e.* none of them are conserved. If L is odd, then the parity on the odd sublattice is conserved, unless the driving site itself is odd.¹² In other words, when driving odd L at even x_0 , the phase space divides into two mutually inaccessible regions. We conclude that for odd L and even x_0 degeneracy is at least two-fold. With the findings above (joint eigenstate of all operators and the

¹² In fact, for odd L , driving on a site on the odd sublattice flips the parity of the particle number of the odd sublattice and because for odd L this is the only mechanism by which the parity can be changed, one may expect one eigenvalue of -1 .

lack of parity conservations for even L or odd x_0), we suspect that this is in fact the only situation when the phase space becomes disjoint, *i.e.* there is at most two-fold degeneracy. Unfortunately, L is odd and x_0 is even for the centre driving used above.

We were able to verify exactly two-fold degeneracy up to the largest system we could analyse analytically, $L = 7$, driving at sites $x_0 = 2$ and at $x_0 = 4$. On each even site, the pair of eigenstates can obviously be written so that they are orthogonal. In fact, the two eigenstates on each (even) site can always be chosen so that they correspond to the stationary states where all recurrent configurations have either even or odd parity of the odd sublattice, setting components corresponding to states with the other parity to 0. The eigenstates for a given parity found on different (even) sites must be the same, because the linear combination of the two eigenstates must result in the (same) unique joint eigenstate. The pair of eigenstates can, in fact, be constructed by taking all components in the common, unique eigenstate corresponding to one particular parity of the odd sublattice, setting the others to 0. In other words, if there is indeed only ever at most two-fold degeneracy at even x_0 for odd L , then the pairs of eigenstates at those driving sites x_0 can be chosen to be identical among different x_0 .

To see that the unique joint eigenstate is an equally weighted sum of the two eigenstates containing only configurations of a single parity on the odd sublattice, we consider (any) global drive where even and odd parity of the odd sublattice occur with equal frequencies, because it changes only when odd sites are driven. As a result, configurations with odd and even parity on the odd sublattice appear with equal frequencies in the unique joint eigenstate, which must therefore be made up from the two eigenstates of opposite parity with equal weights.

As we were unable to identify any degeneracy in even L or for driving at odd x_0 , the further analysis focuses on odd L and even driving x_0 . In $L \leq 7$, we were able to calculate matrices a_{x_0} and their eigenstates explicitly using the techniques discussed in Appendix A and the computer algebra system Mathematica [107]. We confirmed that the equally weighted sum of the two degenerate eigenstates (for even and odd parity) reproduces the unique eigenstate $|e\rangle$ and that there was two-fold degeneracy of the eigenstate only when driving even sites and not when driving odd sites. For larger L we have determined numerically the density profile (*i.e.* the probability for a site to be occupied in the stationary state) as a “fingerprint” of the stationary state, Fig. 28. In these systems, we could only ever see two-fold degeneracy for driving at even x_0 in odd L resulting in the same pair of density profiles for all even x_0 . With increasing system size the (in total three) different density profiles become less and less different. Fig. 28(f) shows the profiles obtained for $L = 15$ which are virtually indistinguishable from the unique density profile of odd $x_0 = 1$. In reasonably large systems as those studied above, observing the degeneracy in the density profile may be beyond nu-

merical reach. We expect similar caveats to apply in the Oslo Model [40, 64].